

Exploring planetary interiors: Experiments at extreme conditions

by

Kanani Kealaokhehaulani Meulang Lee

B. S. (University of San Francisco) 1999

A dissertation submitted in partial satisfaction of the

requirements for the degree of

Doctor of Philosophy

in

Geophysics

in the

GRADUATE DIVISION

of the

UNIVERSITY OF CALIFORNIA, BERKELEY

Committee in charge:

Professor Raymond Jeanloz, Chair

Professor Michael Manga

Professor Geoffrey Marcy

Fall 2003

The dissertation of Kanani Kealaokehaulani Meulang Lee is approved:

Chair	Date
-------	------

	Date
--	------

	Date
--	------

University of California, Berkeley

Fall 2003

Exploring planetary interiors: Experiments at extreme conditions

Copyright 2003

by

Kanani Kealaokehaulani Meulang Lee

Abstract

Exploring Planetary Interiors: Experiments at Extreme Conditions

by

Kanani Kealaokehaulani Meulang Lee

Doctor of Philosophy in Geophysics

University of California, Berkeley

Professor Raymond Jeanloz, Chair

In-situ high-pressure and high-temperature experiments are invaluable to understanding the interiors of planets primarily giving us insight into the relationship of pressure and temperature on the chemical and physical characteristics of planetary materials as well as testing current theories of planetary accretion, differentiation and evolution throughout a planet's lifetime.

X-ray diffraction was used to measure the volume response to pressure and temperature of a natural peridotite at lower-mantle pressures. A lower mantle composed of an upper-mantle rock composition is 1-4% less dense than seismic observations for temperatures between 2000-3000 K, suggesting distinct mantle layers not only based on structural phase changes but also chemical differences.

X-ray diffraction was also used to track the alloying behavior between two very different elements, alkali-metal potassium (K) and transition-metal iron (Fe) to test the theory of an alkali-to-transition metal electronic transition at high pressure as well as the theory of sequestering potassium into the Earth's iron-rich core thereby providing a long-lived radioactive isotope ^{40}K to power the Earth's magnetic field and mantle dynamics.

At pressures above ~26 GPa and above the melting temperature of iron, K and Fe form an alloy in which one percent of the Fe atoms are substituted for K in the hexagonal-close-pack structure of ϵ -Fe thereby validating the former theory and making the latter possible.

Dynamic and static experimental methods were combined to explore the behavior of water at pressures above ~50 GPa and up to ~10,000 K. Water is found to exhibit complicated physical behavior—not surprising since at relatively low pressures and temperatures water has more than a dozen structures—with changing optical properties indicative of ionization and metallization with increased pressures and temperatures.

Table of Contents

Exploring Planetary Interiors: Experiments at Extreme Conditions

List of Figures	ii
List of Tables	iv
List of Symbols	v
Acknowledgements	vi
Introduction	1
Part I: Exploring the Deep Earth	7
Lower Mantle: Peridotite	
Chapter 1: Equations of state of the high-pressure phases of a natural peridotite and implications for the Earth's lower mantle	8
Core: Iron-Potassium Alloying	
Chapter 2: High-pressure alloying of potassium and iron: Radioactivity in the Earth's core?	42
Part II: Exploring Icy Giants	60
Chapter 3: Forming icy giant interiors: Laser-driven shock waves on pre-compressed water	61
Appendix: Technical Aspects	81
Appendix A: Limits to resolution in composition and density in ultrahigh- pressure experiments on natural mantle-rock samples	82
Appendix B: Taking thin diamonds to their limit: Coupling static-compression and laser-shock techniques to generate dense water	112

List of Figures

Part I: Exploring the Deep Earth

Figure 1-1:	Rietveld-refined x-ray diffraction pattern of BN-35	36
Figure 1-2:	Volume vs. pressure for orthorhombic perovskite	37
Figure 1-3:	Volume vs. pressure for magnesiowüstite	38
Figure 1-4:	Volume vs. pressure for calcium perovskite	39
Figure 1-5:	Volume vs. pressure for transformed peridotite assemblage	40
Figure 1-6:	Comparison of lower-mantle assemblage with PREM	41
Figure 2-1:	X-ray diffraction patterns of potassium and iron at high pressure	58
Figure 2-2:	Iron unit-cell volumes vs. pressure	59

Part II: Exploring Icy Giants

Figure 3-1:	VISAR image of shocked pre-compressed water	79
Figure 3-2:	Pressure vs. temperature phase diagram of shocked pre-compressed water	80

Appendix: Technical Aspects

Figure A-1(A):	Raw x-ray diffraction patterns of BN-35 at 51.8 GPa	107
Figure A-1(B):	Rietveld-refined x-ray diffraction pattern of BN-35 at 51.8 GPa	108
Figure A-2:	Percent deviations in unit-cell volumes for lower-mantle phases	109
Figure A-3:	Volume ratio of orthorhombic perovskite to	

	magnesiowüstite, $V_{\text{opv}}/V_{\text{mw}}$ at high pressure (Top) and upon quench (Bottom)	110
Figure A-4:	Photomicrograph, schematic drawing and SEM image of recovered BN-35 sample	111
Figure B-1:	Schematic cross-section of diamond-cell configuration used for laser-driven shock experiments on pre-compressed samples	120
Figure B-2:	Maximum pressure load vs. diamond thickness for thin Diamonds	120
Figure B-3:	Schematic cross-section of flexure of thin diamond flat	121
Figure B-4:	Interferometric measurement of diamond flat deflection	121
Figure B-5:	Diamond flat deflection vs. maximum pressure load	122
Figure B-6:	Index of refraction of water vs. pressure	122

List of Tables

Part I: Exploring the Deep Earth

Table 1-1:	Composition comparison of BN-35 and pyrolite	29
Table 1-2:	Comparison of equation of state parameters of lower-mantle minerals	30
Table 1-3:	Equation of state data for the three high-pressure phases and the whole-rock assemblage	31
Table 1-4:	Thermal parameters for Mie-Grüneisen-Debye equation of state	32

Part II: Exploring Icy Giants

Table 3-1:	Initial condition and Hugoniot parameters	76
------------	---	----

Appendix: Technical Aspects

Table A-1:	Composition of BN-35 and individual phases	100
Table A-2:	Electron microprobe analyses of quenched samples	101
Table A-3:	Orthorhombic perovskite composition inferred from electron microprobe analyses	102
Table A-4:	Decomposition reactions of initial minerals to lower-mantle phases	103

List of Symbols

a_i	volume fraction of phase i
d	distance between lattice planes
E_{th}	thermal energy
F	normalized pressure
f	Eulerian strain
hkl	Miller indices
K_{0T}	isothermal bulk modulus at ambient conditions
K_{0T}'	pressure derivative of K_0
P	pressure
q	volume dependence of γ
T	temperature
V	volume
V_0	volume at ambient conditions
x_i	molar fraction of phase i
α	coefficient of thermal expansion
γ	Grüneisen parameter
λ	x-ray wavelength
ρ	density
ρ_0	density at ambient conditions
θ	x-ray scattering angle
Θ_D	Debye temperature

Acknowledgements

I could not have completed this research without the help of many key people academically, scientifically, technically, physically and emotionally. I thank H. Camblong, my first college physics professor, for introducing me to quantum mechanics and R. Pockalny for refocusing my physics background for study in the Earth sciences. I certainly would not have entered graduate studies in geophysics had I not been exposed to both fields.

Scientifically, B. O'Neill laid the framework out for the studies of peridotite while W. R. Panero and L. R. Benedetti taught me many of the experimental techniques and gave me hours of priceless advice. S.-H. Shim provided thoughtful questions and advice pushing my analyses further. S. M. Clark for continuing to ask the important questions. M. Bukowinski for making the first quantum-mechanical predictions on potassium's transition-metal tendencies. I thank G. Steinle-Neumann and D. Rubie for inviting me to Bayerisches Geoinstitut to run calculations on my experimental results on potassium and iron. G. W. Collins, P. M. Celliers, D. Hicks, J. H. Eggert, A. Mackinnon, S. J. Moon and countless others at Lawrence Livermore National Laboratory who brought me into the world of dynamic compression through laser-driven shock waves. I thank M. Manga for his efficient and thorough support during the development of my thesis and G. Marcy for expressing a genuine interest in the our own rocky planet Earth far from the hot, gaseous giants that he is accustomed to studying. Of course, the person that ties all of these people together would be my advisor, Raymond Jeanloz who first introduced me to the high-pressure research world.

Technically, there have been many: W. Unites, J. Donovan, M. Feinemann, T. Teague, D. Smith, G. Shen, V. Prakapenko, and the numerous duty operators at the Stanford Synchrotron Radiation Laboratory.

Physically and emotionally (they go hand-in-hand after all), I could not have done this without my husband Erik Girndt. He has kept me sane and deserves an award for listening to me rehearse all of my talks—although occasionally falling asleep! My family has been wonderful always knowing that I could “do it” even though they may not have really understood what “it” was. Thanks to S. Al-Hashimi for getting me back into shape. M. d’Alessio, M. Panning, H. Gönnermann, K. Knight, S. Park and the rest from our first-year class: we got through our oral exams together. I thank D. Stegman, L. Hammersley, M. Feinemann, S. Akber-Knutsen, D. Larowe and others, for being good role models. L. R. Benedetti, W. R. Panero, M. A. d’Alessio, I. Johanson, V. E. Lee, R. S. McWilliams and B. Grocholski for being good office mates.

Most of this work was completed at three Department of Energy-funded synchrotrons: Stanford Synchrotron Radiation Laboratory, the Advanced Photon Source and the Advanced Light Source and was supported by the National Science Foundation, Lawrence Livermore National Laboratory and the University of California at Berkeley. The laser-driven shock wave experiments were conducted at the Vulcan Laser Facility at the Rutherford Appleton Laboratory in Didcot, England, U. K.

Chapter 2, Appendix A and B have been published or will soon be published as papers elsewhere, in *Geophysical Research Letters*, *Physics of Earth & Planetary Interiors* and in the conference proceedings of the *APS, Shock Compression Condensed Matter* meeting respectively.

Introduction

For more than 80 years, high-pressure and high-temperature experiments have been performed to study the physical properties of various materials [*Bridgman*, 1923; *Mao et al.*, 1978; *Marsh*, 1980]. Most notably in the study of the Earth and other planets, these experiments which reproduce the extreme conditions of planetary interiors are ultimately the best way to test theories of planetary structure based on seismology, moment of inertia, gravity and magnetic field measurements, as well as accretion and differentiation models.

Here two different techniques are utilized to study the high-pressure and -temperature behavior of relevant planetary materials: a natural peridotite, potassium and iron, and water. The first technique employs a laser-heated diamond-anvil cell (DAC) [*Heinz and Jeanloz*, 1987; *Shen et al.*, 1998] which incorporates the long-term quasi-static high-pressure conditions of a DAC with the heating capabilities of a continuous wave laser. With some amount of difficulty, this technique can reach pressures of a few hundred gigapascals (GPa) and up to several thousand Kelvin (K), thus able to routinely reproduce conditions relevant to the deep Earth. To reach the higher pressures and temperatures relevant to larger planets, the second technique, described in Appendix B and developed in collaboration with Lawrence Livermore National Laboratory and Commissariat a l'Energie Atomique, combines laser-driven shock waves with pre-compression of samples in a diamond-anvil cell [*Lee et al.*, 2002]. A short (~nanosecond) laser pulse creates a shock wave that takes the sample momentarily to high pressures and temperatures. By combining static and dynamic experimental techniques, different Hugoniot paths are traced throughout pressure-density-temperature

space because we can vary the sample's initial conditions (P_0 : pressure, ρ_0 : density, E_0 : energy) [*Zel'dovich and Raizer*, 1966].

Part I describes an exploration of the deep Earth, namely the lower mantle and core. Chapter 1 describes experiments of compressing and heating a natural peridotite—thought to represent the composition of the upper mantle—to test the theory of a chemically homogeneous mantle that is uniformly mixed by whole-mantle convection. I compare my density measurements at high pressures and temperatures with seismological observations of the Earth's interior [*Dziewonski and Anderson*, 1981] and find that physical properties of an upper-mantle composition at lower-mantle conditions do not match the seismologically observed properties of the deep mantle [*Lee et al.*, 2003a; *Lee et al.*, 2003b].

As the lower mantle constitutes approximately two-thirds of the Earth's volume, the chemical makeup of this region is especially important in the geodynamics. If the lower mantle and upper mantle are chemically distinct, the transition zone may not only be a transition of mineral structure but also a chemical boundary. This would greatly affect mantle convection, suggesting two (or more?) separately convecting regions of the mantle. Such distinct levels would be isolated by thermal boundary layers that conduct—rather than convect—heat upward, thus greatly reducing the efficiency of heat loss out of the Earth's deep interior. My results are in accord with geochemical models that suggest that the mantle is not entirely uniform in bulk composition, but instead has complex structure and thus complex dynamics [*Kellogg et al.*, 1999].

Furthering the heat story in the Earth, one can also look to the heat sources that cause the Earth's internal dynamics. There are two main heat sources in the Earth:

radioactive heating, and primordial, that is, the release of gravitational potential energy associated with accretion and differentiation of the planet. The latter is much harder to quantify, as it requires a detailed understanding of the Earth's formation and evolution. Radioactivity is easier to ascertain based on chemical analyses of terrestrial rocks and meteorites. Chapter 2 describes experiments that explore the high-pressure and -temperature behavior of potassium and iron together, and addresses an old—and recently renewed—debate regarding radioactivity in the Earth's core [Buffett, 2002; Wasserburg *et al.*, 1964]. The results suggest that potassium can indeed alloy with iron at mantle pressures and temperatures (~26 GPa, 2500 K) [Lee and Jeanloz, 2003]. This makes the theory of potassium sequestering in the core early in Earth's history plausible, thereby resolving cosmochemical discrepancies in the K/U ratio between terrestrial rocks and chondritic samples [Wasserburg *et al.*, 1964]. Long-lived radioactive isotope ^{40}K (half-life of ~1 billion years) in the Earth's core could currently provide as much as 8 terawatts (TW) of power, or approximately 20% of the Earth's total power budget [Verhoogen, 1980]. This power is more than adequate to sustain the Earth's magnetic field over its entire age.

Part II describes an exploration of the interiors of “Icy” Giant planets Uranus and Neptune. These larger planets, although composed of mostly “light” materials, namely “ices” water, ammonia and methane, have much more extreme interior conditions than the Earth. This is due to their large masses: nearly an order of magnitude increase in pressure and temperature over the Earth's interior! Using the novel technique of precompressing water prior to laser-driven shock proved difficult to employ, although a few density measurements at high pressure and temperature as well as marked changes in

the optical properties (i.e., reflectivity and opacity) in hot, dense water were measured and are described in chapter 3. This technique works well for very compressible materials (i.e., fluids) where the initial density strongly increases with nominal pressures. Although the first of these experiments were performed on water, more recently this new technique has been used on hydrogen, helium and nitrogen—all important constituents of giant planets [Loubeyre *et al.*, in press, 2004].

References

- Bridgman, P.W., The compressibility of thirty metals as a function of pressure and temperature, *Proceedings of the American Academy of Arts and Sciences*, 58, 166-242, 1923.
- Buffett, B.A., Estimates of heat flow in the deep mantle based on the power requirements for the geodynamo, *Geophysical Research Letters*, 29 (12), 10.1029, 2002.
- Dziewonski, A.M., and D.L. Anderson, Preliminary reference Earth model, *Physics of the Earth and Planetary Interiors*, 25 (4), 297-356, 1981.
- Heinz, D.L., and R. Jeanloz, Temperature measurements in the laser-heated diamond cell, in *High-Pressure Research in Mineral Physics*, edited by M.H. Manghnani, and Y. Syono, pp. 113-127, American Geophysical Union, Washington, D. C., 1987.
- Kellogg, L.H., B.H. Hager, and R.D. van der Hilst, Compositional stratification in the deep mantle, *Science*, 283 (5409), 1881-4, 1999.
- Lee, K.K.M., L.R. Benedetti, A. Mackinnon, D.G. Hicks, S.J. Moon, P. Loubeyre, F. Occelli, A. Dewaele, G.W. Collins, and R. Jeanloz, Taking thin diamonds to their limit: Coupling static-compression and laser-shock techniques to generate dense

- water, in *APS, Shock Compression Condensed Matter*, edited by M.D. Furnish, N.N. Thadhani, and Y. Horie, pp. 1363-1366, American Institute of Physics, Atlanta, Georgia, 2002.
- Lee, K.K.M., and R. Jeanloz, High-pressure alloying of potassium and iron: Radioactivity in the Earth's core?, *Geophysical Research Letters*, *30* (23), 2212, 2003.
- Lee, K.K.M., B. O'Neill, and R. Jeanloz, Limits to resolution in composition and density in ultrahigh-pressure experiments on natural mantle-rock samples, *Physics of Earth and Planetary Interiors*, in press, 2003a.
- Lee, K.K.M., B. O'Neill, S.-H. Shim, W.R. Panero, L.R. Benedetti, and R. Jeanloz, Equations of state of high-pressure phases of a natural peridotite and implications for the Earth's lower mantle, *Submitted*, 2003b.
- Loubeyre, P., P.M. Celliers, D.G. Hicks, E. Henry, A. Dewaele, J. Pasley, J. Eggert, M. Koenig, F. Occelli, K.K.M. Lee, R. Jeanloz, D. Neely, A. Benuzzi-Mounaix, D. Bradley, M. Bastea, S.J. Moon, and G.W. Collins, Coupling static and dynamic compressions: First measurements in dense hydrogen, *High Pressure Research*, in press, 2004.
- Mao, H.-K., P.M. Bell, J. Shaner, and D.J. Steinberg, Specific volume measurements of Cu, Mo, Pd, and Ag and calibration of the ruby R1 fluorescence pressure gauge from 0.06 to 1 Mbar, *Journal of Applied Physics*, *49*, 3276-3283, 1978.
- Marsh, S.P., *LASL Shock Hugoniot Data*, pp. 658, University of California Press, Berkeley, 1980.

- Shen, G., H.-K. Mao, R.J. Hemley, T.S. Duffy, and M.L. Rivers, Melting and crystal structure of iron at high pressures and temperatures, *Geophysical Research Letters*, 25 (3), 373-376, 1998.
- Verhoogen, J., *Energetics of the Earth*, 139 pp., National Academy of Sciences, Washington, D. C., 1980.
- Wasserburg, G.J., G.J.F. MacDonald, F. Hoyle, and W.A. Fowler, Relative contributions of Uranium, Thorium, and Potassium to heat production in the Earth, *Science*, 143, 465-467, 1964.
- Zel'dovich, Y.B., and Y.P. Raizer, *Physics of Shock Waves and High-Temperature Hydrodynamic Phenomena*, Dover Publications, Mineola, New York, 1966.

Part I: Exploring the Deep Earth

Chapter 1: Equations of state of the high-pressure phases of a natural peridotite and implications for the Earth's lower mantle

***Abstract.** To help determine the chemical composition of the Earth's mantle, we characterized an undepleted natural peridotite—thought to be representative of the Earth's upper-mantle—to 107 GPa using high-resolution x-ray diffraction. At lower-mantle conditions, the peridotite transforms to the assemblage 76 (± 2)% $(\text{Mg}_{0.88}\text{Fe}^{2+}_{0.05}\text{Fe}^{3+}_{0.01}\text{Al}_{0.12}\text{Si}_{0.94})\text{O}_3$ orthorhombic perovskite by volume (at zero pressure), 17 (± 2)% $(\text{Mg}_{0.80}\text{Fe}_{0.20})\text{O}$ magnesiowüstite and 7 (± 1)% CaSiO_3 perovskite. The measured room-temperature bulk properties of this high-pressure assemblage, together with a range of estimates of thermal properties of the constituent minerals, are inconsistent with seismological constraints on the density and bulk modulus of the lower mantle. Therefore, we propose that the lower mantle differs in bulk composition (e. g., richer in iron, $\text{Mg}\# \sim 0.85$) from current estimates for the upper mantle, requiring some amount of segregation between the upper and lower mantle over geological history.*

Introduction

Geochemists, geodynamicists, seismologists, and mineral physicists have long debated the nature of the Earth's mantle which comprises more than three-quarters of the Earth's volume and thus dictates the thermal and chemical evolution of the Earth [1-12]. The global discontinuities in seismic-wave velocities at 410 and 660 km depths are attributed to high-pressure transformations of upper-mantle minerals into lower-mantle phases [13-16]. However, recent studies suggest that there may be large-scale compositional variations near the base of the lower mantle, and there are reasons for suspecting that the mantle is not entirely uniform in bulk composition [8, 10, 17].

To assess the similarity in composition of the deep mantle to that at shallower levels, we compressed a natural peridotite—an upper-mantle rock—to lower-mantle pressures in a laser-heated diamond-anvil cell, and measured the lattice parameters and compressibility of the various mineral phases by high-resolution synchrotron and laboratory-based x-ray diffraction. If the mantle is homogeneous, the density and elasticity of the upper-mantle rock composition once transformed to the relevant mineral phases at lower-mantle conditions, should agree with the seismologically-observed properties of the lower mantle.

Methods

The starting material for our experiment, BN-35 [18-20], is a garnet-spinel lherzolite xenolith and thought to be a good proxy for relatively primitive and fertile upper-mantle rock. With an Mg# ≈ 0.89 and consisting of $\sim 45\%$ olivine, 25% orthopyroxene, 15% clinopyroxene, and 15% garnet by volume [18, 21], our sample is a

natural analog of pyrolite, a model intended to represent the upper mantle: see Table 1-1 (an Mg#, molar Mg/(Mg+Fe) ratio, of 0.90 (\pm 0.05) is the estimated value for the bulk composition of the uppermost mantle) [1].

Angle-dispersive x-ray diffraction patterns collected at high pressure, before and after laser heating, as well as after decompression confirm the identity of the phases, and show that their observed compressions are compatible with the known equations of state of the individual mineral phases (see Section 4, High-Pressure, Room-Temperature Measurements). Two independent sets of experiments were carried out. In the first, samples were compressed and transformed under quasi-hydrostatic conditions (argon pressure medium) in a laser-heated diamond-anvil cell (Nd-YAG laser, $\lambda = 1064$ nm or Nd-YLF laser, $\lambda = 1053$ nm), and characterized at room temperature by synchrotron x-ray diffraction using image plates at beamline 10-2 at the Stanford Synchrotron Radiation Laboratory ($\lambda = 0.7277$ Å) and the GSECARS 13-IDD beamline at the Advanced Photon Source ($\lambda = 0.4246$ Å). In the second set of experiments, the same sample material was loaded without a pressure medium and patterns were collected using laboratory sources with Mo $K\alpha$ ($\lambda = 0.7107$ Å) radiation (high-pressure diffraction) and Cu $K\alpha$ ($\lambda = 1.5418$ Å) radiation (zero-pressure diffraction) [20]. Ruby grains were added as a pressure calibrant in all experiments [22]. In some of the experimental runs, additional laser heating (at pressures of 41, 47, 66, 78 and 87 GPa) was applied to thermally relax the sample of any non-hydrostatic stresses. All 300 K measurements (synchrotron- and laboratory-based) are mutually compatible and are used to compile a whole-rock equation of state. More detailed experimental procedures have been described elsewhere [19, 20].

Experimental Results

Upon compression to lower-mantle pressures ($P > 24$ GPa) and laser heating to ~ 2000 K in a diamond anvil cell, the peridotite transforms into a new assemblage consisting of $64 (\pm 2)$ mol% orthorhombic perovskite (opv), $31 (\pm 2)$ mol% magnesiowüstite (mw), and $5 (\pm 1)$ mol% calcium perovskite (cpv). The identification and abundances of the high-pressure phases is determined by x-ray diffraction and through modeling the bulk composition of the starting material [19]. Twenty-five x-ray diffraction patterns were taken of the sample at pressures between 25 and 107 GPa at room temperature, before and after heating, and upon subsequent decompression (see Fig. 1-1).

Additional *in-situ* high-pressure, high-temperature experiments confirm that the opv, mw, and cpv phases exist at high temperatures (Fig. 1-1). Due to potential systematic errors, however, such measurements do not yield sufficiently reliable density values to allow a direct and independent comparison of the whole-rock assemblage at lower-mantle conditions with the seismologically-observed properties of the mantle; therefore, the measurements obtained *in-situ*, at simultaneously high pressures and temperatures, are not included here. The high-pressure and high-temperature data shown in the inset of Fig. 1-1 are nevertheless entirely consistent with our thermal equation of state.

Major-element Partitioning

Major-element partitioning was determined from the observed ambient-pressure unit-cell volume V_0 of opv and mw, as well as analysis of the bulk (starting) composition of the rock assuming conservation of cations and charge. In the absence of other minor elements, Mg and Fe partitioning into these high-pressure phases has been reasonably well documented [23-25], but the multi-variate partitioning of elements between the three phases found in the present natural assemblage is not well constrained by prior work [23, 26, 27]. No systematic trends in V_0 , and thus no systematic trends in individual phase compositions, were observed among our samples, despite different loading and synthesis conditions (e. g., pressure and temperature, see [19]). Therefore, the following assumptions were made in our analysis: the calcium perovskite is pure CaSiO_3 , incorporating all of the Ca in the multi-phase assemblage [27]; the Fe concentration in magnesiowüstite is determined by V_0 [14], with the remaining Fe assumed to be in orthorhombic perovskite; and all of the Al^{3+} cations are distributed between the Mg and Si sites in orthorhombic perovskite for charge balance. With the above constraints, it is possible to balance all major elements yielding the assemblage composition: 64 (± 2) mol% orthorhombic perovskite ($\text{Mg}_{0.88}\text{Fe}_{0.05}^{2+}\text{Fe}_{0.01}^{3+}\text{Al}_{0.12}\text{Si}_{0.94}\text{O}_3$), 31 (± 2) mol% magnesiowüstite ($\text{Mg}_{0.80}\text{Fe}_{0.20}\text{O}$), and 5 (± 1) mol% calcium perovskite CaSiO_3 . We note that the final values of whole-rock density remain unchanged, within quoted uncertainties, regardless of the validity of these assumptions [19].

High-Pressure, Room-Temperature Measurements

Orthorhombic Perovskite

Orthorhombic perovskite has long been recognized as the most abundant phase in the Earth's mantle (e.g., [28, 29]), probably making up more than 75% of the lower mantle and more than 50% of the Earth's volume. Except for a few early experiments on natural samples [20, 21, 29] and some recent experiments on Al-bearing perovskites [30-32], much of the focus has been on the Mg-endmember MgSiO_3 (e. g., [33]) and (Mg, Fe) SiO_3 (e.g., [34]) (see Table 1-2). At all pressures in our experimental range, we observe orthorhombic perovskite and measure its unit-cell volume as a function of pressure (Fig. 1-2). Despite a variety of synthesis-pressure and -temperature conditions, we do not find a systematic difference in Fe partitioning between opv and mw [19]. Using a 3rd order Birch-Murnaghan equation of state, we determined a compression curve for our opv that is comparable to previous equations of state (Table 1-2, Fig. 1-2). The relatively large V_0 that we measure for orthorhombic perovskite (~1% larger than pure endmember MgSiO_3) is consistent with the results of past studies on Fe- and Al-bearing silicate perovskites [14, 30, 31], and the compressibility is compatible with that documented by [31] (~2% smaller than pure endmember MgSiO_3).

Magnesiowüstite

The next most dominant phase of the lower mantle is expected to be magnesiowüstite. Extensive work has been done on the pure Mg (e. g., [35-37]) and Fe (e.g., [38]) endmembers, as well as on a variety of solid solutions between the two (e.g., [39, 40]). Magnesiowüstite is observed at all experimental pressures, as well as on quench, except at pressures of 70.6 and 84.4 GPa where the overlap of opv diffraction

peaks obscures mw identification. The equation of state we determine is compatible with those of former studies as is shown in Table 1-2 and Fig. 1-3.

Calcium Perovskite

Calcium perovskite is thought to be the least abundant of the major phases in the Earth's lower mantle [41]. Due to the consequently weak diffraction peaks of calcium perovskite and overlap of diffraction peaks with those of the more abundant phases, cpv was not detected above ~70 GPa, even though its stability has been documented to much higher pressures [42, 43] (Fig. 1-4). Calcium perovskite also does not quench to ambient conditions [42, 43]. Although there is some spread in the reported compressibility of cpv [42, 44, 45], its low abundance (~5 mol%) means that any resulting uncertainties make little difference to the assemblage's bulk properties (< 0.5%). Because of these difficulties, and the fact that our measurements are in agreement with it, the equation of state of [43] was used to determine the volume of the calcium perovskite portion of the assemblage in the modeling that we describe below.

Whole-Rock Assemblage

As we are able to track the structural changes of individual phases (see Table 1-2, 1-3), we are able to determine a high-pressure assemblage volume and density at each pressure, $V_{BN-35} = \sum_i x_i V_i$, from the molar ratios x_i of the three phases and the respective unit-cell volumes V_i (see Fig. 1-5). The derivative of the pressure–volume relation for the high-pressure assemblage yields the isothermal bulk modulus of the rock as a function of pressure (therefore depth) in the mantle.

Other methods of determining the bulk properties of composite materials include the Reuss (all grains equally stressed) and Voigt (all grains equally strained)

approximations (see [46] for a review); these provide a measure of the uncertainty associated with averaging the moduli (Table 1-3). The arithmetic mean of the Voigt and Reuss bounds, the Voigt-Reuss-Hill average, has also been suggested as another approximation to the moduli of composite materials. Whichever approximation is invoked (they all are very similar and lie within mutual uncertainties), none of our conclusions regarding the density and bulk composition of the lower mantle is affected. Also dispersion of seismic waves is known to affect the seismologically-observed moduli, which are only partly relaxed, whereas our approach yields fully relaxed values. Therefore our calculated bulk modulus represents a lower bound for comparison with the mantle, and may systematically underestimate the seismologically observed modulus. In combination with the effects of averaging moduli for a poly-phase aggregate, the resultant offset can amount to as much as 3% increased stiffness at lower-mantle conditions.

Birch-Murnaghan Equation of State

The individual-phase isothermal bulk modulus, K_{0T} , and its pressure derivative, K_{0T}' , are determined using the Birch-Murnaghan formalism [47], a good approximation for Earth materials, which is based on a Taylor expansion of the Helmholtz free energy in the Eulerian strain measure, f :

$$f = \frac{1}{2} \left[\left(\frac{V}{V_0} \right)^{-2/3} - 1 \right] \quad (1)$$

where V/V_0 is the ratio of the high-pressure volume V to the room-pressure volume V_0 . The pressure P can be normalized to give an effective derivative of the equation of state:

$$F = \frac{P}{3f(1+2f)^{5/2}} \quad (2)$$

Expanding to fourth order of Eulerian strain,

$$F = K_{0T}(1 + f\left(\frac{3}{2}K_{0T}' - 6\right) + f^2\left(\frac{3}{2}K_{0T}K_{0T}'' + \frac{3}{2}K_{0T}'\left(K_{0T}' - 7\right) + \frac{143}{6}\right) + \dots) \quad (3)$$

Routinely the Birch-Murnaghan formulism is truncated to third order (before the f^2 term), hence an F vs. f plot yields K_{0T} (intercept) and K_{0T}' (via the slope) (see Insets of Figs. 1-2 through 1-5).

High-Temperature Analysis

Whole-rock assemblage at High Pressure and Temperature

To compare our whole-rock, room-temperature data with seismic observations of the Earth's interior, we applied a Mie-Grüneisen-Debye model to determine a thermal equation of state for each phase as well as for the whole-rock assemblage at temperatures of 1000 K, 1500 K, 2000 K, 2500 K and 3000 K (Fig. 1-6) (see following Section, High-Temperature Analysis: Thermal Equation of State). Because the temperature variation is expected to be small (thus negligible) across the bulk of the lower mantle (~500 K from about 700-2700 km depth), an isotherm is a reasonable approximation for the actual temperature variation throughout much of the deep interior [48, 49]. Two sets of thermal parameters are used to compare our thermally-corrected data with the Preliminary Reference Earth Model (PREM) [50] (Table 1-4): the "Standard" set [39, 45, 51] is supported by a reanalysis of the gold pressure standard [52], whereas the "Low" set is illustrative of prior analyses yielding relatively low values of thermal expansion [6].

Thermal Equation of State

A Mie-Grüneisen thermal equation of state adds a thermal pressure to the room-temperature pressure at a given volume, yielding a total pressure at temperature T [6, 53]:

$$P_{total}(V, T) = P(V, 300 K) + P_{thermal}(V, T) \quad (4)$$

where,

$$P_{thermal} = \left(\frac{\gamma}{V}\right) \left[E_{thermal}(T, \Theta_D) - E_{thermal}(300 K, \Theta_D) \right] \quad (5)$$

where the Grüneisen parameter, γ , is,

$$\gamma = \gamma_0 \left(\frac{V}{V_0}\right)^q = -\frac{\partial \ln \Theta_D}{\partial \ln V} \quad (6)$$

and with a Debye model for the internal energy, $E_{thermal}$,

$$E_{thermal} = 9nRT \left(\frac{T}{\Theta_D}\right)^3 \int_0^{\frac{\Theta_D}{T}} \frac{x^3 dx}{e^x - 1} \quad (7)$$

and

$$\Theta_D = \Theta_{D0} \exp\left(\frac{\gamma_0 - \gamma}{q}\right), \quad (8)$$

where Θ_D is the Debye temperature. Subscript 0 indicates the value at zero pressure and 300 K. The correction from isothermal to adiabatic (subscript S) bulk modulus, $K_S = K_T (1 + \alpha \gamma T)$, is performed in a self-consistent manner using the same model and individual phase parameters (α is the volumetric thermal-expansion coefficient). K_T is determined from the fourth-order Birch-Murnaghan equation of state (3) [47]. For the whole-rock assemblage we use $\gamma_{rock} = \sum a_i \gamma_i$, where a_i is the volume percent of each phase and γ_i is the phase Grüneisen parameter. As thermal expansion depends on both pressure and temperature, we solved for α_{rock} directly by solving for the volume of the rock (as stated above) for a small interval ($\pm 1K$) around the temperature of interest and using

$$\alpha = \left. \frac{\partial \ln V}{\partial T} \right)_P \quad (\text{Table 1-4}).$$

High-Temperature Error Analysis

Representative error bars for the final pressure at a given volume and temperature are derived from the uncertainties in the 300 K compression measurements and in the correction to high temperature. The uncertainty in compression is determined via Bell et al.'s analysis [54], while the uncertainty in the thermal correction is based on the difference between the Standard and Low thermal-expansion models (Fig. 1-6, Table 1-4). This determination of uncertainty is probably generous, as the thermal portion (~2 times the compression part of the uncertainty) encompasses the full range of possible temperature corrections (“Standard” and “Low” Thermal Expansion Parameters, Table 1-4).

In general, at a given pressure an increase in temperature increases the uncertainty in the thermal portion; conversely, at a given temperature an increase in pressure decreases the uncertainty in the thermal portion of the equation of state. The reason for this is that the absolute magnitude of the thermal correction to the 300 K pressure (at a given volume) increases with increasing temperature and decreases with increasing pressure, the latter mitigating the increase in *relative* uncertainty of the thermal correction with increasing pressure.

Discussion

We apply our results by first testing the hypothesis that the entire mantle is uniformly mixed, and consists of a pyrolite-like composition. Comparison of experimentally observed phase transformations with the corresponding depths of seismic

discontinuities within the transition zone yields a temperature of 1900-2000 K for the top of the lower mantle, rising toward 2500 K at the bottom assuming an adiabat [14-16, 55].

It is evident from Fig. 1-6A, however, that the density of our natural peridotite is incompatible with such high temperatures. Even accounting for uncertainties in the thermal properties, the density can only be matched by temperatures between 1000-1500 K across the depth of the lower mantle: about 1000 K too cold, and below typical eruption temperatures at mid-ocean ridges [56]. Indeed, analysis of the bulk modulus also suggests lower-mantle temperatures in the range of 2000-3000 K (Fig. 1-6B).

One way to satisfy the observed properties of the lower mantle with a peridotite-like composition close to that which we studied is to invoke a higher iron content at depth, rather than the preferred value for the upper mantle ($Mg\# \approx 0.90$, see Table 1-1). If some region of the deep mantle differs in bulk composition from the shallower mantle, however, then temperatures are expected to be increased by about 500-1000 K due to the presence of thermal boundary layers at the interface at which the bulk composition changes, across which mixing is suppressed [49]. Thus, temperatures of about 2500-3000 (± 500) K are reasonable for a layer within the lower mantle that differs in composition from shallower depths (e.g., [8]).

As varying the Fe/Mg ratio has essentially no effect on the bulk modulus of the high-pressure, perovskite-dominated assemblage (e.g., [34]), Fig. 1-6B shows that such high temperatures are in good accord with our measurements. The density deficit of ~1-4% obtained from Fig. 1-6A can then be “fixed” by an increased abundance of iron, to an $Mg\# \approx 0.85 (\pm 0.02)$. The result is non-unique, however, as there are tradeoffs between

temperature and composition (e. g., including Si, Al and Ca abundances) for satisfying the observed properties of the lower mantle [51].

Nevertheless, the intrinsic density difference between the observed density profile for the lower mantle and the lower-mantle density predicted for the current (pyrolite-like) estimate of upper-mantle bulk composition is sufficient to stabilize layered convection over geological time [57-60]. Thus geochemical, geophysical and—now—mineral physical observations point to complex structure and dynamics of the Earth's mantle [8].

References

- [1] A.E. Ringwood, *Composition and Petrology of the Earth's Mantle*, 618 pp., McGraw-Hill, New York, 1975.
- [2] D.P. McKenzie, J.M. Roberts and N.O. Weiss, Convection in the Earth's mantle: towards a numerical simulation, *Journal of Fluid Mechanics* 62 pt.3, 465-538, 1974.
- [3] D.L. Anderson, *Composition of the Earth*, *Science* 243, 367-370, 1989.
- [4] Y. Fukao, S. Widiyantoro and M. Obayashi, Stagnant slabs in the upper and lower mantle transition region, *Reviews of Geophysics* 39(3), 291-323, 2001.
- [5] G.R. Helffrich and B.J. Wood, The Earth's mantle, *Nature* 412(6846), 501-507, 2001.
- [6] I. Jackson, Elasticity, composition and temperature of the Earth's lower mantle: a reappraisal, *Geophysical Journal International* 134(1), 291-311, 1998.
- [7] R. Jeanloz and E. Knittle, Density and composition of the lower mantle, *Philosophical Transactions of the Royal Society of London A (Mathematical and Physical Sciences)* 328(1599), 377-89, 1989.
- [8] L.H. Kellogg, B.H. Hager and R.D. van der Hilst, Compositional stratification in the deep mantle, *Science* 283(5409), 1881-4, 1999.
- [9] L. Stixrude, R.J. Hemley, Y. Fei, et al., Thermoelasticity of silicate perovskite and magnesiowüstite and stratification of the Earth's mantle, *Science* 257(5073), 1099-101, 1992.

- [10] R.D. van der Hilst and H. Karason, Compositional heterogeneity in the bottom 1000 kilometers of Earth's mantle: toward a hybrid convection model, *Science* 283(5409), 1885-8, 1999.
- [11] P.E. van Keken, E.H. Hauri and C.J. Ballentine, Mantle mixing: The generation, preservation, and destruction of chemical heterogeneity, *Annual Reviews of Earth and Planetary Science* 30(11), 1-33, 2002.
- [12] M.J. Drake and K. Righter, Determining the composition of the Earth, *Nature* 416, 39-44, 2002.
- [13] C.B. Agee, Phase transformation and seismic structure in the upper mantle and transition zone, in: *Ultrahigh-Pressure Mineralogy: Physics and Chemistry of the Earth's Deep Interior*, R.J. Hemley, ed., *Reviews in Mineralogy* 37, pp. 165-203, Mineralogical Society of America, Washington, D. C., 1998.
- [14] R. Jeanloz and A.B. Thompson, Phase transitions and mantle discontinuities, *Reviews of Geophysics and Space Physics* 21(1), 51-74, 1983.
- [15] S.H. Shim, T.S. Duffy and G. Shen, The post-spinel transformation in Mg_2SiO_4 and its relation to the 660 km seismic discontinuity, *Nature* 411(6837), 571-4, 2001.
- [16] I. Chudinovskikh and R. Boehler, High-pressure polymorphs of olivine and the 660-km seismic discontinuity, *Nature* 411(6837), 574-7, 2001.
- [17] A.M. Forte and J.X. Mitrovica, Deep-mantle high-viscosity flow and thermochemical structure inferred from seismic and geodynamic data, *Nature* 410(6832), 1049-56, 2001.

- [18] C.R. Stern, S.L. Saul, M.A. Skewes, et al., Garnet peridotite xenoliths from the Pali-Aike alkali basalts of southernmost South America, in: Fourth International Kimberlite Conference, J. Ross, ed., Kimberlites and Related Rocks 2, pp. 735-744, Blackwell Scientific, Perth, Australia, 1986.
- [19] K.K.M. Lee, B. O'Neill and R. Jeanloz, Limits to resolution in composition and density in ultrahigh-pressure experiments on natural mantle-rock samples, *Physics of the Earth and Planetary Interiors*, in press, 2003.
- [20] B. O'Neill, *Experimental Petrology of the Lower Mantle*, PhD, University of California, Berkeley, 1994.
- [21] B. O'Neill and R. Jeanloz, Experimental petrology of the lower mantle: A natural peridotite taken to 54 GPa, *Geophysical Research Letters* 17(10), 1477-80, 1990.
- [22] H.K. Mao, P.M. Bell, J.W. Shaner, et al., Specific volume measurements of Cu, Mo, Pd, and Ag and calibration of the ruby R1 fluorescence pressure gauge from 0.06 to 1 Mbar, *Journal of Applied Physics* 49(6), 3276-83, 1978.
- [23] B. O'Neill and R. Jeanloz, MgSiO₃-FeSiO₃-Al₂O₃ in the Earth's lower mantle: Perovskite and garnet at 1200 km depth, *Journal of Geophysical Research* 99(B10), 19,901-19,915, 1994.
- [24] H.K. Mao, G. Shen and R.J. Hemley, Multivariable dependence of Fe-Mg partitioning in the lower mantle, *Science* 278(5346), 2098-100, 1997.
- [25] D. Andrault, Evaluation of (Mg,Fe) partitioning between silicate perovskite and magnesiowüstite up to 120 GPa and 2300 K, *Journal of Geophysical Research* 106(B2), 2079-87, 2001.

- [26] B.J. Wood and D.C. Rubie, The effect of alumina on phase transformations at the 660-kilometer discontinuity from Fe-Mg partitioning experiments, *Science* 273(5281), 1522-4, 1996.
- [27] B.J. Wood, Phase transformations and partitioning relations in peridotite under lower mantle conditions, *Earth and Planetary Science Letters* 174(3-4), 341-54, 2000.
- [28] L.G. Liu, Orthorhombic perovskite phases observed in olivine, pyroxene, and garnet at high pressures and temperatures, *Physics of the Earth and Planetary Interiors* 11, 289-298, 1976.
- [29] E. Knittle and R. Jeanloz, Synthesis and equation of state of (Mg,Fe)SiO₃ perovskite to over 100 gigapascals, *Science* 235(4789), 668-70, 1987.
- [30] I. Daniel, H. Cardon, G. Fiquet, et al., Equation of state of Al-bearing perovskite to lower mantle pressure conditions, *Geophysical Research Letters* 28(19), 3789-92, 2001.
- [31] D. Andrault, N. Bolfan-Casanova and N. Guignot, Equation of state of lower mantle (Al,Fe)-MgSiO₃ perovskite, *Earth and Planetary Science Letters* 193(3-4), 501-8, 2001.
- [32] J. Zhang and D.J. Weidner, Thermal equation of state of Aluminum-enriched silicate perovskite, *Science* 284, 782-784, 1999.
- [33] G. Fiquet, A. Dewaele, D. Andrault, et al., Thermoelastic properties and crystal structure of MgSiO₃ perovskite at lower mantle pressure and temperature conditions, *Geophysical Research Letters* 27(1), 21-4, 2000.

- [34] H.K. Mao, R.J. Hemley, Y. Fei, et al., Effect of pressure, temperature, and composition on lattice parameters and density of (Fe,Mg)SiO₃-Perovskites to 30 GPa, *Journal of Geophysical Research* 96(B5), 8069-79, 1991.
- [35] A. Dewaele, G. Fiquet, D. Andrault, et al., P-V-T equation of state of periclase from synchrotron radiation measurements, *Journal of Geophysical Research* 105(B2), 2869-77, 2000.
- [36] I. Jackson and H. Niesler, The elasticity of periclase to 3 GPa and some geophysical implications, S. Akimoto and M.H. Manghnani, eds., pp. 93-113, Center for Academic Publications, 1982.
- [37] T.S. Duffy, R.J. Hemley and H.K. Mao, Equation of state and shear strength at multimegabar pressures: Magnesium oxide to 227 GPa, *Physical Review Letters* 74, 1371-1374, 1995.
- [38] R.M. Hazen and R. Jeanloz, Wüstite (Fe_{1-x}O): A Review of Its Defect Structure and Physical Properties, *Reviews of Geophysics and Space Physics* 22(1), 37-46, 1984.
- [39] Y. Fei, H.-K. Mao, J. Shu, et al., P-V-T Equation of State of Magnesiowüstite (Mg_{0.6}Fe_{0.4})O, *Phys Chem Minerals* 18, 416-422, 1992.
- [40] P. Richet, M. Ho-Kwang and P.M. Bell, Bulk moduli of magnesiowüstites from static compression measurements, *Journal of Geophysical Research* 94(B3), 3037-45, 1989.
- [41] S.H. Shim, T.S. Duffy and G. Shen, The stability and P-V-T equation of state of CaSiO₃ perovskite in the Earth's lower mantle, *Journal of Geophysical Research* 105(B11), 25955-68, 2000.

- [42] S.-H. Shim, T.S. Duffy and G. Shen, The equation of state of CaSiO₃ perovskite to 108 GPa at 300 K, *Physics of the Earth and Planetary Interiors* 120(4), 327-38, 2000.
- [43] H.K. Mao, L.C. Chen, R.J. Hemley, et al., Stability and equation of state of CaSiO₃-perovskite to 134 GPa, *Journal of Geophysical Research* 94(B12), 17889-94, 1989.
- [44] S.H. Shim, R. Jeanloz and T.S. Duffy, Tetragonal structure of CaSiO₃ perovskite above 20 GPa, *Geophysical Research Letters* 29(24), 2166, 2002.
- [45] Y. Wang, D.J. Weidner and F. Guyot, Thermal equation of state of CaSiO₃ perovskite, *Journal of Geophysical Research* 101(B1), 661-72, 1996.
- [46] F.D. Stacey, Thermoelasticity of a mineral composite and a reconsideration of lower mantle properties, *Physics of the Earth and Planetary Interiors* 106(3-4), 219-36, 1998.
- [47] F. Birch, Finite strain isotherm and velocities for single-crystal and polycrystalline NaCl at high pressures and 300 K, *Journal of Geophysical Research* 83, 1258-1267, 1978.
- [48] J.M. Brown and T.J. Shankland, Thermodynamic parameters in the Earth as determined from seismic profiles, *Geophysical Journal of the Royal Astronomical Society* 66(3), 579-96, 1981.
- [49] R. Jeanloz and F.M. Richter, Convection, composition, and the thermal state of the lower mantle, *Journal of Geophysical Research* 84(B10), 5497-5504, 1979.
- [50] A.M. Dziewonski and D.L. Anderson, Preliminary reference Earth model, *Physics of the Earth and Planetary Interiors* 25(4), 297-356, 1981.

- [51] L. Stixrude and M.S.T. Bukowinski, Stability of (Mg,Fe)SiO₃ perovskite and the structure of the lowermost mantle, *Geophysical Research Letters* 19(10), 1057-60, 1992.
- [52] S.H. Shim, T.S. Duffy and K. Takemura, Equation of state of gold and its application to the phase boundaries near 660-km depth in the Earth's Mantle, *Earth and Planetary Science Letters* 203(2), 729-739, 2002.
- [53] I. Jackson and S.M. Rigden, Analysis of P-V-T data: constraints on the thermoelastic properties of high-pressure minerals, *Physics of the Earth and Planetary Interiors* 96, 85-112, 1996.
- [54] P.M. Bell, H.K. Mao and J.A. Xu, Error analysis of parameter-fitting in equations of state for mantle minerals, in: *High-Pressure Research in Mineral Physics*, M.H. Manghnani and Y. Syono, eds. 2, pp. 447-454, American Geophysical Union, Washington, D. C., 1987.
- [55] E. Ito and E. Takahashi, Postspinel transformations in the system Mg₂SiO₄-Fe₂SiO₄ and some geophysical implications, *J. Geophys. Res.* 94, 10637-10646, 1989.
- [56] C.R.J. Kilburn, Lava flows and flow fields, in: *Encyclopedia of Volcanoes*, H. Sigurdsson, ed., pp. 291-305, Academic Press, San Diego, 2000.
- [57] U.R. Christensen, Models of mantle convection: One or several layers, *Philosophical Transactions of the Royal Society of London A (Mathematical and Physical Sciences)* 328, 417-424, 1989.
- [58] P. Olson, An experimental approach to thermal convection in an two-layered mantle, *Journal of Geophysical Research* 89, 11293-11301, 1984.

- [59] F.M. Richter and D.P. McKenzie, On some consequence and possible causes of layered mantle convection, *Journal of Geophysical Research* 86, 6133-6142, 1981.
- [60] H. Gönnerman, M. Manga and A.M. Jellinek, Dynamics and longevity of an initially stratified mantle, *Geophysical Research Letters* 29(10), 1399, 2002.
- [61] I. Jackson, *The Earth's Mantle: Composition, Structure, and Evolution*, pp. 566, Cambridge University Press, Cambridge, UK, 1998.
- [62] R. Jeanloz, The Earth's Mantle, in: *Encyclopedia of Volcanoes*, H. Sigurdsson, ed., pp. 41, Academic Press, San Diego, 2000.

Table 1-1. Composition comparison of BN-35 and pyrolite.

	BN-35 ^a cations per 12 O	Pyrolite ^b cations per 12 O ^c	Pyrolite ^c cations per 12 O	Upper estimate ^d cations per 12 O ^e	Mantle
Si	3.291 (0.094)	3.251 (0.084)	3.252	3.243 (0.101)	
Ti	0.014 (0.008)	0.011 (0.011)		0.010 (0.003)	
Al	0.367 (0.112)	0.391 (0.073)	0.375	0.382 (0.127)	
Fe ^f	0.503 (0.072)	0.474 (0.101)	0.526	0.458 (0.102)	
Mn	0.009 (0.002)	0.006 (0.002)		0.007 (0.003)	
Mg	4.010 (0.128)	4.094 (0.235)	4.137	4.125 (0.215)	
Ca	0.256 (0.012)	0.239 (0.065)	0.271	0.255 (0.077)	
Na	0.042 (0.010)	0.056 (0.021)		0.057 (0.028)	
K	0.0 (-)	0.002 (0.007)		0.001 (0.009)	
Ni	0.014 (-)	0.012 (0.003)		0.013 (0.003)	
Cr	0.017 (0.018)	0.017 (0.006)		0.023 (0.006)	
Mg #	= 0.89	0.90 (0.05)	0.89	0.90 (0.05)	
Mg/(Mg+Fe)					

^a Uncertainties are given in parentheses and are determined by taking the difference of element values from an independent measurement of the starting sample [18, 20].

^b An average pyrolite from Table 5-2, column 8 of [1]. Uncertainties are determined from the standard deviation of columns 1-7 of Table 5-2.

^c A simplified model based on the 5 major oxide components [61].

^d From [62].

^e Uncertainties are given in parentheses.

^f Fe²⁺ and Fe³⁺ totals are combined.

Table 1-2. Comparison of equation of state parameters of lower-mantle minerals using a 3rd order Birch-Murnaghan equation of state [47].

Study	Composition	V_0 (Å ³)	K_{0T} (GPa)	K_{0T}'	P range (GPa)
Orthorhombic Perovskite					
This Study	(Mg _{0.88} Fe ²⁺ _{0.05} Fe ³⁺ _{0.01} Al _{0.12} Si _{0.94})O ₃	163.90 (0.67)	269 (14)	4.06 (0.66)	24-107
Fiquet et al., 2000	MgSiO ₃	162.27 (0.01)	253 (9)	3.9 (0.2)	39-94
Knittle & Jeanloz, 1987	(Mg _{0.88} Fe _{0.12})SiO ₃	162.77 (0.39)	266 (6)	3.9 (0.4)	25-127
Mao et al., 1991	(Mg _{1.00-0.80} Fe _{0.00-0.20})SiO ₃	162.49 (0.07) - 163.53 (0.10)	261 (4)	4.0 ^a	< 29, synthesis at 40 GPa
Zhang & Weidner, 1999	Al _{0.10} (MgSi) _{0.95} O ₃	163.2 (0.2)	234 (4)	4.0 ^a	< 10
Daniel et al., 2001	Al _{0.154} (MgSi) _{0.923} O ₃	163.52 (0.03)	229 (4)	2.5 (0.4)	< 32
Andrault et al., 2001	(AlFe) _{0.05} (MgSi) _{0.95} O ₃	163.2 (0.2)	265.0 (3.7)	4.0 ^a	26-58
Andrault et al., 2001	Al _{0.05} MgSi _{0.95} O ₃	163.3 (0.2)	266.7 (2.8)	4.0 ^a	26-56
Andrault et al., 2001	Al _{0.22} (MgSi) _{0.89} O ₃	163.5 (0.4)	275.5 (6.0)	4.0 ^a	26-68
Magnesiowüstite					
This Study	(Mg _{0.80} Fe _{0.20})O	76.09 (0.60)	175 (9)	3.75 (0.46)	24-107
Jackson & Niesler, 1982	MgO	74.69	162.5 (0.2)	4.13 (0.09)	< 3
Duffy et al., 1995	MgO	74.7 ^a	177 (4)	4.0 (0.1)	< 227
Dewaele et al., 2000	MgO	74.71 ^a	161 ^a	3.94 (0.2)	< 53
Richet et al., 1989	(Mg _{0.40} Fe _{0.60}) O	78.43 (0.02)	149 (4)	4.0 ^a	< 50
Richet et al., 1989	(Mg _{0.20} Fe _{0.80}) O	79.26 (0.03)	148 (10)	4.0 ^a	< 49

^a fixed.

Table 1-3. Equation of state data for the three high-pressure phases and the whole-rock assemblage observed for a peridotite composition at lower-mantle pressures^a. Listed are the measured V_0 , K_{0T} , K_{0T}' and mol% of each of the three lower-mantle phases, as well as the whole-rock bulk properties obtained by four methods for calculating the properties of multi-phase assemblages [46]. We assume that the given phases keep a constant mol% abundance throughout the mantle, which yields $K_{0T} = 247 (\pm 21)$ GPa and $K_{0T}' = 4.01 (\pm 0.67)$. The other methods (Reuss, Voigt, and Voigt-Reuss-Hill) all yield values that fall within quoted uncertainties of our assumption of constant molar abundance.

<u>Phase</u>	V_0 (\AA^3)	K_{0T} (GPa)	K_{0T}'	mol%, x_i
opv	163.90 (0.67)	269 (14)	4.06 (0.66)	64 (2)
mw	76.09 (0.60)	175 (9)	3.75 (0.46)	31 (2)
cpv^b	45.37 (0.08)	281 (4)	4.0	5 (1)
<u>Whole rock</u>				
Constant mol%		247 (21)	4.01 (0.67)	
Reuss		247 (15)	4.13 (0.48)	
Voigt		254 (11)	4.00 (0.51)	
Voigt-Reuss-Hill		251	4.07	

^a Uncertainties in parentheses are 2 standard deviations.

^b Values taken from [43], where K_{0T}' is constrained to 4.0.

Table 1-4. Thermal parameters used in or obtained from the Mie-Grüneisen-Debye equation of state.

“Standard” Thermal Expansion Parameters

	opv^a	mw^b	cpv^c	rock^d
Θ_D (K)	1017	500	1100	
γ_0	1.96	1.5	1.7	
q	2.5	1.1	1	
α 300 K, 0 GPa (10^{-5} K)	2.4	3.1	3.0	2.6
α 2000 K, 0 GPa (10^{-5} K)^d	6.8	5.0	3.4	6.3
α 2000 K, 25 GPa (10^{-5} K)^d	3.3	2.9	2.3	3.2

“Low” Thermal Expansion Parameters

	opv^e	mw^e	cpv^c	rock^d
Θ_D (K)	1000	673	1100	
γ_0	1.31	1.41	1.7	
q	1	1.3	1	
α 300 K, 0 GPa (10^{-5} K)	1.6	3.1	3.0	2.0
α 2000 K, 0 GPa (10^{-5} K)^d	3.0	4.8	3.4	3.3
α 2000 K, 25 GPa (10^{-5} K)^d	2.1	2.6	2.3	2.2

^a From [9].

^b From [39].

^c From [45].

^d Calculated values (see Section 5.2, High-Temperature Analysis: Thermal Equation of State).

^e From [6].

Fig. 1-1. Rietveld refinement applied to the powder-diffraction pattern of BN-35 at 59.5 (± 1.4) GPa and 300 K collected with synchrotron x-ray ($\lambda = 0.7277 \text{ \AA}$) radiation [19]. The raw data (dots) and the refinement (solid curve) are consistent with 3 phases: opv, mw, cpv (tick marks in descending order). The unassigned diffraction peak at $\sim 2.5 \text{ \AA}$ is attributed to ruby (internal pressure standard). The goodness of the fit is shown in the residuals (% difference between observed and Rietveld fit) plotted below the data. **Inset:** *In-situ* high-pressure and high-temperature energy-dispersive x-ray diffraction pattern show the same phases to be present at 36 (± 2) GPa and $T \sim 1500$ (± 150) K. Vertical lines denote the gold pressure calibrant, and diffraction peaks from the individual phases are labeled.

Fig. 1-2. Volume versus pressure for orthorhombic perovskite at room temperature, based on data collected both on compression with laser-annealing at each pressure (black) and decompression (white). Gray symbols are measurements done without laser-annealing after initial synthesis heating. The circles are data collected from monochromatic ($\lambda = 0.7277 \text{ \AA}$) synchrotron radiation and the squares are from laboratory-based sources [19]. The heavy solid line through the data points is calculated from the Birch-Murnaghan equation of state. The dashed line is the Birch-Murnaghan equation of state of [34]. **Inset:** A more sensitive representation of the same data, an F vs. f plot (see Section 4.5, High-Pressure, Room-Temperature Measurements: Birch-Murnaghan Equation of State). The intercept of the line is the K_{0T} (269 ± 14 GPa) of orthorhombic perovskite, while the slope is related to K_{0T}' (4.06 ± 0.66). The shaded area is the extrapolated uncertainty.

Fig. 1-3. Volume versus pressure for magnesiowüstite at room temperature. Symbol identification is the same as in Figure 1-2. The heavy solid line through the data points is calculated from the Birch-Murnaghan equation of state. The dashed line is the Birch-Murnaghan equation of state of [39]. **Inset:** An F vs. f plot, as in Figure 1-2. The intercept of the line is the K_{0T} (175 ± 9 GPa) of magnesiowüstite, while the slope is related to K_{0T}' (3.75 ± 0.46).

Fig. 1-4. Volume versus pressure for calcium perovskite at room temperature. Symbol identification is the same as in Figure 1-2. The heavy solid line through the data points is calculated from the Birch-Murnaghan equation of state of [43] (used in this study). For comparison, the dashed line is the equation of state measured by [44]. **Inset:** An F vs. f plot, as in Figure 1-2.

Fig. 1-5. Volume versus pressure for the transformed peridotite assemblage at room temperature, based on data collected both on compression and decompression. The circles are data collected from synchrotron radiation and the squares are from laboratory-based sources [19]. The solid shapes represent diffraction patterns in which all 3 phases are present, while the open shapes include extrapolation due to unobserved phases. The curve through the data points is calculated from the Birch-Murnaghan equation of state of the whole-rock assemblage. **Inset:** An F vs. f plot, as in Figure 1-2. The intercept of the line is the K_{0T} (247 ± 21 GPa) of the rock, while the slope is related to K_{0T}' (4.01 ± 0.67).

Fig. 1-6. Comparison of lower-mantle assemblage with PREM [50]. Two scenarios are plotted which give a range of possibilities for mantle thermal expansivities: Standard (solid) and Low (dash) thermal expansion parameters (see Table 1-4). The isothermal temperatures used in the model are 1000 K (blue), 1500 K (purple), 2000 K (green), 2500 K (orange), and 3000 K (red). Representative error bars at 65 GPa (~1500 km depth) and 2000 K are given (see Section 5.3, High-Temperature Analysis: High-Temperature Error Analysis). **(A)** At temperatures relevant to the lower mantle of the Earth (2000-3000 K), the density of the whole-rock assemblage is lower than that of PREM by 1-4%. **(B)** The adiabatic bulk modulus K_s also differs from PREM by up to ~3% for relevant lower-mantle temperatures.

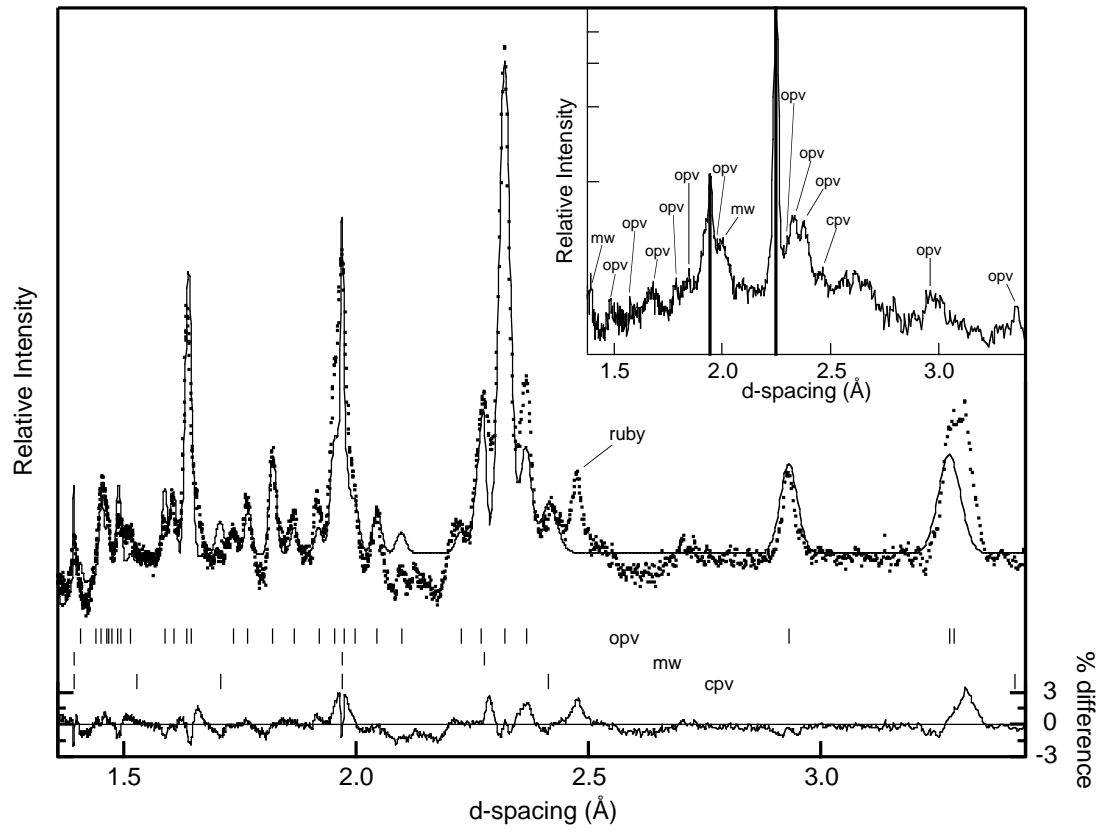


Fig. 1-1

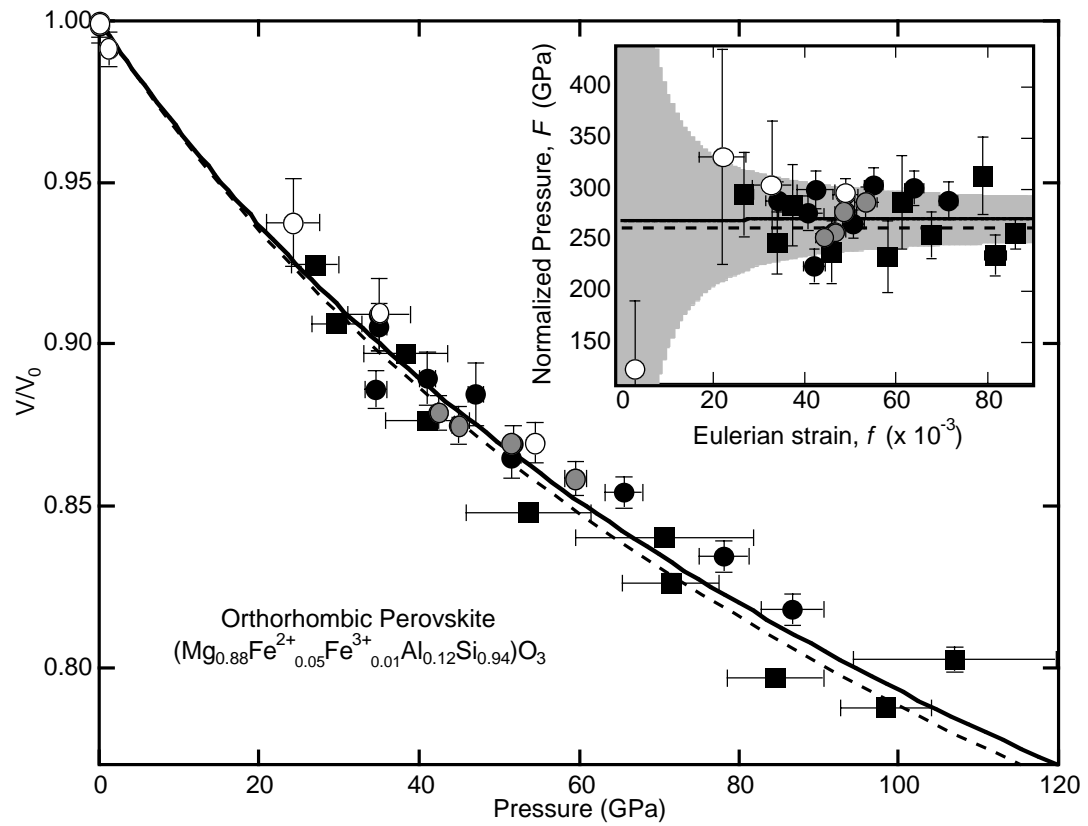


Fig. 1-2

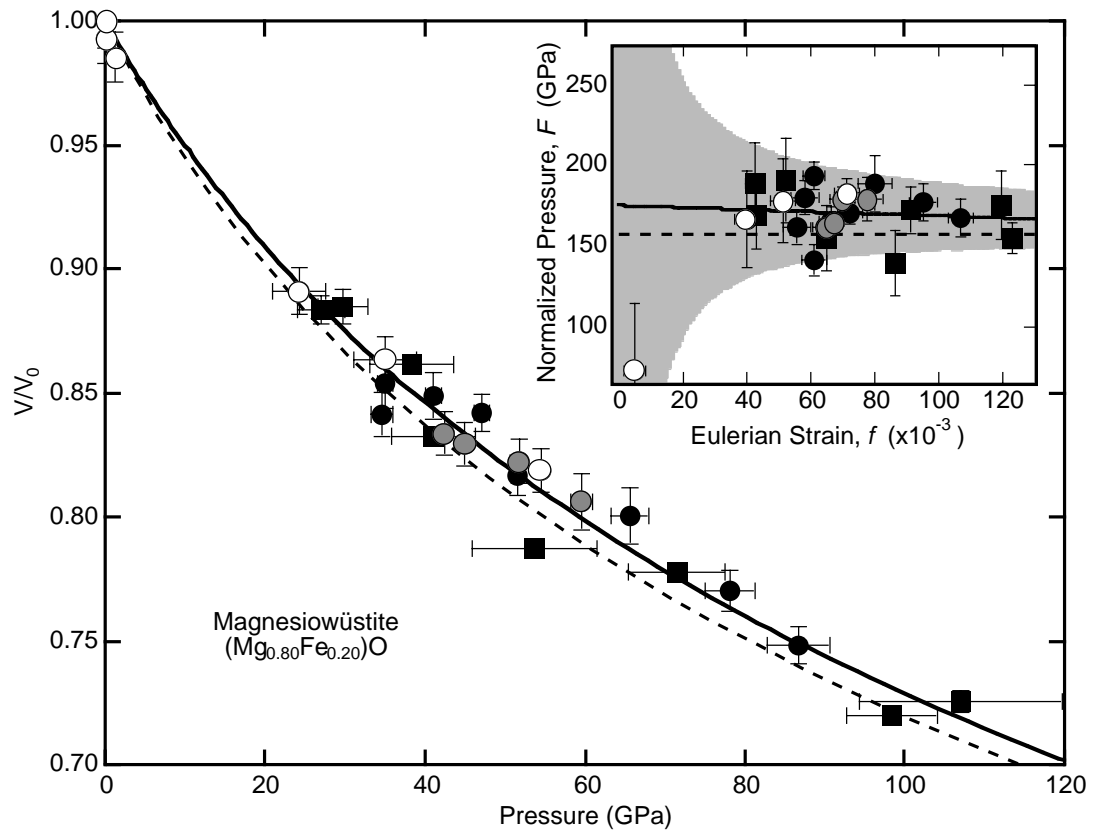


Fig. 1-3

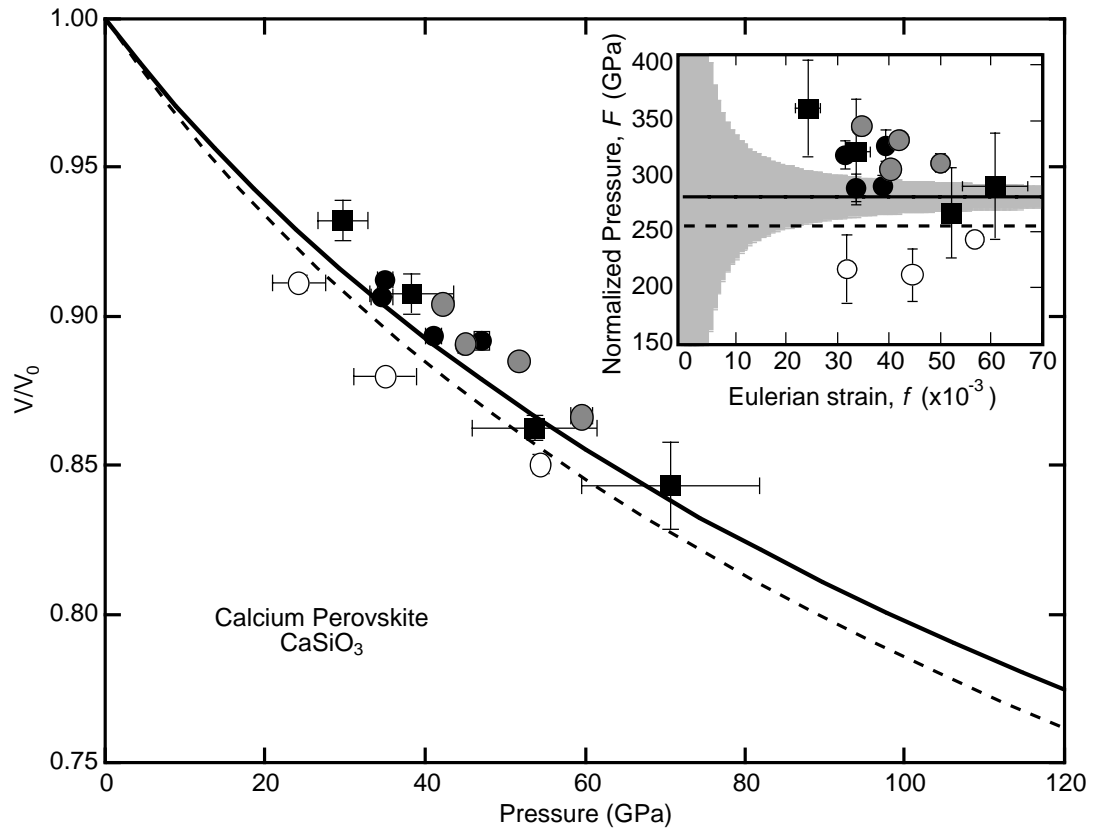


Fig. 1-4

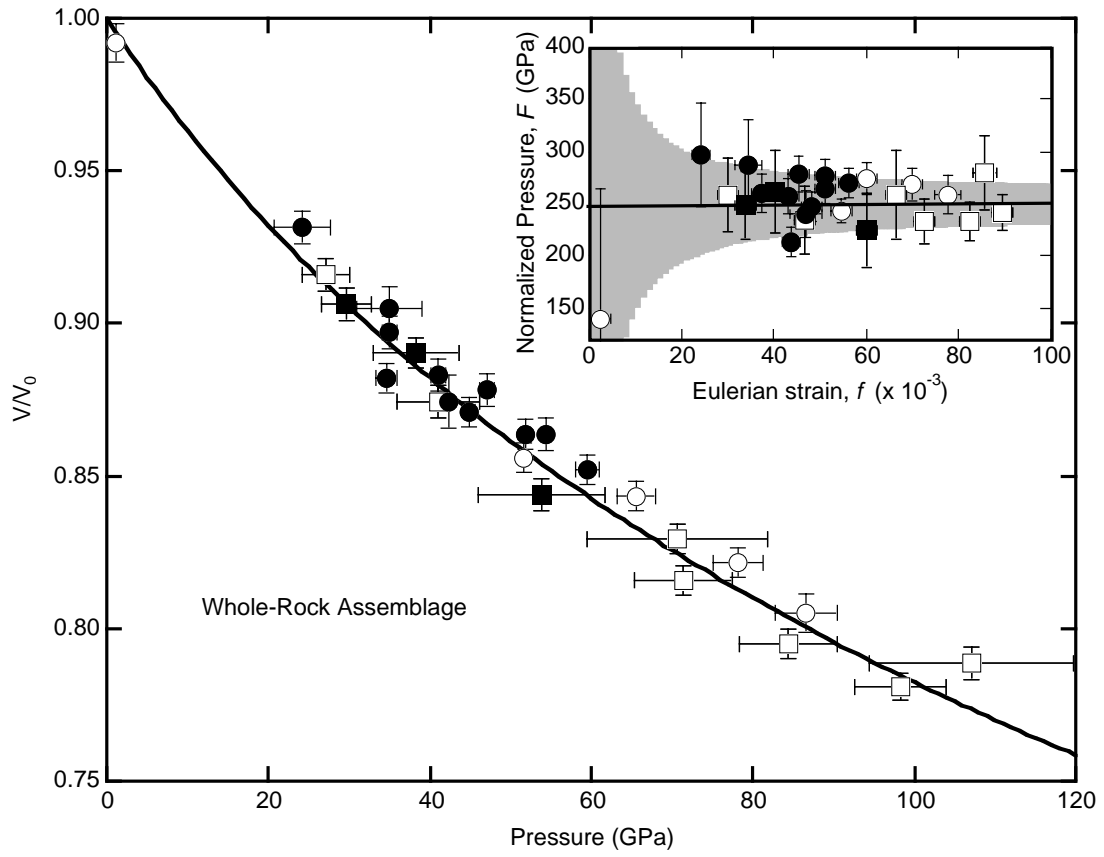


Fig. 1-5

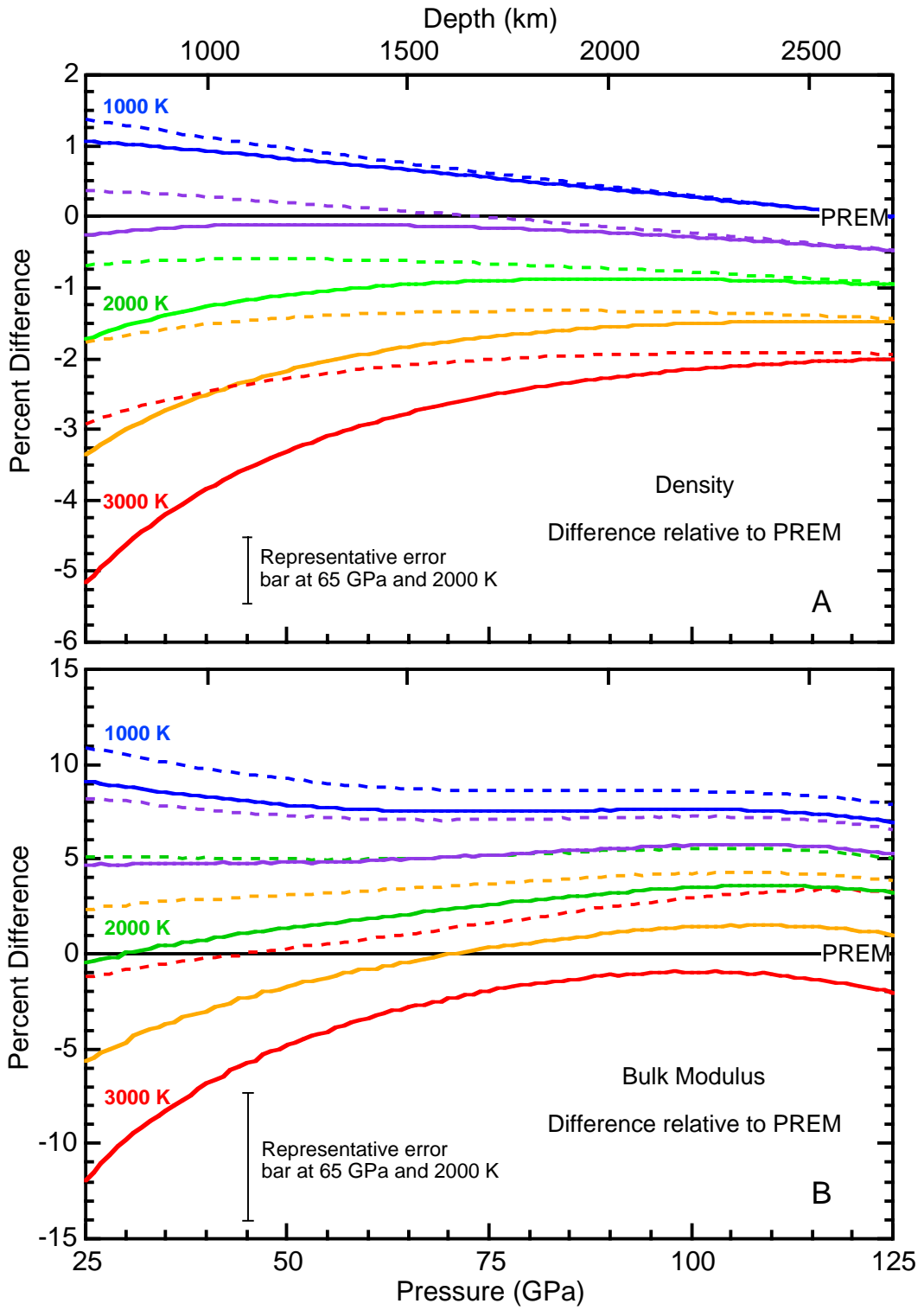


Fig. 1-6

Chapter 2: High-pressure alloying of potassium and iron: Radioactivity in the Earth's core?

***Abstract.** High-resolution x-ray diffraction provides evidence that potassium (K) alloys with iron (Fe) when the two pure elements are heated together at pressures above ~26 gigapascals (GPa). Increases of 2-3% in volume of the ϵ (hexagonal close packed: hcp) high-pressure phase of Fe can be attributed to the incorporation of ~1 atomic% (~7000 ppm by weight) K into Fe. Our results provide experimental support for predictions, derived from quantum mechanical calculations, that pressure can induce the alloying of K with Fe due to a change in the chemical-bonding character of K from alkaline- to transition-metal. Radioactive decay through the incorporation of ^{40}K into the core could therefore be an important source of energy deep inside the Earth, helping to power the geodynamo and mantle dynamics.*

Introduction

Two sources of heat drive the thermal, tectonic and geochemical evolution of the Earth: the release of gravitational potential energy and the decay of naturally occurring radioactive nuclides. The first includes the energy associated with accretion and differentiation of the planet. Its magnitude is hard to quantify, because doing so requires a detailed understanding of the Earth's formation and earliest evolution. The role of radioactive heating is potentially easier to estimate, based on chemical analyses of crust and mantle rocks and of meteorites.

A detailed study of terrestrial and chondritic samples [*Wasserburg et al.*, 1964] found that the K/U (potassium/uranium) ratios of $\sim 1 \times 10^4$ on Earth are distinct from the 8×10^4 ratio found in chondrites. If one is to assume a chondritic model for the Earth, where did the rest of the potassium go? Some have argued that because potassium is a moderately volatile element, it is depleted due to the high temperatures present during accretion [*McDonough and Sun*, 1995; *Newsom*, 1995]. On the other hand, [*Humayun and Clayton*, 1995] found that although there is a wide range of K/U ratios between chondritic, lunar and Earth samples, potassium isotopic ratios barely vary. This finding suggests that evaporation cannot be responsible for the depletion of K in the terrestrial planets, as a mass-dependent depletion of the isotopes would then be expected.

Alternatively it has been suggested that the K “missing” from mantle rocks may have been segregated into the Earth’s core [*Hall and Murthy*, 1971; *Lewis*, 1971]. Indeed, quantum mechanical calculations [*Bukowinski*, 1976] as well as experiments show that the chemical bonding in potassium changes under pressure [*Ito et al.*, 1993; *Parker et al.*, 1996; *Takemura and Syassen*, 1983]. The change in electronic structure with pressure (from 4s-like to 3d-like bonding orbitals) makes potassium more like a transition metal, hence increasing its tendency to alloy with other transition metals such as iron [*Parker et al.*, 1997]. This electronic transition is bracketed by two structural phase changes, from KII to KIII structures at 11.6 and 23 GPa, respectively [*Winzenick et al.*, 1994]. Once above this transition, potassium can bond with iron according to previous quantum mechanical calculations [*Bukowinski*, 1976]. However, there have been more recent theoretical calculations [*Sherman*, 1990] which do not find an increased affinity of K for Fe at high pressure for the composition KFe_{14} . Although we do not fully

understand this apparent discrepancy, it may be due to the calculation being for a large amount of K alloyed with Fe (large relative both to what experiment reveals, and to the maximum amount indicated for the core based on cosmochemical grounds).

The change in bonding character of elemental potassium is an important result for chemistry, but it is more geophysically interesting to determine whether K could partition into and alloy with the iron-rich core of the Earth. The radioactive isotope ^{40}K decays by β -decay to ^{40}Ca :



and to ^{40}Ar by electron capture and positron emission:



Potassium is also relatively abundant in nature and has a long half-life (~1.25 billion years), so it serves as an important heat source over all of Earth's history. If present in the Earth's core, potassium could be a major source of energy for the geodynamo that creates our planet's magnetic field, and even for mantle plumes and convection.

Experiment

Experimental Methods

Potassium (ingot packaged under argon, >99.95% pure, Aldrich) and iron powder (>99.9% pure, Alfa Products) were mixed and loaded under an argon atmosphere into a pre-compressed rhenium (Re) gasket in a diamond-anvil cell. Ruby grains (< 10 μm in diameter, and smaller than the pre-compressed gasket thickness of 30-45 μm in order to avoid diamond bridging) were placed into the sample chamber for pressure calibration [Mao *et al.*, 1978]. Liquid argon (Ar) was loaded cryogenically as a pressure medium

and thermal insulator. At each pressure above ~26 GPa, the samples were laser-heated to temperatures > 2500 K (above the melting point of iron and potassium) with a Nd-YAG laser ($\lambda = 1064$ nm) to synthesize the alloy and alleviate any deviatoric stresses. In one run, we also laser heated at lower pressures (13.2, 19.8, 25.1 GPa). High-pressure x-ray diffraction patterns were collected at room temperature on image plates at beamline 10-2 of the Stanford Synchrotron Radiation Laboratory, and at beamline 7.3.3 of the Advanced Light Source. Great care was taken to measure the sample-to-image plate distance, determined by Au diffraction, for each diffraction pattern taken (an Au calibration foil was placed on the backside of the diamond closest to the image plate, and the thickness of the diamond was taken into account). We performed six different experimental runs to verify the reproducibility of our results. Separate experiments on only K were also performed using the above methodology, and confirm that K is not amorphous after laser-heating above 26 GPa.

X-Ray Diffraction Measurements

At low pressures, the phases of K [Liu, 1986; Takemura and Syassen, 1983; Winzenick et al., 1994] and Fe [Jephcoat et al., 1986; Mao et al., 1990; Takahashi et al., 1968; Wilburn and Bassett, 1978] are identifiable by their most intense x-ray diffraction peaks (Figure 2-1). Diffuse and broad diffraction lines at the lowest pressure, with d-spacings between ~2.2 and 2.6 Å, may be due to minor oxidation or hydration of the initial K, which is highly reactive. Below ~26 GPa, the measured unit-cell volumes are consistent with the equations of state for pure Fe and pure K (Figures 2-1 and 2-2).

After laser-heating above 26 GPa, however, the x-ray diffraction lines for K become much less intense, and the ϵ -Fe unit-cell volume is enlarged by 2-3% relative to

that for pure Fe (Figures 2-1 and 2-2). We can determine the K:Fe (by atomic percent) ratio at the lowest pressure by comparing the intensities of the diffraction peaks as estimated by Rietveld refinement: ~60:100 [*Larson and Von Dreele, 2000; Toby, 2001*]. The same sample, shown at 57.5 GPa in Figure 2-1, yields a much decreased K:Fe ratio of ~5:100, indicative of most of the K being incorporated into Fe.

To verify expansion of the Fe unit cell we also measured the compression of pure Fe, loaded in the same way as the K + Fe sample (including the use of an Ar pressure medium, and laser heating). We obtained results in good agreement with prior measurements [*Jephcoat et al., 1986*] on the volume of ϵ -Fe as a function of pressure (Figure 2-2).

Using the Birch-Murnaghan equation of state [*Birch, 1978*], holding $K_{0T}' = 4.0$ and assuming an initial volume (V_0) expanded by 2.1 (± 0.6)% (in line with the average expansion we observe at high pressures), we find a zero-pressure room-temperature isothermal bulk modulus $K_{0T} = 196 (\pm 11)$ GPa for the enlarged ϵ -Fe phase (black dashed curve in Figure 2-2). This is comparable to the values $K_{0T} = 165-193$ GPa obtained in previous studies [*Jephcoat et al., 1986; Mao et al., 1990*] for pure ϵ -Fe, assuming $V_0 = 11.173 \text{ \AA}^3$.

Upon opening the cell at zero pressure, all that is recovered within the Re gasket exhibits only diffraction from Fe and numerous weak diffraction peaks from potassium oxides (K_2O , KO_2 , $KFeO_2$, K_2FeO_4), likely due to the immediate oxidation of any unalloyed K upon quench. The ϵ -Fe we recover has a slightly expanded unit cell, perhaps due to K remaining incorporated in the Fe upon quenching: the ambient-pressure volume we measure is 0.3 (± 0.1)% larger than that expected for pure ϵ -Fe. For comparison, the

Re unit-cell volume is as expected [Donohue, 1974], suggesting that the potassium did not alloy with the Re gasket (in contrast with other, much smaller elements like hydrogen [Benedetti and Jeanloz, 2000]). Rietveld analysis confirms that the amount of K left over (now in the form of oxides) corresponds to a K:Fe ratio of $\sim 5:100$, in good agreement with the K:Fe ratio observed at 57.5 GPa from which it was quenched.

Three separate samples exhibited a decrease in K diffraction intensities, and increase in Fe lattice parameters, upon heating at pressures above ~ 26 GPa. The atomic ratios of K:Fe determined from Rietveld fitting decreased from 56 (± 14), 17 (± 5) and 23 (± 1)% to 10 (± 5), 8 (± 2) and 5 (± 3)% respectively. Finally, in a separate experiment, we confirmed that a sample of K + Fe taken directly to 35.6 GPa only exhibits a decrease in K diffraction intensities and expansion in Fe unit-cell volume after heating.

Analysis

For hexagonal close-packed (hcp) materials, interstitial occupation can occur with either tetrahedral or octahedral coordination [Smallman *et al.*, 1988]. However, interstitial atoms (in our case, K) must be smaller than the hcp atoms (Fe): K tetrahedral radius $\leq 0.225 \times (\text{Fe hcp radius})$, K octahedral radius $\leq 0.414 \times (\text{Fe hcp radius})$. Even at our experimental pressures, the atomic radius of K is too large for interstitial occupation (at 50 GPa, $r_K = 1.75 \text{ \AA}$ compared to $r_{Fe} = 1.18 \text{ \AA}$) [Winzenick *et al.*, 1994]. This is an approximation, however, as the K radius may change upon combining with Fe. Even so, the pure K radius for our experimental pressure range is more than three (six) times larger than allowed for octahedral (tetrahedral) coordination. Thus we can rule out interstitial occupation because the atomic volume of K is much larger than that of Fe, even at our experimental pressures.

For substitution, we must also be aware of the atomic sizes. The first of the empirical Hume-Rothery rules states that the atomic radii of the alloying elements must be within ~15% of each other, otherwise the solid solution formed will be restricted to a few atomic percent [*Hume-Rothery*, 1963]. Although the size-factor is unfavorable for K, limited solid-solution is still possible with Fe. For substitution, we compare the hcp volume of ϵ -Fe with the volume of a hypothetical hcp phase of K. Assuming Vegard's Law [*Vegard*, 1921], a linear relationship between volume and composition (in atomic percent), we find that in order to increase the ϵ -Fe unit cell volume by 2-3% we must substitute ~1% of the Fe atoms with K. This ~1% substitution is compatible with the first of the Hume-Rothery rules, though it may be a lower bound because most solid solutions have a concave response to concentration increase (greater than a linear growth) rather than a linear response [*Smallman et al.*, 1988].

This amount of K that apparently can be dissolved into Fe, ~7000 ppm (0.7 (\pm 0.2) wt%), is far larger than the amount of K sequestered into the core according to cosmochemical estimates (~1200 ppm; see discussion in [*Gessmann and Wood*, 2002]). It is also larger than the amount that has been experimentally determined to partition into iron-sulfide in previous experiments, conducted at lower pressures than ours ($\sim 10^2$ ppm; [*Gessmann and Wood*, 2002; *Murthy et al.*, 2003]). The pressures of the earlier experimental studies were too low (< 26 GPa) for the $s \rightarrow d$ electronic transfer to be complete. Ito et al. [*Ito et al.*, 1993] measured the dissolution of K into molten iron sulfide at 26 GPa and 2900 K, and found partitioning of K into Fe ($D_K = 3.8 \times 10^{-2}$) corresponding to 5 ppm in the Earth's core. However, as Murthy et al. [*Murthy et al.*, 2003] have shown, the distribution coefficient is highly dependent on time and on

polishing methods, thus the equilibrium abundance of K in liquid Fe could actually be much higher than measured by Ito et al. (e.g., by more than one order of magnitude). One might therefore expect that if future partitioning experiments are done at pressures above 26-30 GPa, the partitioning of K into iron sulfide would be greater. A shock-wave study of KFeS_2 has shown a similar transition from a “low-pressure regime” to a “high-pressure regime” between ~20-30 GPa, possibly due to the transition-metal tendencies of K at those conditions [Somerville and Ahrens, 1980].

Discussion and Conclusions

There are several scenarios for core formation (e.g., blobs, percolation, diapirs, magma-fracturing; for more details see [Stevenson, 1990]) which suggest that iron droplets formed and settled through the mantle, possibly at the base of a magma ocean. The base of this magma ocean is inferred to have been at a depth of ~400 to 1000 km (~15-35 GPa) and at temperatures of 2200-3000 K [Ohtani, 1985]. Our experiments show that K can alloy with Fe above pressures of ~26 GPa and temperatures above 2500 K, compatible with the base of a magma ocean environment. Although we have shown that potassium and iron alloy at deep magma-ocean conditions, without the presence of sulfur or high oxygen fugacities [Gessmann and Wood, 2002; Murthy et al., 2003], partitioning between silicate and metal also needs to be taken into account. However, uncertainties in the relevant phases and compositions (e. g., light elements in the forming core, nature of silicate and oxide phases that were present) mean that significant assumptions are required if one is to more quantitatively evaluate the partitioning of K between the early core and mantle.

Recent core-energetics calculations [*Breuner and Spohn, 1993; Buffett, 2002; Labrosse et al., 2001; Nimmo et al., in press 2003*] suggest that some amount of radioactivity may be compatible with – or even necessary for – producing the Earth’s early magnetic field. Likely candidates for radioactivity in the core are potassium, uranium and thorium (Th). Potassium’s relative abundance and now-demonstrated affinity for iron make it a plausible source of radioactive heat in the core. Following Verhoogen [*Verhoogen, 1980*], the 7000 ppm maximum amount of K indicated to alloy with Fe from our experiments would currently yield approximately 45 terawatts (TW) of power if present throughout the core: more than the ~40 TW currently being lost at the Earth’s surface.

Our experiments only provide an upper limit to the amount of K that might be present in the core, because we have not taken into account the partitioning between silicate and metal phases. Moreover, this amount of potassium is at least one order of magnitude greater than is necessary to satisfy calculated energy requirements to sustain the geodynamo [*Buffett, 2002*], as well as being greater than cosmochemical estimates. As core differentiation probably began before accretion was complete, the pressure and temperature conditions may not have been favorable early on to alloy potassium and iron, until accretion was nearly finished. Therefore, although we find a high amount of K (relative to that required) alloying with Fe at pressures greater than 26 GPa and temperatures above 2500 K, much of the core could have already formed before the conditions were such that potassium could begin to alloy. Geochemically-based estimates of the abundance of K in the core, 1200 ppm, yield 8 TW of power being currently released, and 100 TW being released from the core 4.5 billion years ago

[*Gessmann and Wood, 2002*]. Considering that U and Th could additionally be present in the core, a much larger amount of radioactive heating than previously recognized could thus be powering the geodynamo, as well as the dynamics of the overlying mantle, throughout geological history.

References

- Benedetti, L.R., and R. Jeanloz, Science and Technology of High Pressure, edited by M.H. Manghnani, W.J. Nellis, and M.F. Nicol, pp. 939-940, Universities Press, 2000.
- Birch, F., Finite strain isotherm and velocities for single crystal and polycrystalline NaCl at high pressures and 300 K, *Journal of Geophysical Research*, 83, 1257-1268, 1978.
- Breuner, D., and T. Spohn, Cooling of the Earth, Urey ratios, and the problem of potassium in the core, *Geophysical Research Letters*, 20 (15), 1655-1658, 1993.
- Buffett, B.A., Estimates of heat flow in the deep mantle based on the power requirements for the geodynamo, *Geophysical Research Letters*, 29 (12), 10.1029, 2002.
- Bukowinski, M.S.T., The effect of pressure on the physics and chemistry of potassium, *Geophysical Research Letters*, 3, 491-503, 1976.
- Donohue, J., *The Structure of the Elements*, Wiley, New York, 1974.
- Gessmann, C.K., and B.J. Wood, Potassium in the Earth's core?, *Earth and Planetary Science Letters*, 200, 63-78, 2002.
- Hall, H.T., and V.R. Murthy, The early chemical history of the Earth: Some critical elemental fractionations, *Earth and Planetary Science Letters*, 11, 239-244, 1971.
- Humayun, M., and R.N. Clayton, Potassium isotope cosmochemistry: Genetic implications of volatile element depletion, *Geochimica et Cosmochimica Acta*, 59 (10), 2131-2148, 1995.
- Hume-Rothery, W., *Electrons, Atoms, Metals and Alloys*, 387 pp., Dover Publications, New York, 1963.

- Ito, E., K. Morooka, and O. Ujike, Dissolution of K in molten iron at high-pressure and temperature, *Geophysical Research Letters*, 20 (15), 1651-1654, 1993.
- Jephcoat, A.P., H.-K. Mao, and P.M. Bell, Static compression of iron to 78 GPa with rare gas solids as pressure-transmitting media, *Journal of Geophysical Research*, 91 (B5), 4677-4684, 1986.
- Labrosse, S., J.-P. Poirier, and J.-L. Le Mouel, The age of the inner core, *Earth and Planetary Science Letters*, 190, 111-123, 2001.
- Larson, A.C., and R.B. Von Dreele, Los Alamos National Laboratory Report No. LAUR 86-748, LANL, 2000.
- Lewis, J.S., Consequences of the presence of sulfur in the core of the Earth, *Earth and Planetary Science Letters*, 11, 130-134, 1971.
- Liu, L.-G., Compression and polymorphism of potassium to 400 kbar, *Physical Chemistry of Solids*, 47 (11), 1067-1072, 1986.
- Mao, H.-K., P.M. Bell, J. Shaner, and D.J. Steinberg, Specific volume measurements of Cu, Mo, Pd, and Ag and calibration of the ruby R1 fluorescence pressure gauge from 0.06 to 1 Mbar, *Journal of Applied Physics*, 49, 3276-3283, 1978.
- Mao, H.-K., Y. Wu, L.C. Chen, J.F. Shu, and A.P. Jephcoat, Static compression of iron to 300 GPa and Fe_{0.8}Ni_{0.2} Alloy to 260 GPa: Implication for the composition of the core, *Journal of Geophysical Research*, 95, 21737-21742, 1990.
- McDonough, W.F., and S.-s. Sun, The composition of the Earth, *Chemical Geology*, 120, 223-253, 1995.
- Murthy, V.R., W. van Westrenen, and Y. Fei, Radioactive heat sources in planetary cores: Experimental evidence for potassium, *Nature*, 423, 163-165, 2003.

- Newsom, H.E., Composition of the solar system, planets, meteorites, and major terrestrial reservoirs, in *Global Earth Physics, A Handbook of Physical Constants, AGU Reference Shelf 1*, edited by T.J. Ahrens, pp. 159-189, American Geophysical Union, Washington, D. C., 1995.
- Nimmo, F., G.D. Price, J. Brodholt, and D. Gubbins, The influence of potassium on core and geodynamo evolution, *Geophysical Journal International*, in press 2003.
- Ohtani, E., The primordial terrestrial magma ocean and its implication for stratification of the mantle, *Physics of the Earth and Planetary Interiors*, 38 (1), 1985.
- Parker, L.J., T. Atou, and J.V. Badding, Transition element-like chemistry for potassium under pressure, *Science*, 273, 95-97, 1996.
- Parker, L.J., M. Hasegawa, T. Atou, and J.V. Badding, High-pressure synthesis of alkali metal-transition metal compounds, *European Journal of Solid-State & Inorganic Chemistry*, 34 (7-8), 693-704, 1997.
- Sherman, D.M., Chemical bonding and the incorporation of potassium into the Earth's core, *Geophysical Research Letters*, 17 (6), 693-6, 1990.
- Smallman, R.E., W. Hume-Rothery, and C.W. Haworth, *The Structure of Metals and Alloys*, Institute of Metals, London, 1988.
- Somerville, M., and T.J. Ahrens, Shock compression of KFeS_2 and the question of potassium in the core, *Journal of Geophysical Research*, 85 (B12), 7016-7024, 1980.
- Stevenson, D.J., Fluid Dynamics of core formation, in *Origin of the Earth*, edited by H.E. Newsom, and J.E. Jones, pp. 231-250, Oxford University Press, New York, 1990.

- Takahashi, T., W.A. Bassett, and H.-K. Mao, Isothermal compression of the alloys of iron up to 300 kbar at room temperature: iron-nickel alloys, *Journal of Geophysical Research*, *73*, 1968.
- Takemura, K., and K. Syassen, High-pressure phase transitions in potassium and phase relations among heavy alkali metals, *Physical Review B*, *28* (2), 1193-1196, 1983.
- Toby, B.H., EXPGUI, a graphical user interface for GSAS, *Journal of Applied Crystallography*, *34*, 210-13, 2001.
- Vegard, L., The constitution of mixed crystals and the space occupied by atoms, *Z. Phys.*, *5* (17), 17-26, 1921.
- Verhoogen, J., *Energetics of the Earth*, 139 pp., National Academy of Sciences, Washington, D. C., 1980.
- Wasserburg, G.J., G.J.F. MacDonald, F. Hoyle, and W.A. Fowler, Relative contributions of Uranium, Thorium, and Potassium to heat production in the Earth, *Science*, *143*, 465-467, 1964.
- Wilburn, D.R., and W.A. Bassett, Hydrostatic compression of iron and related compounds: an overview, *American Mineralogist*, *63*, 591-596, 1978.
- Winzenick, M., V. Vijayakumar, and W.B. Holzapfel, High-pressure x-ray diffraction on potassium and rubidium up to 50 GPa, *Physical Review B*, *50* (17), 12381-12385, 1994.

Figure 2-1. X-ray diffraction patterns at 5.9, 15.3 and 25.9 GPa prior to heating (thin curves), and at 26.3 and 57.5 GPa after laser-heating (thick curves). The expected diffraction-peak locations are labeled for the three phases of potassium: KI, KII, KIII, and for both phases of Fe (thick vertical lines). At the highest pressure, an example of the offset of the Fe peak position with that of the Fe-K alloy (thin vertical line) is displayed. The large peak at $\sim 2.4 \text{ \AA}$ at 25.9 GPa is due to diffraction from the argon pressure medium.

Figure 2-2. Iron unit-cell volumes observed for K + Fe samples, prior to heating above the sample solidi (solid circles) and after heating above the sample solidi (open circles), are compared with those for pure Fe (solid squares). Solid circles at pressures of 13.2, 19.8 and 25.1 GPa were also laser heated (but to lower than the melting temperature of iron) and do not show evidence of volume expansion. Below ~ 26 GPa and before heating, and at all pressures (measured after heating) for pure Fe, our measurements are in good agreement with prior results for the α (bcc: thin curve, [Takahashi *et al.*, 1968]) and ϵ (hcp: thick curve, [Jephcoat *et al.*, 1986]; dash-dot curve, [Mao *et al.*, 1990]) phases of pure Fe. Dashed curve is the Birch-Murnaghan equation of state for the expanded hcp unit-cell observed after heating Fe with K at pressures above 26 GPa. Phase-transition pressures are indicated by vertical lines for Fe (solid) and K (dashed) (see also Figure 2-1), with phase stability ranges labeled in between. Shaded vertical bar at $26 (\pm 3)$ GPa is our K-Fe alloy transition pressure. **Inset.** Percent volume deviation from the expected volume for Fe [Jephcoat *et al.*, 1986; Takahashi *et al.*, 1968]. Horizontal dashed lines at 0 and 2.1 (± 0.6)% volume deviation correspond to no

deviation, as observed for the volumes of unalloyed Fe (closed circles), and the average percent volume deviation of the Fe-K alloy volumes (open circles). Detailed analysis of the diffraction patterns of K + Fe heated at pressures above ~26 GPa show that the expansion of the hcp unit cell of Fe cannot be ascribed to overlap of diffraction lines from K III, Ar or the gasket.

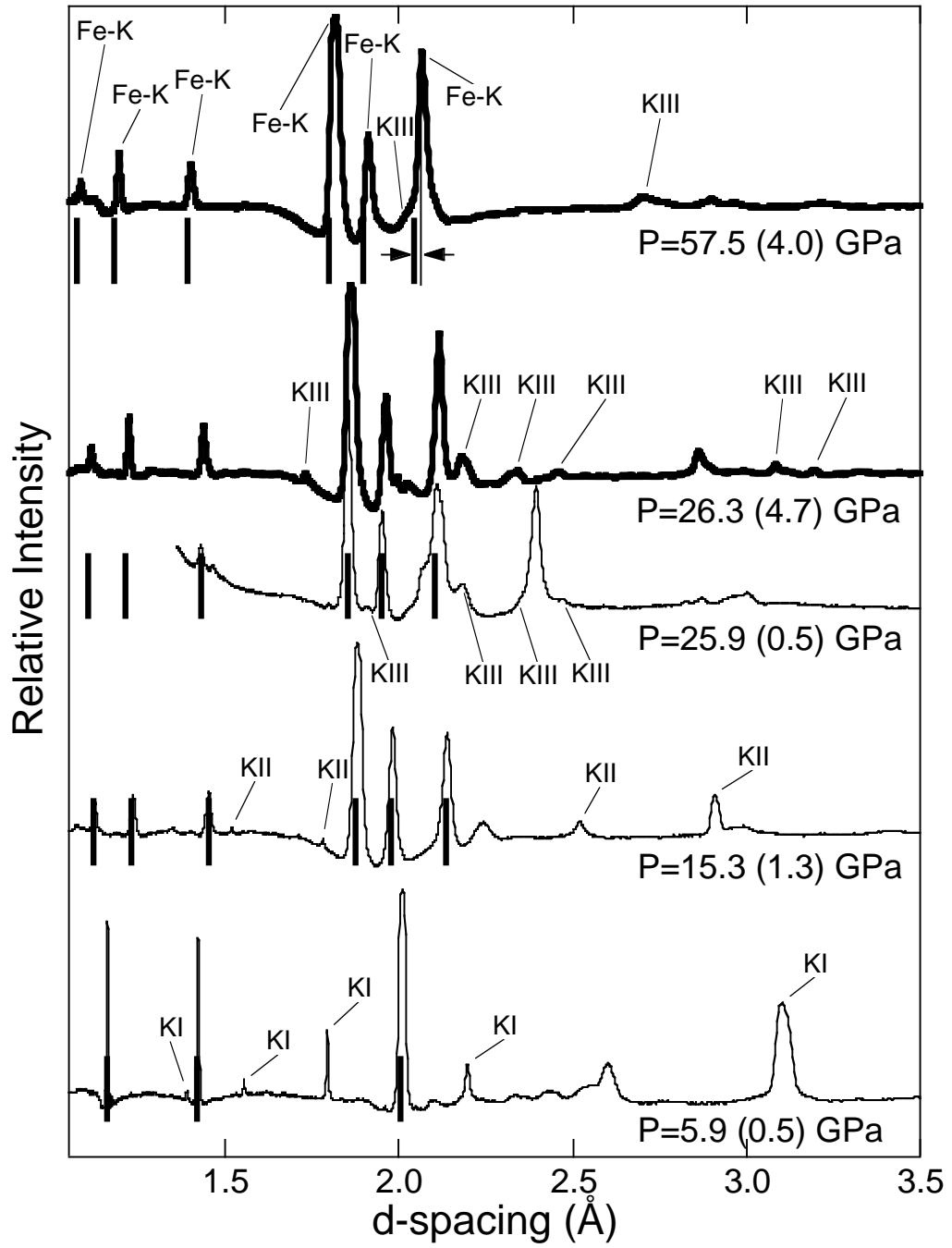


Figure 2-1

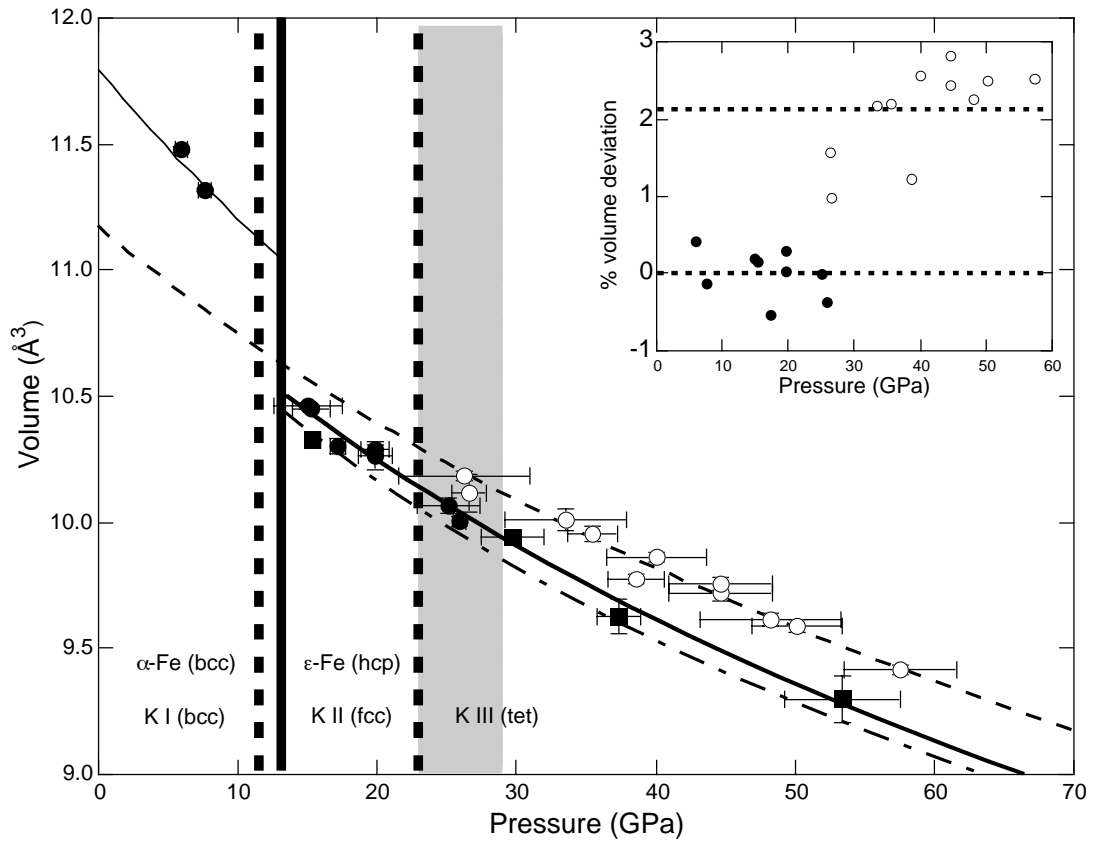


Figure 2-2

Part II: Exploring Icy Giants

Forming icy giant interiors: Laser-driven shock waves on pre-compressed water

***Abstract.** Laser-driven shock compression of pre-compressed water (up to 1 GPa pre-compression) produces high-pressure, -temperature conditions in the water inducing two optical phenomena: opacity and reflectivity in the initially transparent water. The onset of reflectivity is interpreted as the ionic \rightarrow metallic transition in water and is found at pressures above ~ 150 GPa and calculated temperatures above ~ 9000 K.*

Introduction

Although the giant gas planets are mostly comprised of hydrogen and helium, the icy giants Neptune and Uranus are additionally believed to contain as much as $\sim 50\%$ water (by mass) and significant amounts of methane and ammonia [Hubbard, 1984]. Most of the water is in a dense, fluid state, forming an “icy” interior layer with pressures ranging between 10 and 500 GPa and temperatures between 2000 and 5000 K [Hubbard, 1997]. “Ice” refers to the presence of molecular species, such as water, methane or ammonia, and it is theorized that it is in this icy layer that the planet’s magnetic field is produced.

Planetary magnetic fields are prevalent in our solar system, and can be expected to be important to extra-solar planets as well [Stevenson, 2003]. Magnetic fields can be produced by three mechanisms: permanent magnetism, which is produced at the microscopic level and is inherent to the material (e. g., ferromagnetism); induction from external sources; or by production through electrical currents generated by a dynamo. Although some of the magnetism in our Solar System can be attributed to permanent magnetism from iron-rich minerals (e.g., Moon and Mars) or by induction by varying

external magnetic fields (Galilean satellites), most must be formed by a dynamo sustained by convection of an electrically conducting fluid deep inside the planet.

The magnetic fields of Neptune and Uranus were first measured during the 1980's Voyager missions [*Stone and Miner, 1989*]. The surface field was shown to be about the same for both planets, $\sim 2 \times 10^{-5}$ T, comparable in strength to the Earth's magnetic field value of $\sim 5 \times 10^{-5}$ T. Although it is expected that the icy giants have a core of rock and metal about the size of the Earth, the mostly quadrupolar nature of the observed magnetic field suggests that an Earth-like iron-dominated geodynamo at the center of the planet is unlikely to be the source of the magnetism [*Hubbard, 1984*]. Instead, it is theorized that an ionized or perhaps a metallic form of water, existing at high pressures and temperatures in the shallower levels of the planet, likely sustains the necessary electric currents for the planetary dynamo.

Pure water is normally thought of as an insulator. At ambient conditions its resistivity is quite low, only 2.5×10^7 ohm-centimeters ($\Omega\text{-cm}$), yet this is still about 12 orders of magnitude less conductive than iron [*Lide, 1990*].

The high-pressure and high-temperature environment of the planetary interior has been simulated in the laboratory with diamond-anvil cells and shock-wave experiments. Successful diamond-cell experiments on water have been carried out to 210 GPa at temperatures near 300 K [*Goncharov and Struzkhin, 1996*] or at lower pressures but higher temperatures [*Benedetti, 2001*], leaving most of the pressure range relevant to the icy layer untouched. Shock waves produce high pressures (> 100 GPa) and temperatures ($> 10,000$ K) in the sample for a short time (ns – μ s). Unfortunately, the temperatures reached through shock-compression tend to be unrealistically high for the interior layer

of “ice.” Reverberating shock experiments on water have reached 180 GPa and 10700 K [Chau *et al.*, 2001], although previous gas gun shock experiments were limited to pressures below 100 GPa [Lyzenga *et al.*, 1982; Mitchell and Nellis, 1982; Volkov *et al.*, 1980]. Early Soviet shock experiments (likely produced by nuclear explosions) reached up to 3200 GPa [Avrorin *et al.*, 1981; Podurets *et al.*, 1972]. More recently, laser-driven shock experiments on water have reached pressures up to nearly 800 GPa with estimated temperatures of up to 80,000 K [Celliers *et al.*, submitted, 2003].

Static compression yields an isothermal equation of state (EOS), while dynamic (shock-wave) methods yield a different EOS (Hugoniot) characteristic of the high temperatures that are reached. By combining dynamic and static methods, laser-driven shock experiments on pre-compressed samples access conditions unreachable by either static or dynamic high-pressure techniques alone, and allow the investigation of a broad range of P-V-T space [Lee *et al.*, 2002; Loubeyre *et al.*, 2004]. By knowing the initial pressure and density of the pre-compressed sample, it is possible to infer the conditions achieved in the sample under shock compression via the Hugoniot Relations [Zeldovich and Raizer, 1967].

Here we present EOS and optical measurements using laser-driven shock waves on pre-compressed samples of water. The EOS measurements are expected to lie between the isentrope and Hugoniot of water, due to the increased initial density of the pre-compressed sample, thereby recreating the conditions of the icy layers of Neptune and Uranus. We also observe optical reflectivity changes in the water as the shock wave propagates through the sample, providing evidence for the molecular → ionic → metallic transition expected to occur in H₂O under conditions relevant for the production of

magnetic fields in the icy giants [*Cavazonni et al.*, 1999; *Celliers et al.*, 2000; *Hicks et al.*, 2003].

Methods

The sample consists of a layer of doubly-distilled ultra-pure water compressed between diamond windows, with an aluminum piece embedded in the water layer and placed against the diamond window from which the shock enters. The aluminum piece is used for calibration of the shock-wave velocity and is stepped, such that it has two distinct thicknesses across which the entering shock wave traverses before entering the water. Modified diamond cells fit with 200-500 μm thick, 1.0 mm wide diamond windows, were used to compress water to a finite initial density and pressure (see Table 3-1) and were shocked by a high-power laser pulse. Detailed experimental techniques of the design of the pre-compressed targets is described in Appendix B [*Lee et al.*, 2002]. These experiments were performed at the Vulcan Laser Facility at the Rutherford Appleton Laboratory. Shots preceded by “00,” were shocked with a 4 ns square laser pulse, whereas shots preceded by “01” were shocked with a 1 ns square pulse. The longer duration pulses allow for a more steady shock throughout the sample; the short pulses allow for stronger shocks, which are, however, decaying by the time they reach the water sample.

For each shot, there were three probes monitoring the sample: two VISAR interferometers (Figure 3-1) and one optical pyrometer, as described earlier [*Barker and Hollenbach*, 1972; *Celliers et al.*, 1998; *Loubeyre et al.*, 2004]. For shots preceded by

“00,” both interferometers were filtered to 532 nm, whereas shots preceded by “01” were recorded by interferometers at 532 nm and 1064 nm.

A streaked optical pyrometer was also used to measure the black-body radiation emitted from the shocked sample. Care was taken to calibrate the camera, the beam path and optics against a tungsten lamp in order to determine the intensity versus temperature at a wavelength of 650 nm. As we only collected blackbody radiation at one wavelength, a constant emissivity of 1 is assumed for opaque samples, whereas for transparent and reflecting samples, the emissivity is decreased from unity as described elsewhere [Kormer, 1968]. Temperature measurement is difficult, and uncertainties on the temperature are ~20%. We find our temperature measurements are in fairly good agreement with predictions [Ree, 1976], available in the SESAME database, T_{Sesame} , [Lyon and Johnson, 1992], while the water is still transparent (Table 3-1, Figure 3-2). The agreement decreases with increasing pressure (opaque and reflecting samples). The model overestimates the temperatures by about 5000 K at the highest experimental pressures (black circles in Figure 3-2) and may indicate a measured non-equilibrium temperature caused by electron screening of the thermal radiation [Grigor'ev et al., 1985].

Analysis

An example of raw data recorded from the VISAR shows the intensity recorded at the streak camera slit as a function of time (Figure 3-1). The first two fringe discontinuities are due to the Doppler shift of the now-moving Al step surface into the water. Successive discontinuities are due to the shock wave hitting the back surface of

the diamond, thereby causing another Doppler shift. To extract velocity measurements, both the Fourier-transform method, which yields a velocity-per-fringe (VPF) relation [Takeda *et al.*, 1982], and direct velocity determination using Al step heights divided by transit time were used (e.g., [Trunin, 2001]). Initial conditions, measured velocities, and final conditions as determined by the Hugoniot relations are listed in Table 3-1. The index of refraction of the pre-compressed water was calculated and taken into account when measuring the shock velocities, varying with pressure from 1.37 to 1.45 and up from the ambient-condition value of 1.33 [Dewaele *et al.*, 2003].

The uncertainties in measuring the Al shock velocity (and in determining the particle velocity of Al) stem from the uncertainties of knowing the Al step height, the index of refraction of the compressed water and our ability to determine the breakout times in each of the two interferometers. These amount to no more than 10%, and routinely ~5%. Additional uncertainties in the water velocities are minimized due to the redundant interferometers, each having their own VPF relation, but can be as large as 7%. Combining all of the uncertainties, the final pressure and density uncertainties in the water are up to 12% but usually less than 10%.

Reflectivity is estimated by determining the intensity of light measured after the shock breaks out from the Al step (reflectivity of ~81% in the green) [Bessarab *et al.*, 1978]. In samples that are still transparent ($T_{\text{Sesame}} < \sim 3700$ K), the intensity of the light after breakout is nearly the same; that is the water continues to stay transparent to the light being reflected off of the moving Al step. For opaque samples (~ 3700 K $< T_{\text{Sesame}} < 9000$ K), the intensity of light after breakout drops to zero, whereas for reflecting samples ($T_{\text{Sesame}} > 9000$ K), there is some reflected light bouncing off of the now moving water

surface rather than the moving Al surface. This is inferred by the reduced intensity of light reflecting off the moving water surface and corresponds to pressures (and therefore temperatures) that are greater than those of opaque samples (Figures 3-1, 3-2). Uncertainties in reflectivity are up to 10%.

To compare with a theoretical model of water [Cavazzoni *et al.*, 1999], samples that are transparent may be inferred to be superionic, whereas opaque samples are ionic and reflecting samples are metallic (Figure 3-2). This is somewhat consistent with earlier shock-wave experiments on water, which demonstrated an increase in the electrical conductivity to $\sim 25 (\Omega\text{-cm})^{-1}$ of water with increasing pressure up to ~ 30 GPa and remaining constant until 60 GPa [Mitchell and Nellis, 1982]. More recent experiments at pressures between 70 and 180 GPa (via shock reverberation) show a slight increase in conductivity, from 30 to $210 (\Omega\text{-cm})^{-1}$, interpreted as being due to ionization of water: $\text{H}_2\text{O} \rightarrow \text{H}^+ + \text{OH}^-$ [Chau *et al.*, 2001]. The temperatures were measured in the former experiment and are up to 4100 K at 60 GPa [Lyzenga *et al.*, 1982]. In the latter experiment, the temperatures were not measured but are estimated to be $\sim 11,000$ K at the highest pressures and are likely comparable to our own temperatures because of the use of shock reverberation technique. To compare the conductivity of water with that of its components, shocked metallic hydrogen has a conductivity of $\sim 2000 (\Omega\text{-cm})^{-1}$ at 140 GPa [Weir *et al.*, 1996] and shocked metallic oxygen has a conductivity of $\sim 1000 (\Omega\text{-cm})^{-1}$ at 120 GPa [Bastea *et al.*, 2001]. Both studies suggest that metallization occurs in the molecular forms of each element, with limited dissociation to the monatomic state.

Reflectivity is indicative of the production of free carriers generated by thermal activation across a mobility gap, and can be modeled simply as thermal excitation across

a semiconductor energy gap ϵ_g [Kittel and Kroemer, 1980]. In two of our samples, we measured (at 1064 nm) a reflectivity in the shocked water of $\sim 35\%$ compared to $\sim 80\%$ in the aluminum step. Using the Fresnel formula, $R = |(n-n_0)/(n+n_0)|^2$, where $n_0 = 1.45$ is the index of pre-compressed water at 1 GPa, and $n = \sqrt{\epsilon}$, the square root of the dielectric function, we can estimate the number of carriers N_e and N_h (electrons and holes) per volume. The number of electrons per given volume at a pressure of ~ 150 GPa ($T_{\text{Sesame}} \sim 8000$ K), is $N_e = N_h \approx 2 \times 10^{26} \text{ m}^{-3}$ assuming an energy gap $\epsilon_g = 2.3$ eV and a $\gamma = 1.4$ (see [Celliers *et al.*, submitted, 2003; Hicks *et al.*, 2003]). Using a Drude model, we can estimate the electronic contribution (versus ionic) to conductivity, $\sigma_e = (N_e + N_h)e^2\gamma\tau_{\text{min}}/m_e$. The minimum scattering time $\tau_{\text{min}} = \ell/v_e$, and m_e is the effective electron mass (here we use half of the electron mass to take into account the “mass” of the hole). At 5000 K $\sigma_e \approx 25 (\Omega\text{-cm})^{-1}$, at 8000 K $\sigma_e \approx 108 (\Omega\text{-cm})^{-1}$, whereas at 10,000 K, $\sigma_e \approx 189 (\Omega\text{-cm})^{-1}$, comparable to the conductivity measured previously [Chau *et al.*, 2001; Mitchell and Nellis, 1982]. The observed reflectivity can thus be attributed to the production of free electrons (i.e., metal-like behavior).

Discussion

With 5 shots, we are able to observe hot, dense water up to ~ 175 GPa and up to $\sim 10,000$ K. As expected due to the lower temperatures achieved in our pre-compressed samples, at a given pressure, we measure densities that are greater than values measured on the principal Hugoniot [Holmes *et al.*, 1985; Lyzenga *et al.*, 1982; Mitchell and Nellis, 1982; Volkov *et al.*, 1980]. We notice 3 distinct regimes of differing optical properties upon shock compression: transparent, opaque and reflecting (see Table 3-1, Figure 3-2).

At low temperatures ($T < \sim 3700$ K), the shocked water remains transparent with VISAR measuring the moving and reflecting surface of the Al step. With increasing shock pressure, the water turns opaque (optically thick). With further increased pressures, thus increased temperatures, the shocked water becomes reflecting. This has been observed in previous experiments (e.g., [Celliers *et al.*, 2000]) and is interpreted as due to the metallization of the water (production of free electrons) because of the high temperatures reached during shock loading, as predicted by theoretical models [Cavazonni *et al.*, 1999]. We only see reflectivity of the shocked water in the infrared (1064 nm) and not at visible wavelengths for a given shot. At the highest pressures and temperatures (> 150 GPa, 9000 K), water becomes reflecting at 1064 nm (opaque at 532 nm), whereas at lower temperatures (< 9000 K), the water is opaque at 532 nm. We are unable to determine if the shocked water is reflecting in the infrared at temperatures below 9000 K as we did not monitor this wavelength during experiments preceded by “00”.

Figure 3-2 shows the phase diagram of water based on Cavazonni *et al.*'s [1999] calculations and our new measurements. Within the uncertainties of our measurements, our results agree well with the theoretical predictions if we take reflecting water to be metallic in character. Some of our measurements also lie near Neptune's expected isentrope, and suggest that this planet's magnetic field could be generated by pressure-ionized water ($\text{H}_2\text{O} \rightarrow \text{H}^+ + \text{OH}^-$) at pressures as low as ~ 100 GPa, at least an order of magnitude lower in pressure (thus depth) than expected for Neptune's rocky core. Otherwise, if the magnetic field of Neptune is produced by “metallic” water, pressures of ~ 400 GPa, would be required (or temperatures twice as high as that calculated for the isentrope). Our results provide additional evidence that water can sustain a magnetic

dynamo at fairly shallow levels in the planet, compatible with the strongly quadrupolar nature of the observed magnetic field at the surface [*Stone and Miner, 1989*].

References

- Avrorin, E.N., B.K. Vodolaga, L.P. Volkov, A.S. Vladimirov, V.A. Simonenko, and B.T. Chernovoluk, Shock compressibility of lead, quartzite, aluminum, and water at a pressure of ~100 Mbar, *JETP Letters*, 31 (12), 685-687, 1981.
- Barker, L.M., and R.E. Hollenbach, Laser interferometer for measuring high velocities of any reflecting surface, *Journal of Applied Physics*, 43 (11), 4669-4675, 1972.
- Bastea, M., A.C. Mitchell, and W.J. Nellis, High pressure insulator-metal transition in molecular fluid oxygen, *Physical Review Letters*, 86 (14), 3108-3111, 2001.
- Benedetti, L.R., Molecular systems at high pressures and temperatures: Solar system astronomy in a physics laboratory, PhD thesis, University of California, Berkeley, Berkeley, 2001.
- Bessarab, A.V., N.V. Zhidkov, S.B. Korner, D.V. Pavlov, and A.I. Funtikov, Measurement of the reflectivity of metal mirrors acted on by laser radiation, *Sov. J. Quantum Electronics*, 8 (2), 188-191, 1978.
- Cavazonni, C., G.L. Chiarotti, and S. Scandolo, Superionic and metallic states of water and ammonia at giant planet conditions, *Science*, 283 (5398), 44-6, 1999.
- Celliers, P.M., G.W. Collins, and L.B. DaSilva, *Physical Review Letters*, 84, 5564-8, 2000.
- Celliers, P.M., G.W. Collins, L.B. DaSilva, D.M. Gold, and R. Cauble, Accurate measurement of laser-driven shock trajectories with velocity interferometry, *Applied Physical Letters*, 73, 1320-22, 1998.
- Celliers, P.M., G.W. Collins, D.G. Hicks, M. Koenig, E. Henry, A. Benuzzi-Mounaix, D. Batani, D.K. Bradley, R.J. Wallace, S.J. Moon, J.H. Eggert, A. Mackinnon,

- K.K.M. Lee, L.R. Benedetti, R. Jeanloz, I. Masclet, N. Dague, B. Marchet, M. Rabec Le Gloahec, C. Reverdin, J. Pasley, O. Willi, D. Neely, and C. Danson, Equation of state and optical properties of water compressed by strong shock waves, *Physical Review Letters*, submitted, 2003.
- Chau, R., A.C. Mitchell, R.W. Minich, and W.J. Nellis, Electrical conductivity of water compressed dynamically to pressures of 70-180 GPa (0.7-1.8 Mbar), *Journal of Chemical Physics*, 114 (3), 1361-1365, 2001.
- Dewaele, A., J. Eggert, P. Loubeyre, and R. LeToullec, Measurement of refractive index and equation of state in dense He, H₂, H₂O, Ne under high pressure in a diamond-anvil cell, *Physical Review B*, 67, 094112, 2003.
- Goncharov, A.F., and V.V. Struzkhin, Compression of ice to 210 gigapascals: Infrared evidence for a symmetric hydrogen-bonded phases, *Science*, 273 (5272), 218-20, 1996.
- Grigor'ev, F.V., S.B. Kormer, O.L. Mikhailova, M.A. Mochalov, and V.D. Urlin, Shock compression and brightness temperature of a shock wave front in argon. Electron screening of radiation, *Soviet Physics JETP*, 61 (4), 751-757, 1985.
- Hicks, D.G., P.M. Celliers, G.W. Collins, J. Eggert, and S.J. Moon, Shock-induced transformation of Al₂O₃ and LiF into semiconducting liquids, *Physical Review Letters*, 91 (3), 55021-4, 2003.
- Holmes, N.C., W.J. Nellis, and W.B. Graham, Spontaneous Raman scattering from shocked water, *Physical Review Letters*, 55 (22), 2433-36, 1985.
- Hubbard, W.B., *Planetary Interiors*, 334 pp., Van Nostrand Reinhold Company, New York, 1984.

- Hubbard, W.B., Neptune's Deep Chemistry, *Science*, 275, 1279-80, 1997.
- Hubbard, W.B., M. Podolak, and D.J. Stevenson, in *Neptune and Triton*, edited by D.P. Cruikshank, pp. 109-138, University of Arizona Press, Tucson, AZ, 1995.
- Kittel, C., and H. Kroemer, *Thermal Physics*, W. H. Freeman and Co., San Francisco, CA, 1980.
- Kormer, S.B., Optical study of the characteristics of shock-compressed condensed dielectrics, *Soviet Physics Uspekhi*, 11 (2), 229-254, 1968.
- Lee, K.K.M., L.R. Benedetti, A. Mackinnon, D.G. Hicks, S.J. Moon, P. Loubeyre, F. Occelli, A. Dewaele, G.W. Collins, and R. Jeanloz, Taking thin diamonds to their limit: Coupling static-compression and laser-shock techniques to generate dense water, in *Shock Compression Condensed Matter*, American Institute of Physics, Atlanta, GA, 2002.
- Lide, D.R., CRC Handbook of Chemistry and Physics, CRC Press, Boca Raton, FL, 1990.
- Loubeyre, P., P.M. Celliers, D.G. Hicks, E. Henry, A. Dewaele, J. Pasley, J. Eggert, M. Koenig, F. Occelli, K.K.M. Lee, R. Jeanloz, D. Neely, A. Benuzzi-Mounaix, D. Bradley, M. Bastea, S.J. Moon, and G.W. Collins, Coupling static and dynamic compression: First measurements in dense hydrogen, *High Pressure High Temperature*, in press, 2004.
- Lyon, S.P., and J.D. Johnson, Los Alamos National Laboratory Report LA-UR-92-3407, LANL, Los Alamos, NM, 1992.
- Lyzenga, G.A., T.J. Ahrens, W.J. Nellis, and A.C. Mitchell, The temperature of shock-compressed water, *Journal of Chemical Physics*, 76 (12), 6282-6286, 1982.

- Mao, H.K., P.M. Bell, J.W. Shaner, and D.J. Steinberg, Specific volume measurements of Cu, Mo, Pd, and Ag and calibration of the ruby R/_{sub} 1/ fluorescence pressure gauge from 0.06 to 1 Mbar, *Journal of Applied Physics*, 49 (6), 3276-83, 1978.
- Mitchell, A.C., and W.J. Nellis, Equation of state and electrical conductivity of water and ammonia shocked to the 100 GPa (1 Mbar), *Journal of Chemical Physics*, 76 (12), 6273-6281, 1982.
- Podurets, M.A., G.V. Simakov, R.F. Trunin, L.V. Popov, and B.N. Moiseev, Compression of water by strong shock waves, *Soviet Physics JETP*, 35 (2), 375-376, 1972.
- Ree, F.H., Lawrence Livermore National Laboratory Report UCRL-52190, LLNL, Livermore, CA, 1976.
- Saul, A., and W. Wagner, A fundamental equation for water covering the range from the melting line to 1273 K at pressures up to 25000 MPa, *Journal of Physical Chemistry Reference Data*, 18 (4), 1537-1564, 1989.
- Stevenson, D.J., Planetary magnetic fields, *Earth and Planetary Science Letters*, 208, 1-11, 2003.
- Stone, E.C., and E.D. Miner, The Voyager 2 encounter with the Neptunian system, *Science*, 246 (4936), 1417-1421, 1989.
- Takeda, M., H. Ina, and S. Kobayashi, Fourier-transform method of fringe-pattern analysis for computer-based topography and interferometry, *Journal of Optical Society of America*, 72, 156-60, 1982.
- Trunin, R.F., Experimental data on shock compression and adiabatic expansion of condensed matter, pp. 446, RFNC-VNIIEF, Sarov, 2001.

Volkov, L.P., N.P. Voloshin, R.A. Mangasarov, V.A. simonenko, G.V. Sin'ko, and V.L.

Sorokin, Shock compressibility of water at a pressure of ~ 1 Mbar, *JETP Letters*, 31 (9), 513-515, 1980.

Weir, S.T., A.C. Mitchell, and W.J. Nellis, Metallization of fluid molecular hydrogen at

140 GPa (1.4 Mbar), *Physical Review Letters*, 76 (11), 1860-1863, 1996.

Zeldovich, Y.B., and Y.P. Raizer, *Physics of shock waves and high temperature*

phenomena, Academic Press, New York, 1967.

Table 3-1.

Listed below are the initial values of our pre-compressed water samples. Initial pressures, P_0 , are measured by ruby fluorescence [Mao *et al.*, 1978], while initial water densities, ρ_0 , and energies, E_0 , are calculated [Saul and Wagner, 1989]. The shock velocities of Al are measured by VISAR, and particle velocities inferred by the linear U_s - U_p relations. Shock velocity of water is determined by the fringe shift in the short step of the Al (where attenuation is less), while the final pressures and densities are calculated through impedance matching techniques [Zeldovich and Raizer, 1967]. Optical properties are given in the first column; samples which show evidence of reflectivity are only reflecting in the infrared and not in the visible. Shots that are opaque or transparent are only opaque or transparent in the visible. Temperature estimates from pyrometry measurements as well as calculated temperatures from the SESAME database [Lyon and Johnson, 1992], table 7150 [Ree, 1976] are given in the final columns.

Sample	P_0 , GPa	ρ_0 , g/cm ³	E_0 , kJ/ mol	U_s (Al) μm/ns	U_p (Al) μm/ns	U_s (H ₂ O) μm/ns	U_p (H ₂ O) μm/ns	P_f (H ₂ O) GPa	ρ_f (H ₂ O) g/cm ³	T, K Obs., Calc.
4-ns laser-shock pulse, VISAR interferometry at 532 nm only										
001212-13 transparent	0.75 (0.07)	1.199 (0.005)	23.05 (0.02)	10.6 (0.6)	3.86 (0.54)	10.1 (0.3)	5.1	61	2.44	2800, 2700
001213-12 opaque	0.93 (0.13)	1.229 (0.018)	23.16 (0.04)	13.0 (0.5)	5.63 (0.45)	12.9 (0.5)	7.1	115	2.83	4250, 5800
001221-11 opaque	0.74 (0.04)	1.196 (0.006)	23.03 (0.03)	14.1 (0.6)	6.54 (0.50)	14.2 (0.9)	8.5	144	3.00	4300, 8600
1-ns laser-shock pulse, VISAR interferometry at 532 and 1064 nm										
011218-07 reflecting at 1064 nm	1.02 (0.15)	1.242 (0.002)	23.18 (0.13)	15.1 (1.0)	7.43 (0.90)	14.6 (1.0)	9.6	173	3.69	5700, 9800
011220-06 reflecting at 1064 nm, opaque at 532nm	0.40 (0.05)	1.127 (0.001)	22.44 (0.03)	14.8 (0.3)	7.10 (0.30)	14.4 (0.8)	9.4	153	3.25	5300, 10900

Figure 3-1. VISAR streaked image at 1064 nm for sample 011218-07. Al step breakouts are shown for the short (A) and tall (C) steps. Discontinuities shown at B and D are where the fringes disappear, corresponding to the shock wave having traversed the sample and hitting the back diamond. The time duration for the shock record below is ~ 8 ns and the vertical axis is ~ 400 microns. This sample was pre-compressed to the ice VI structure of water. Note that the intensity of light reflected after the short aluminum step (A) is still rather high, although not visible for the tall step (C). This is likely due to the decreased shock strength after going through ~ 10 microns of additional Al. Measured pressure and temperature at A is ~ 173 GPa and 5700 K, where at C, the values are 88 GPa, 3800 K (see Figure 3-2). **Inset.** Percent reflectivity as a function of time. In red (blue), a normalized lineout of the intensity used as a proxy for reflectivity, for the short (tall) step. There is a decaying reflectivity off the short Al step corresponding to $\sim 35\%$ reflectivity down to $\sim 10\%$, compared to $\sim 80\%$ reflectivity for the Al step. The reflectivity falls to zero after points B and D due to the shock wave hitting the back diamond.

Figure 3-2. Pressure versus temperature phase diagram for shocked pre-compressed water compared against a theoretical model [Cavazonni *et al.*, 1999]. Original model is outlined in rectangular box separated into five regions: solid, molecular, superionic, ionic and metallic. For pressures and temperatures outside of their calculations, thin dotted lines show linear extrapolations. Samples that remained transparent at 532 nm (green outlined squares), opaque at 532 (1064) nm (green (red) filled squares) and reflecting at 1064 nm (red hatched squares) are plotted with their measured temperatures. Black

circles above squares indicate the temperatures predicted by the Sesame tables [*Lyon and Johnson, 1992; Ree, 1976*]. Black thick dashed line is Neptune's isentrope [*Hubbard et al., 1995*]. Single-shock (pre-compressed to 1 GPa) Hugoniot of water is plotted as the black (red) curve for reference [*Lyon and Johnson, 1992; Ree, 1976*]. Temperature measurement uncertainties stem from emissivity uncertainties (i.e., wavelength dependence of reflectivity).

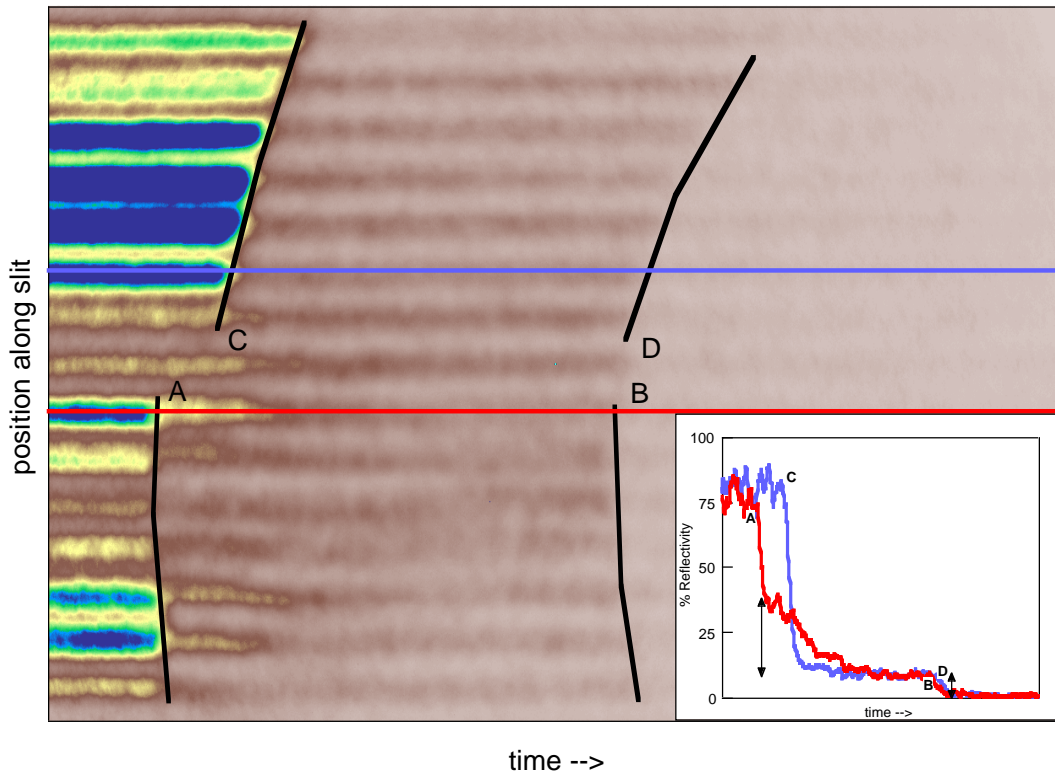


Figure 3-1

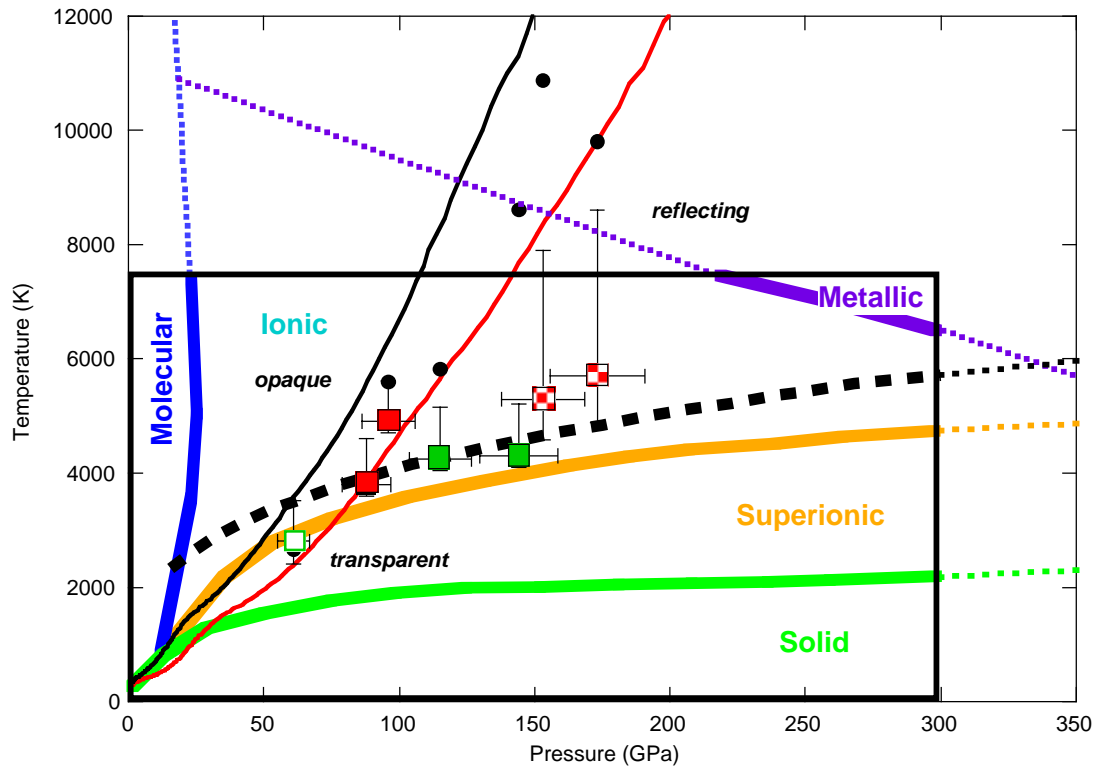


Figure 3-2

Appendix: Technical Aspects

Appendix A: Limits to resolution in composition and density in ultrahigh-pressure experiments on natural mantle-rock samples

Abstract. *To support studies of the Earth's mantle, we compressed and analyzed an undepleted natural peridotite – thought to be representative of the Earth's upper mantle – from ~25-110 GPa and heated to 2000-2500 K. Scatter in zero-pressure unit-cell volumes observed for high-pressure phases synthesized from peridotite, of $\pm 0.4\%$ for orthorhombic perovskite and $\pm 0.8\%$ for magnesiowüstite, can be ascribed to compositional heterogeneity in the natural starting material and its transformation products (calcium perovskite was also observed at high pressures, but does not quench to zero pressure). The scatter is larger than the measurement uncertainties, which are as little as $\pm 0.1\%$, but is less than would be expected from the variation in composition among distinct minerals if the starting material had failed to equilibrate upon transformation to the high-pressure assemblage (e. g., up to $\pm 0.6-0.8\%$ in volume for orthorhombic perovskite). The equilibrium unit-cell volume of orthorhombic perovskite calculated from an average of electron microprobe analyses on the quenched samples, $163.3 (\pm 0.6) \text{ \AA}^3$, agrees to within 0.4% with the average value measured from the same samples by x-ray diffraction at zero pressure ($163.9 \pm 0.7 \text{ \AA}^3$). Similarly, values of zero-pressure density for the whole-rock assemblage of high-pressure phases are identical ($4.13 \pm 0.03 \text{ g/cm}^3$), whether derived from electron microprobe or x-ray diffraction measurements.*

Introduction

There is a great need for experiments that reproduce the conditions of high pressures and temperatures existing deep inside planets. In particular, it is important to characterize the properties of relevant materials at deep-interior conditions in order to determine the constitution, state and evolution of the Earth and planets over geological time. Thus, it is only through high pressure–temperature studies that seismological and other geophysical observations can be interpreted in terms of the identities (*e. g.*, crystal structures), abundances, compositions and other properties of the mineral phases of the Earth’s deep interior. It is therefore important to quantify the reliability and resolution of the measurements obtained from high-pressure experiments so that one can determine the significance of models derived from the combined measurements and geophysical observations.

The quality of such experiments is often described in terms of i) the range and calibration of the pressures and temperatures that are achieved, and ii) the quality of the measurements performed at high pressures. With the advent of the laser-heated diamond cell, it is now possible to reproduce essentially the full range of pressures and temperatures existing inside the Earth, and calibration of experimental conditions has received considerable attention to date (Jeanloz and Kavner, 1996; Knittle and Jeanloz, 1987; Mao et al., 1978; Shim et al., 2002). Similarly, the use of synchrotron- and laser-based probes, among other tools, has led to major advances in the quality of measurements that can be performed on samples at high pressures.

The role of the starting material has received relatively little attention, however, as a third source of uncertainty affecting the quality of high-pressure measurements.

Indeed, the sample material is often chosen so as to minimize any possible degradation of the measurements. It is for this reason that most ultrahigh-pressure (~ 100 GPa) studies to date have focused on the properties of single-phase and, in many cases, synthetic starting materials (*e. g.*, (Andrault, 2001; Fiquet et al., 1998; Knittle and Jeanloz, 1987). As the ultimate objective is to determine the properties of planetary materials at deep-interior conditions, however, it also becomes necessary to examine natural samples. This is so if for no other reason than to evaluate the effects of minor elements or the presence of minor (initial) phases on the final results. In addition, certain materials are intrinsically difficult to synthesize as truly homogeneous samples, with the most ideally uniform starting material being amorphous.

Ultramafic rocks, characteristic of the Earth's upper mantle and of chondritic meteorites, offer a good example of such difficulties. Bulk compositions corresponding to peridotite and similar rocks are refractory, and cannot be readily quenched to a glass from the melt. Even if a glass is formed on cooling (*e. g.*, by splat quenching), melting temperatures are sufficiently high that moderately volatile elements such as Na and K are often lost during preparation of the starting sample. Sol-gel techniques can produce an amorphous and relatively uniform starting material of peridotite composition, but invariably lead to contamination, especially by hydrogen. Finally, mechanical comminution (*e. g.*, by ball milling) can produce a uniform, fine-grained and possibly amorphous sample, but with the potential of contamination from the grinding surfaces.

Consequently, it is difficult to obtain pure (uncontaminated) and uniform starting materials having the bulk composition of terrestrial mantles. Sample uniformity is especially critical for the highest-pressure experiments: these rely on small ($\sim \mu\text{g}$) samples

being compressed inside a diamond-anvil cell, in contrast with the larger (~mg) samples that are compressed (but to lower peak pressures) in multi-anvil devices. For the latter, electron microprobe and other high-quality analytical tools can be used to confirm that individual mineral grains formed at high pressures have uniform and reproducible compositions. In comparison, it is much more difficult to document homogeneity – and therefore a close approach to equilibrium – for individual mineral phases produced in the laser-heated diamond cell.

The objective of the present work is to quantify the resolution in molar volume, composition and density of the high-pressure mineral-phase assemblage formed from a natural sample that is thought to have a bulk composition close to that of the Earth's mantle. In combination with seismological observations, these properties are important for modeling the constitution and state of the deep interior. Our focus here is on zero-pressure measurements, as these can reveal much about the reliability of the data: for example, beginning to quantify the degree to which the sample achieves (at least local) thermodynamic equilibrium, as well as the accuracy of such relevant properties as phase-composition and assemblage-density.

Lower-Mantle Assemblage formed from Natural Peridotite

We address these issues, including the role of the initial sample in producing equilibrated high-pressure phases, by describing the high-pressure assemblage formed from a natural peridotite at lower-mantle pressures (~25-110 GPa). This is but one example of the rock-types present in the Earth's mantle, but is of special interest because it is thought to correspond to the bulk composition of at least the upper mantle (*e. g.*,

(Ringwood, 1975). The starting material (BN-35), with bulk composition and mineral constituents given in Table A-1 (Stern et al., 1986), was transformed in two sets of experiments using laser-heated diamond cells (diamond culet size ranging from 100-350 μm) using pre-compressed (to $\sim 20\text{-}40$ μm thick) Re or Fe gaskets. In all cases, pressures were determined before and after laser heating using the ruby-fluorescence scale (Mao et al., 1978), with only the values after heating being quoted here. In both sets of experiments, the sample was laser heated by rastering it under the focused beam (hot-spot diameter ~ 20 μm) of a continuous (cw) TEM₀₀-mode Nd-YAG ($\lambda = 1064$ nm) laser, keeping clear of the very edges of the gasket and ruby calibrant to minimize the possibility of contamination. Heating duration at any one spot was short (seconds) at any particular time, in order to minimize the Soret diffusion of Fe out of the hot spot, with total heating of the entire sample taking approximately 10 - 30 minutes (both for synthesis and annealing). The laser power was kept sufficiently low to avoid melting, and we observed no evidence of melting either during heating or through analysis of the sample after heating.

Of the two sets of experiments, each run in the first set consisted of compressing a fresh sample of peridotite to a given pressure, laser-heating the sample to temperatures of 2000-2500 K, and then obtaining x-ray diffraction patterns at room temperature before and after decompressing the sample to zero pressure (O'Neill, 1994; O'Neill and Jeanloz, 1990). All of these diffraction patterns were collected at room temperature, using monochromatic Mo K α ($\lambda = 0.7107$ Å) radiation from a rotating-anode source at high pressures and filtered Cu K α ($\lambda = 1.5418$ Å) radiation from a standard tube at zero pressure (after the sample was removed from the diamond cell). In both cases, the beam

size was comparable to the diameter of the sample, $\sim 100\text{-}150\ \mu\text{m}$. The diffraction patterns were collected on film that was digitized and analyzed as described elsewhere (Nguyen and Jeanloz, 1993), and with fitting of individual peaks to determine constituent phase unit-cell volumes (O'Neill, 1994).

In the second set of experiments, the sample was loaded in an Ar medium and laser heated to 2000-2500 K at pressures of 30-52 GPa in order to convert the peridotite to the high-pressure assemblage. X-ray diffraction patterns were then collected at several pressures, on compression to peak pressures of 47-87 GPa and decompression to zero pressure (sample outside the diamond cell), with laser-heating used to further anneal the samples at 41, 47, 66, 78 and 87 GPa. All of the diffraction patterns for the second set of experiments were collected at room temperature using synchrotron radiation and image plates, with the size of the x-ray beam ranging from $60\ \mu\text{m}$ (*i. e.*, much smaller than the sample) for the high-pressure runs to more than $100\ \mu\text{m}$ diameter upon quench (Figure A-1A, B). Data were collected at Stanford Synchrotron Radiation Laboratory (SSRL) beamline 10-2 and Advanced Photon Source (APS) beamline 13-IDB, and were analyzed both through individual fitting of peaks (as in the first set of experiments) and by Rietveld analysis (Larson and Von Dreele, 2000; Toby, 2001) (Figure A-1B).

In both sets of experiments, the samples transformed to assemblages of $64 (\pm 2)$ mol% (Mg, Fe, Al)SiO₃ orthorhombic perovskite (opv), $31 (\pm 2)$ mol% (Mg, Fe)O magnesiowüstite (mw) and $5 (\pm 1)$ mol% CaSiO₃ perovskite (cpv), where the relative proportions were determined from the bulk composition of the starting material (see Table A-1) and the compositions of the high-pressure mineral phases deduced from the lattice parameters obtained from the x-ray patterns (Jeanloz and Thompson, 1983;

O'Neill, 1994; O'Neill and Jeanloz, 1990). These results are compatible with the mineral-phase proportions obtained in the Rietveld fits, so can be considered independently verified.

Complete and essentially smooth powder-diffraction lines were obtained, with some amount of spottiness (from grain growth upon transformation) observed in patterns taken with higher spatial resolution (Figure A-1A). The character of the diffraction rings is in line with observations by optical microscopy, which indicate the presence of occasional crystals as large as 2-5 μm but the bulk of the transformed sample having crystal sizes under 1-2 μm . The important point is that the individual crystals were much smaller than the laser-heated spot, both before and after transformation.

Overall, the quality of the diffraction patterns indicates good conversion to the high-pressure assemblage. Except for minor amounts of garnet remaining after heating at pressures below 30-35 GPa, none of the starting material was evident in the diffraction patterns from the heated portions of each sample. Of course, starting material was present in the unheated portions of the samples (*e. g.*, next to the gasket), as we were able to distinguish by comparing diffraction patterns obtained using a small-diameter x-ray beam taken at high pressures with large-diameter beam patterns taken at zero pressure (Figure A-1). The presence of garnet in the heated portions of the lowest-pressure runs is consistent with phase equilibria determined in independent studies and with other methods, so does not indicate an inability to transform the entire sample or any other indication of deviation from phase-equilibrium. Because of the small amount of calcium perovskite present in the high-pressure assemblage, and the fact that it becomes amorphous (so has no diffraction lines) on quenching to zero pressure, we limit our

present discussion of the diffraction patterns to results for orthorhombic perovskite and magnesiowüstite.

The quality of data obtained from the natural peridotite starting material is quantified in Figure A-2, which shows the scatter in unit-cell volumes for orthorhombic perovskite and magnesiowüstite being about $\pm 1\%$ at high pressures and $\pm 0.4\text{-}0.8\%$ upon quenching to zero pressure (average values, indicated by shading in the figure, are quoted here). Uncertainties in the volumes (individual error bars) range from less than $\pm 0.1\%$ to as much as $\pm 1.0\text{-}2.5\%$, and are generally much less than the scatter.

Both the uncertainties and scatter are larger by $\sim 25\text{-}65\%$ at high pressures than upon quenching. This is partly due to some of the high-pressure patterns being of lower quality than the zero-pressure data, mainly because of the effects of diamond absorption (because the zero-pressure patterns were obtained from samples outside the diamond cell). Additionally, overlapping diffraction lines and uncertainties in the sample pressure also contribute to the increased scatter between observed and calculated volumes at high pressures. In particular, measured variations in pressure across a sample were as small as 0.2 GPa and as large as 12.6 GPa, which corresponds to volume uncertainties of $\pm 0.2\text{-}5.0\%$ (calculated using a Birch-Murnaghan equation of state (Birch, 1978)). Nonhydrostaticity may further degrade some of the high-pressure measurements, although we have found no correlation between the measured pressure variations across samples (or the presence or absence of an Ar medium) and the observed scatter.

Following Andraut (2001), we look at the volume ratio between opv and mw, V_{opv}/V_{mw} (Figure A-3). At zero pressure we find an average $V_{0,opv}/V_{0,mw}$ of 2.16 (± 0.02) without any noticeable dependence on synthesis pressure, and the results in Figure A-3

(bottom) are merely another representation of the data shown in Figure A-2 (bottom). Following early partitioning experiments (Bell et al., 1979; Yagi et al., 1979), this would suggest that the Mg/Fe distribution coefficient between opv and mw does not depend on pressure, and is otherwise not affected by synthesis conditions over the range covered in the present study.

At high pressure, V_{opv}/V_{mw} is not constant due to the differences in the compressibilities of opv and mw. As Andraut points out (Andraut, 2001), any deviations from the predicted Mg-endmember volume ratio (dashed curve and dark shading in Figure A-3, top) may be attributable to a change in partitioning behavior with pressure. His analysis, however, does not include any effects of Al nor the uncertainties in the respective equations of state. When we do take these factors into account, we find that within the uncertainties of the known equations of state (solid curve and light shading in Figure A-3, top (Lee et al., 2003)) we cannot confirm any changes of partitioning with pressure. For the Mg-endmembers, we use the Birch-Murnaghan equation of state with the following values for the parameters V_0 , K_{0T} and K'_{0T} : MgSiO₃ 162.47 (\pm 0.31) Å³, 263 (\pm 3) GPa, 3.9 (\pm 0.5); MgO 74.7243 (\pm 0.0537) Å³, 162.7 (\pm 2.9) GPa, 4.1 (\pm 0.1) (Andraut, 2001; Jeanloz and Hemley, 1994; Jeanloz and Thompson, 1983).

The high-pressure measurements are therefore compatible with what we infer from the zero-pressure volumes (Figure A-2, bottom) or volume ratios (Figure A-3, bottom), namely that there is no evidence for a shift in Mg/Fe partitioning between opv and mw between 25 and 110 GPa. This is in contrast with inferences recently derived from high-pressure x-ray spectroscopy on mw (Badro et al., 2003), perhaps because we

are studying a more complex (*i. e.*, natural, Al-bearing) bulk composition in the present experiment. The remaining scatter, of $\pm 0.4\%$ and $\pm 0.8\%$ observed for the volumes of opv and mw at zero pressure, can be ascribed to compositional variations in the high-pressure mineral phases.

Overall, as much as 1/2-2/3 of the uncertainty in the opv and mw volumes measured at high pressures is of the same magnitude as – so can be ascribed to the same factors causing – the scatter in volumes observed at zero pressure (Figures A-2 and A-3). If there is a systematic correlation between volume deviations for a given sample at high pressures and at zero pressure, however (*e. g.*, Figure A-2 top and bottom), any such correlation is obscured by the added uncertainties in the high-pressure measurements. Consequently, we now focus on the scatter in opv and mw unit-cell volumes measured at zero pressure, and note that it exhibits no correlation with synthesis pressure (Figures A-2, A-3).

Electron Microprobe Analyses

In order to determine whether or not the observed scatter in unit-cell volumes is due to variations in composition, we have performed electron microprobe analyses on several of the quenched samples. The conditions of synthesis, high pressures and temperatures achieved between smooth diamond culet faces, ensure that the transformed peridotite often has a smooth surface suitable for microprobe analysis (Figure A-4). Samples still encased in their gaskets were mounted on glass slides, cleaned and carbon coated. A Cameca SX-51 electron microprobe was used with a 15 keV electron beam

focused to a spot size $\leq 5 \mu\text{m}$ diameter at the sample, and pure metal oxides served as standards (Pingitore et al., 1999).

Abundances were determined for Si, Ti, Al, Fe, Mg, Ca, Na and K. Because oxygen was not included in the analyses, the data were reduced assuming stoichiometric compositions. Earlier analyses (Knittle and Jeanloz, 1991), which did include oxygen, provide support for orthorhombic perovskite having stoichiometric composition when formed in the laser-heated diamond cell at comparable pressures and temperatures. However, we note that there is considerable interest in the possibilities of nonstoichiometry and of point defects in opv; this is especially so for more complex (*e. g.*, Al-bearing) compositions, such as may be relevant to the present study (*e. g.*, (Navrotsky et al., 2002). Low totals were obtained in some analyses, however these can all be attributed to poor surface conditions or sample orientation in the present experiments. Only those analyses with totals between 98.0% and 102.0% are discussed here (almost all the rejected analyses came from one sample with a poor surface).

Although typical sample dimensions exceed $100 \mu\text{m}$ in diameter (Figure A-4), an average of only nine analyses is already in good agreement (within mutual uncertainties) with the bulk composition of the rock, except for a deficiency in CaO (Table A-2). Because of the fine (mostly sub- μm) grain size of the transformed sample, each analysis is an average over a mixture of the three high-pressure phases, opv, mw and cpv. Indeed, it is impossible to interpret the analyses as being an average over fewer than 2-3 of the high-pressure mineral phases (*e. g.*, an Mg/Si ratio exceeding 1 may be inferred for opv). Four individual analyses illustrating the range of observed compositions are listed in

Table A-2, and confirm that there can be quite a bit of variability from one spot to another within a sample, as well as from sample to sample.

Interpreting the scatter in individual analyses as being due to varying amounts of opv, mw, cpv and ruby (contamination from the pressure calibrant), we are able to estimate the composition of opv (and relative abundances of each phase) based on 2 assumptions. First, we assume that $x_{Fe} = 0.20$ for mw, based on the lattice-parameter determined by x-ray diffraction (Jeanloz and Thompson, 1983). Second, we assume that cpv is pure CaSiO_3 , based on the high-pressure volumes being compatible with those previously measured for pure cpv (O'Neill, 1994). Also, there is so little cpv in the high-pressure assemblage that even if the maximum amount of Al that has been observed to enter the structure is assigned to this phase (Takafuji et al., 2002), our conclusions are unaffected within quoted uncertainties. We then calculate the unit-cell volumes for the inferred composition of opv, taking into account aluminum as well as iron substitution (O'Neill and Jeanloz, 1994).

Our calculated opv zero-pressure volumes for the average of 9 analyses ($V_0 = 163.3 \pm 0.6 \text{ \AA}^3$) are in excellent agreement with the observed average opv volume ($V_0 = 163.9 \pm 0.7 \text{ \AA}^3$) for those same samples (Table A-3). The opv volumes inferred from the individual microprobe analyses generally overlap the values observed for the same samples (*e. g.*, Per_500), but not always (Per_601). The difference of up to 0.7% among individual calculated volumes is larger than the estimated uncertainties ($\pm 0.1\text{-}0.2\%$), but the average of calculated volumes is still within the uncertainty for the volumes observed by x-ray diffraction ($\pm 0.4\%$). A similar conclusion is reached for the calculated densities

of opv, which exhibit differences as large as 4.4% for the individual analyses but an uncertainty less than $\pm 1.5\%$ for the average (Table A-3).

These results confirm that the observed scatter in x-ray diffraction measurements at zero pressure can be completely explained in terms of compositional heterogeneity in the high-pressure assemblage formed from a natural rock sample. Indeed, the x-ray data represent more nearly the average composition of the sample, in comparison with the individual electron microprobe analyses that reflect more of the local heterogeneity within each sample. This is not surprising, given the different sampling volumes characterizing the two methods in the present study: $\sim 5\mu\text{m}$ and $\sim 60\mu\text{m}$ diameter for the microprobe and diffraction analyses, respectively.

Discussion and Conclusions

In order to quantify the range of compositional heterogeneity that might be expected in our samples, we consider the possibility that the individual minerals of the starting material each transforms to the high-pressure phases but without equilibrating amongst each other. Based on the composition and mode of BN-35 (Table A-1), we find that the fractional molar abundances of iron and aluminum in the orthorhombic perovskite can vary over the range $x_{Fe} = 0.10\text{-}0.20$ and $x_{Al} (= \text{Al} / (\text{Al} + \text{Mg})) = 0.06\text{-}0.48$ (Table A-4). Similarly, the molar abundance of iron in magnesiowüstite is in the range $x_{Fe} = 0.00\text{-}0.10$ (mw is derived only from the initial olivine, in this instance).

This calculated variability in composition is larger than we observe, as is the corresponding scatter in calculated zero-pressure volumes: *e. g.*, up to 1.2-1.6% expected volume differences (*i. e.*, up to $\pm 0.6\text{-}0.8\%$ scatter) for opv (see Table A-4), as compared

with $\pm 0.4\%$ observed (Figure A-2, bottom). Therefore, we conclude that whereas compositional variation across the entire sample is reflected in the observed variability in zero-pressure volumes (and electron microprobe analyses), there is at least an approach to equilibration between the high-pressure mineral phases formed from the distinct minerals in the starting material. That is, equilibrium is sufficiently well achieved to yield a reproducible assemblage of phases having relatively well-defined compositions and unit-cell volumes.

The variability in bulk starting composition (Table A-1) can explain the scatter in the observed properties of the quenched samples (Figures A-2 and A-3). The resulting uncertainty in properties at zero pressure is then generally convolved with additional uncertainties for *in-situ* measurements at high pressures. In the present case, the average observed uncertainty in unit-cell volumes is roughly 50% greater at high pressures than at zero pressure.

Nevertheless, covariation among the properties of the individual mineral phases can lead to relatively well-constrained properties for the whole-rock assemblage. For example, the whole-rock, zero-pressure densities calculated from analyses 911 and 919 of Tables A-2 and A-3 are 4.11 g/cm^3 and 4.15 g/cm^3 , respectively, a difference of only 1% (as opposed to the nearly 5% difference in opv densities given in Table A-3). For comparison, the whole-rock density calculated for the average of 9 microprobe analyses is $4.13 (\pm 0.03) \text{ g/cm}^3$, and is identical to the density determined entirely from the x-ray diffraction measurements ($4.13 \pm 0.02 \text{ g/cm}^3$).

The reason for this good agreement is that the bulk composition of the rock already determines the mean atomic weight of the sample, so that the density is really

determined to within the resolution of the average volumes of the mineral phases. Thus, the zero-pressure density of the assemblage can be obtained by two methods, purely from the x-ray diffraction data (calculated phase compositions and abundances) or purely from the electron microprobe analyses (calculated phase volumes and compositions), and the results agree to well within the $\pm 0.5\%$ uncertainty of either approach. This agreement is important for geophysical applications because it means that the results of high-pressure experiments can be used to quantitatively interpret seismologically observed values of density for the Earth's deep mantle.

References

- Andrault, D., 2001. Evaluation of (Mg,Fe) partitioning between silicate perovskite and magnesiowüstite up to 120 GPa and 2300 K. *Journal of Geophysical Research*, 106(B2): 2079-87.
- Badro, J. et al., 2003. Iron Partitioning in Earth's Mantle: Toward a Deep Lower Mantle Discontinuity. *Science*, 300(5620): 789-791.
- Bell, P.M., Yagi, T. and Mao, H.K., 1979. Iron-Magnesium distribution coefficients between spinel [(Mg, Fe)₂SiO₄], Magnesiowüstite [(Mg, Fe)O], and Perovskite [(Mg, Fe)SiO₃]. *Carnegie Institution of Washington Year Book*, 78(1790): 618-621.
- Birch, F., 1978. Finite strain isotherm and velocities for single-crystal and polycrystalline NaCl at high pressures and 300 K. *Journal of Geophysical Research*, 83: 1258-1267.
- Fiquet, G. et al., 1998. P-V-T equation of state of MgSiO₃ perovskite. *Physics of the Earth and Planetary Interiors*, 105(1-2): 21-31.
- Jeanloz, R. and Hemley, R.J., 1994. Thermoelasticity of Perovskite: An Emerging Consensus. *EOS, Transactions, American Geophysical Union*, 75(41): 476-477.
- Jeanloz, R. and Kavner, A., 1996. Melting criteria and imaging spectroradiometry in laser-heated diamond-cell experiments. *Philosophical Transactions of the Royal Society of London A (Mathematical and Physical Sciences)*, 354: 1279-1305.
- Jeanloz, R. and Thompson, A.B., 1983. Phase transitions and mantle discontinuities. *Reviews of Geophysics and Space Physics*, 21(1): 51-74.

- Knittle, E. and Jeanloz, R., 1987. Synthesis and equation of state of (Mg,Fe)SiO₃ perovskite to over 100 gigapascals. *Science*, 235(4789): 668-70.
- Knittle, E. and Jeanloz, R., 1991. Earth's Core-Mantle Boundary: Results of Experiments at High Pressures and Temperatures. *Science*, 251(5000): 1438-1443.
- Lang, A.R., 1998. From Borrmann to Super-Borrmann Effect: from 2-Beam to n-Beam Diffraction. *Cryst. Res. Technol.*, 33(4): 613-623.
- Larson, A.C. and Von Dreele, R.B., 2000. Los Alamos National Laboratory Report No. LAUR 86-748, LANL.
- Lee, K.K.M. et al., 2003. Equations of state of high-pressure phases of a natural peridotite: Implications for the Earth's lower mantle. In preparation.
- Mao, H.K., Bell, P.M., Shaner, J.W. and Steinberg, D.J., 1978. Specific volume measurements of Cu, Mo, Pd, and Ag and calibration of the ruby R1 fluorescence pressure gauge from 0.06 to 1 Mbar. *Journal of Applied Physics*, 49(6): 3276-83.
- Navrotsky, A. et al., 2002. Aluminum in Magnesian Silicate Perovskite: Synthesis and Energetics of Defect Solid Solutions. In: K. Poeppellmeier, A. Navrotsky and R.M. Wentzcovitch (Editors), *Materials Research Society Symposium. Perovskite Materials*. Materials Research Society, Warrendale, PA, pp. 103-108.
- Nguyen, J.H. and Jeanloz, R., 1993. A computer program to analyze x-ray diffraction films. *Review of Scientific Instruments*, 64: 3456-3461.
- O'Neill, B., 1994. *Experimental Petrology of the Lower Mantle*. PhD Thesis, University of California, Berkeley, Berkeley, 135 pp.
- O'Neill, B. and Jeanloz, R., 1990. Experimental petrology of the lower mantle: A natural peridotite taken to 54 GPa. *Geophysical Research Letters*, 17(10): 1477-80.

- O'Neill, B. and Jeanloz, R., 1994. MgSiO₃-FeSiO₃-Al₂O₃ in the Earth's lower mantle: Perovskite and garnet at 1200 km depth. *Journal of Geophysical Research*, 99(B10): 19,901-19,915.
- Pingitore, N.E., Jr., Donovan, J.J. and Jeanloz, R., 1999. Electron microprobe quantification: A new model based on electrons rather than on mass. *Journal of Applied Physics*, 86(5): 2790-2794.
- Ringwood, A.E., 1975. *Composition and Petrology of the Earth's Mantle*. McGraw-Hill, New York, 618 pp.
- Shim, S.H., Duffy, T.S. and Takemura, K., 2002. Equation of state of gold and its application to the phase boundaries near 660-km depth in the Earth's Mantle. *Earth and Planetary Science Letters*, 203(2): 729-739.
- Stern, C.R., Saul, S.L., Skewes, M.A. and Futa, K., 1986. Garnet peridotite xenoliths from the Pali-Aike alkali basalts of southernmost South America. In: J. Ross (Editor), *Fourth International Kimberlite Conference. Kimberlites and Related Rocks*. Blackwell Scientific, Perth, Australia, pp. 735-744.
- Takafuji, N., Yagi, T., Miyajima, N. and Sumita, T., 2002. Study on Al₂O₃ content and phase stability of aluminous-CaSiO₃ perovskite at high pressure and temperature. *Phys Chem Minerals*, 29: 532-537.
- Toby, B.H., 2001. EXPGUI, a graphical user interface for GSAS. *Journal of Applied Crystallography*, 34: 210-13.
- Yagi, T., Mao, H.K. and Bell, P.M., 1979. Lattice Parameters and Specific Volume for the Perovskite phase of orthopyroxene composition, (Mg, Fe)SiO₃. *Carnegie Institution of Washington Year Book*, 78(1790): 612-613.

Table A-1. Composition of BN-35 and its individual phases in wt% (Stern et al., 1986)

	BN-35	Olivine	Orthopyroxene	Clinopyroxene	Garnet
	Whole-Rock Composition*	45 vol% 43 mol%	25 vol% 33 mol%	15 vol% 19 mol%	15 vol% 5 mol%
SiO ₂	45.40 (0.26)	34.08	56.89	53.31	43.94
TiO ₂	0.25 (0.06)	0.29	0.10	0.45	0.16
Al ₂ O ₃	4.30 (0.69)	4.02	3.49	5.73	23.19
Cr ₂ O ₃	0.30 (0.02)	0	0.35	0.83	1.16
FeO ^Δ	8.30 (0.53)	10.97	7.63	3.13	8.06
MnO	0.14 (0.01)	0.24	0.08	0.04	0.24
MgO	37.10 (0.93)	52.57	30.99	15.43	19.88
CaO	3.30 (0.13)	0	0.76	20.11	4.97
Na ₂ O	0.30 (0.03)	0.19	-	1.37	-
K ₂ O	0.0 (-)	-	-	-	-
NiO	0.24 (-)	-	-	-	-
Total	99.63	102.36	100.29	100.4	101.6
$x_{Fe} =$ Fe/(Fe+Mg)	0.11 (0.02)	0.10	0.12	0.10	0.19
Mg# = Mg/(Mg+Fe)	0.89 (0.02)	0.90	0.88	0.90	0.81

* Uncertainties are given in parentheses and are determined by taking the difference in element abundances from an independent measurement of the starting sample (O'Neill, 1994).

^Δ Fe²⁺ and Fe³⁺ totals are combined.

Table A-2. Electron microprobe analyses of quenched samples in wt%

Sample Analysis	Per_500		Per_601		Average (9 Analyses)
	<u>882</u>	<u>898</u>	<u>911</u>	<u>919</u>	
SiO ₂	52.34	51.53	44.42	39.98	45.89 (6.32)
TiO ₂	0.17	0.12	0.14	0.00	0.08 (0.07)
Al ₂ O ₃	3.87	7.56	1.62	0.20	2.96 (2.94)
FeO	6.47	5.90	9.41	10.19	8.20 (1.96)
MgO	36.32	32.08	43.19	48.86	41.74 (7.57)
CaO	0.74	0.93	1.23	0.14	0.66 (0.37)
Na ₂ O	0.17	0.13	0.15	0.02	0.11 (0.06)
K ₂ O	0.02	0.02	0.04	0.01	0.01 (0.01)
Sum	100.10	98.26	100.18	99.39	99.65 (0.81)

Table A-3. Orthorhombic perovskite compositions inferred from electron microprobe analyses (per 3 O)*

Sample Analysis	Per_500		Per_601		Average (9 Analyses)
	<u>882</u>	<u>898</u>	<u>911</u>	<u>919</u>	
Mg	0.88 ±0.03	0.87 ±0.02	0.88 ±0.07	1.00 ±0.03	0.93 ±0.08
Fe	0.07 ±0.01	0.09 ±0	0.17 ±0.02	0 ±0.02	0.06 ±0.06
Al	0.08 ±0.01	0.12 ±0.04	0.04 ±0	0.01 ±0	0.06 ±0.05
Si	0.97 ±0.03	0.92 ±0.02	0.91 ±0.09	0.99 ±0.01	0.95 ±0.05
Calculated opv V_0 (Å³)	163.43 ±0.17	163.76 ±0.21	163.80 ±0.23	162.64 ±0.17	163.26 ±0.62
Observed opv V_0 (Å³)	164.37 ±0.19		164.17 ±0.32		163.90 ±0.67
Calculated opv ρ_0 (g/cm³)	4.17 ±0.02	4.19 ±0.02	4.29 ±0.02	4.10 ±0.04	4.16 ±0.06

* Assumes that the magnesiowüstite is of composition (Mg_{0.80}Fe_{0.20})O; all of the Ca is in a pure CaSiO₃; and that there might be a finite amount of ruby contamination. Using the volume relation of orthorhombic perovskite with Fe and Al, we calculate the zero-pressure unit-cell volume (V_0) and density (ρ_0) based on the composition determined by electron microprobe analysis (O'Neill and Jeanloz, 1994). Values indicated as “0” mean less than 0.5%.

Table A-4. Decomposition reactions of initial minerals to lower-mantle phases^Δ

Reaction	Starting composition[†]	Orthorhombic perovskite composition	Magnesiowüstite or calcium perovskite composition
olivine → orthorhombic perovskite + magnesiowüstite	(Mg _{1.90} , Fe _{0.22} , Al _{0.06} , Si _{0.82})O ₄	(Mg _{1.00-0.90} , Fe _{0.12-0.22} , Al _{0.06} , Si _{0.82})O ₃	(Mg _{0.90-1.00} , Fe _{0.10-0.00})O
Calculated V_0 (Å ³) ^{^,*}		163.61-164.20	75.39-74.72
orthopyroxene → orthorhombic perovskite + calcium perovskite	(Mg _{0.81} , Fe _{0.11} , Al _{0.07} , Ca _{0.01}) SiO ₃	(Mg _{0.82} , Fe _{0.11} , Al _{0.07}) SiO ₃	CaSiO ₃
Calculated V_0 (Å ³) [^]		163.61	
clinopyroxene → orthorhombic perovskite + calcium perovskite	(Ca _{0.40} , Mg _{0.43} , Fe _{0.05} , Al _{0.13} , Si _{0.99})O ₃	(Mg _{0.72} , Fe _{0.08} , Al _{0.22} , Si _{0.98})O ₃	CaSiO ₃
Calculated V_0 (Å ³) [^]		164.24	
garnet → orthorhombic perovskite + calcium perovskite	(Mg _{2.10} , Fe _{0.48} , Ca _{0.37} , Al _{1.94} , Si _{3.11})O ₁₂	(Mg _{0.58} , Fe _{0.13} , Al _{0.53} , Si _{0.76})O ₃	CaSiO ₃
Calculated V_0 (Å ³) [^]		166.19	

^Δ Based on a mass balance, allowing some defects or nonstoichiometry (corresponding to up to -6.3 to +2.0% deviation from charge balance).

[†] Whole rock and individual phase compositions from Table A-1 (Stern et al., 1986).

[^] V_0 calculated for orthorhombic perovskite from (O'Neill and Jeanloz, 1994).

^{*} V_0 calculated for magnesiowüstite from (Jeanloz and Thompson, 1983).

Figure A-1. (A) X-ray diffraction patterns of sample Per_500 at a pressure of 51.8 (\pm 0.5) GPa (*Top*) and at zero pressure (*Bottom*), taken after laser heating and conversion to the high-pressure mineral assemblage. The main diffraction lines of the high-pressure phases are labeled: orthorhombic perovskite (opv), magnesiowüstite (mw) and calcium perovskite (cpv). The data were collected at room temperature at SSRL, using monochromatic radiation ($\lambda = 0.7277 \text{ \AA}$) and image plates. The high-pressure diffraction pattern was obtained using a 60 μm diameter x-ray beam, and the zero-pressure pattern was obtained using a 150 μm diameter beam. Only half the diffraction pattern is shown in each case, and the cross-cutting diagonal lines in the upper pattern are ascribed to Kossel fringes (Lang, 1998) from the diamond anvil (the pattern at zero pressure is of only the sample, without the diamonds). **(B)** Rietveld refined x-ray diffraction patterns at 51.8 (\pm 0.5) GPa (*Top*) and quenched (*Bottom*) shown in **A**. Dots are the actual data while the line is the calculated Rietveld fit. Phase diffraction-line positions shown as ticks below each pattern, in descending order: orthorhombic perovskite, magnesiowüstite, and calcium perovskite (or garnet (gt) in quenched pattern). Garnet is seen only in the quenched patterns (and only at the \sim 0.1 wt% level) as the x-ray beam probes a larger portion of the sample, including the edges that were not heated and are thus unconverted.

Figure A-2. Percent deviation in unit-cell volumes (V) for orthorhombic perovskite (*circles*) and magnesiowüstite (*squares*), shown as a function of pressure at high pressure (*Top*) and as a function of synthesis pressure at zero pressure (*Bottom*). Open and closed symbols designate samples loaded with and without an Ar pressure medium, respectively, and error bars indicate measurement uncertainties when these exceed the size of the

symbol. Deviations are calculated from our measured equations of state at high pressures (to be discussed elsewhere; see also O'Neill (1994)), and from weighted-mean values of $163.90 (\pm 0.67) \text{ \AA}^3$ for opv and $76.09 (\pm 0.60) \text{ \AA}^3$ for mw at zero pressure. Standard deviations reflecting the observed scatter are shown by dark shading for orthorhombic perovskite and light shading for magnesiowüstite.

Figure A-3. Volume ratio of orthorhombic perovskite to magnesiowüstite V_{opv}/V_{mw} as a function of pressure at high pressure (*Top*) and as a function of synthesis pressure at zero pressure (*Bottom*). **Top.** *Circles* are our data, with argon as a pressure medium (*open circles*) and without argon (*closed circles*). To compare we also plot data from Table A-2 from Andraut's (2001) high-pressure study of San Carlos olivine (*open triangles*), alumina + San Carlos olivine (*closed triangles*) and a San Carlos olivine equilibrated at oxygen fugacity fO_2 of 8.6×10^{-10} atm (*inverted open triangles*). The *dashed curve* shows the predicted volume ratio for pure Mg endmembers, V_{MgSiO_3}/V_{MgO} (*dark band* indicates uncertainties), whereas the *solid curve* shows the volume ratio as a function of pressure derived from our equations of state and assuming no effect of pressure on the Mg/Fe distribution ration between opv and mw (*light band* indicates uncertainties). **Bottom.** At zero pressure, the average value observed for $V_{0,opv}/V_{0,mw}$ is $2.16 (\pm 0.02)$ (*dashed line* with *shaded band* indicating uncertainty), and the individual values show no trends with synthesis pressure. Samples for which measurements were only taken at zero pressure (after synthesis at high pressure) are marked. Error bars indicate measurement uncertainties.

Figure A-4. (A) Photomicrograph in both reflected and transmitted light, and (B) schematic drawing of sample Per_500 quenched to zero pressure after heating, initially at 35 GPa, and compression up to 65 GPa. The locations of microprobe analyses 882 and 898 are marked for reference, and the bright area around the sample is gasket material. Scale bar is 100 μm . (C) Back-scattered electron image (mw appears as bright spots) of region of Per_500 shown in *box* in A, obtained with an electron beam at 10.00 keV and current of 600 pA. Scale bar is 10 μm .

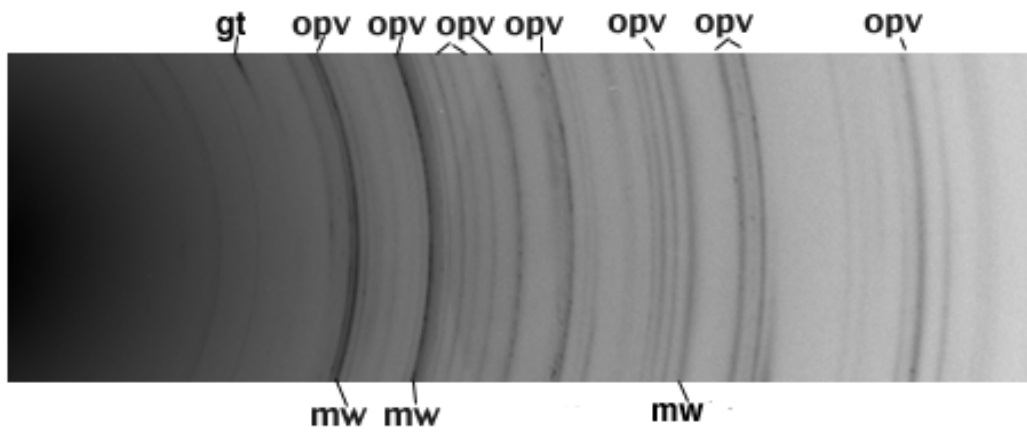
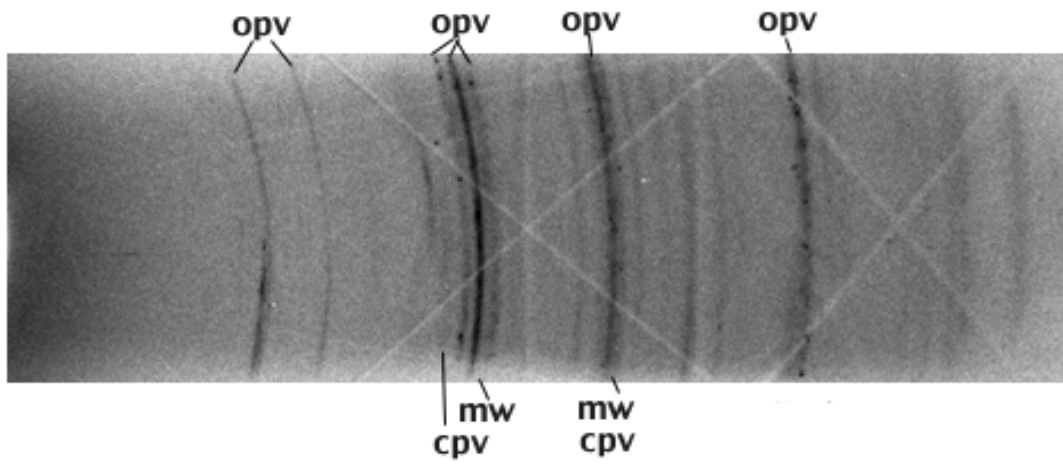


Figure A-1 (A)

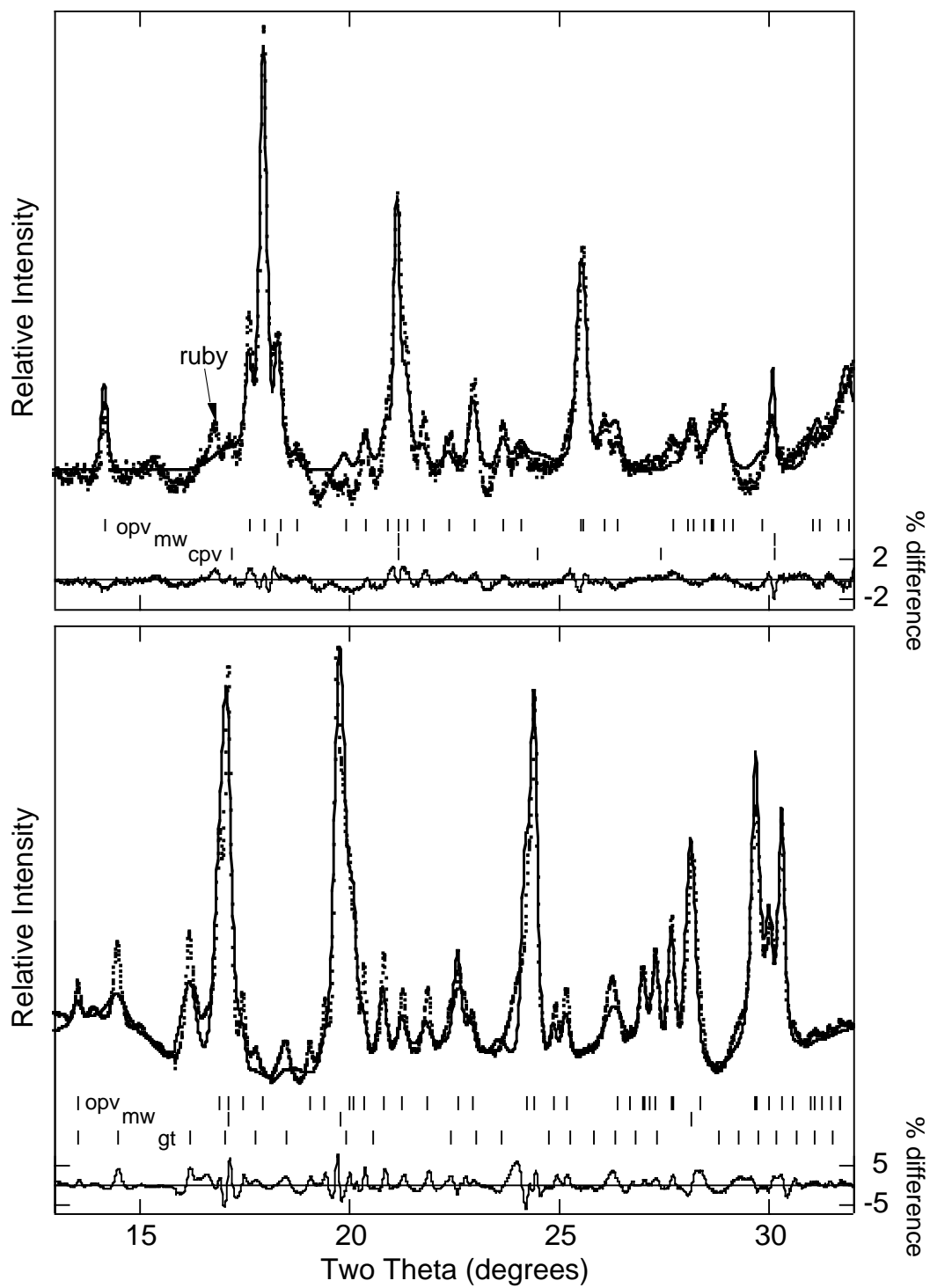


Figure A-1 (B)

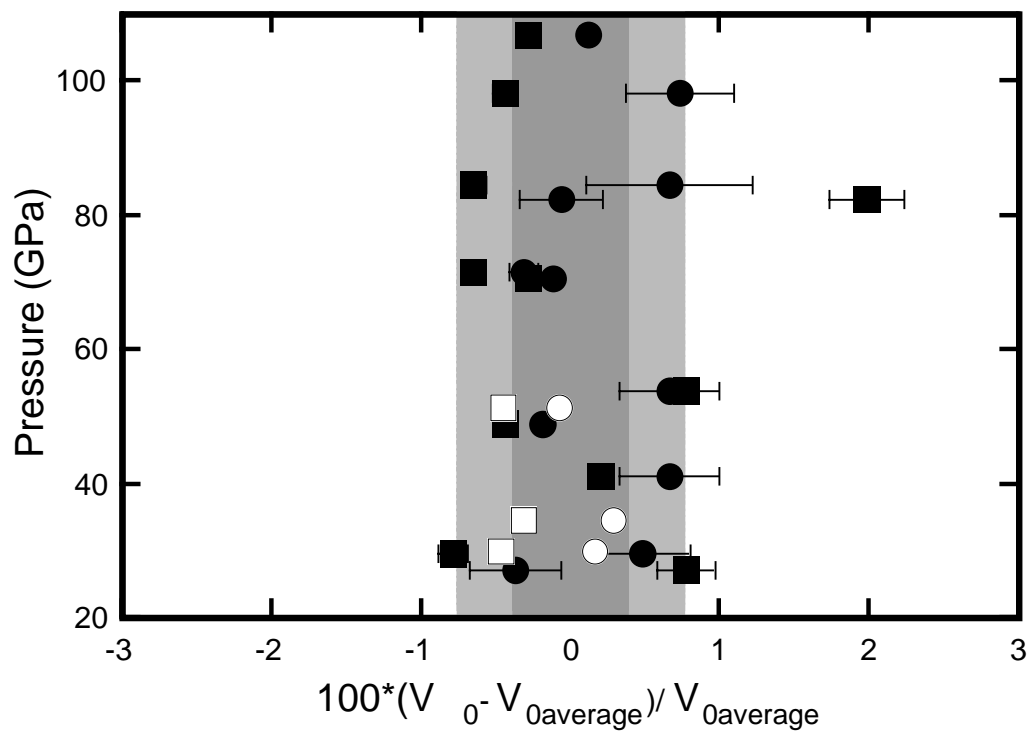
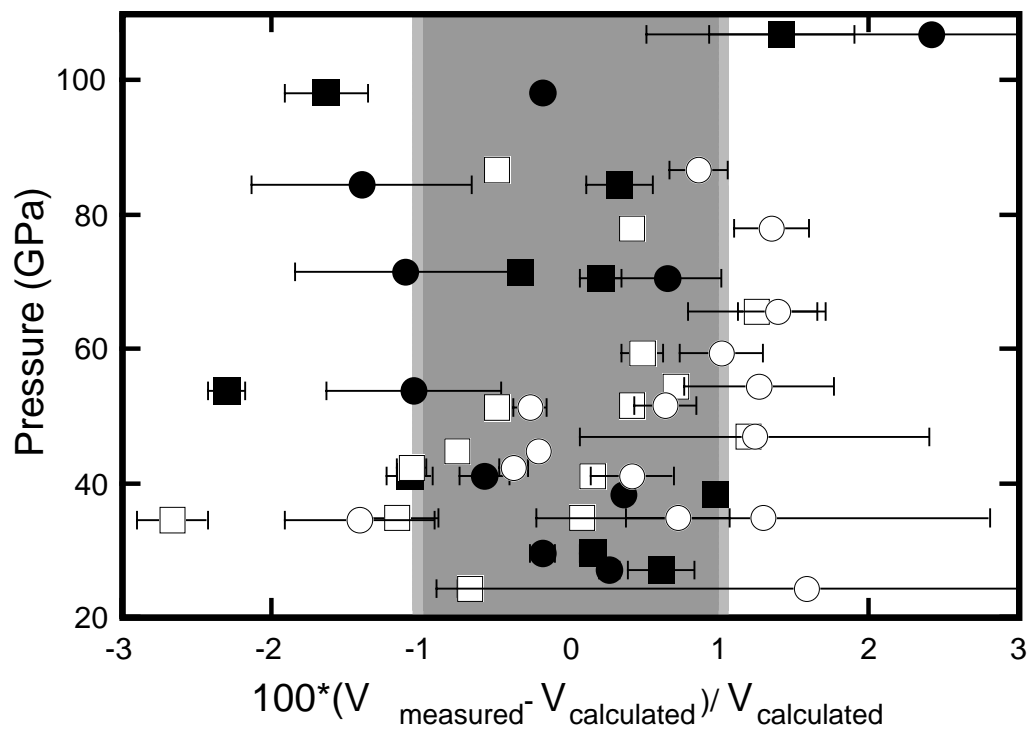


Figure A-2

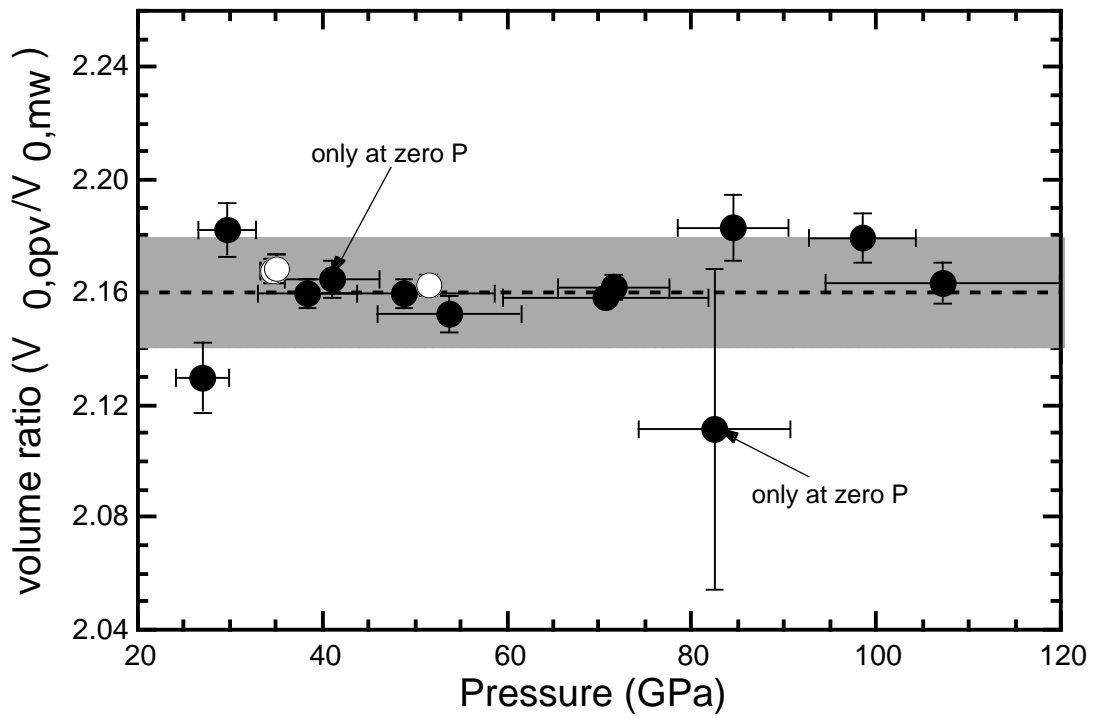
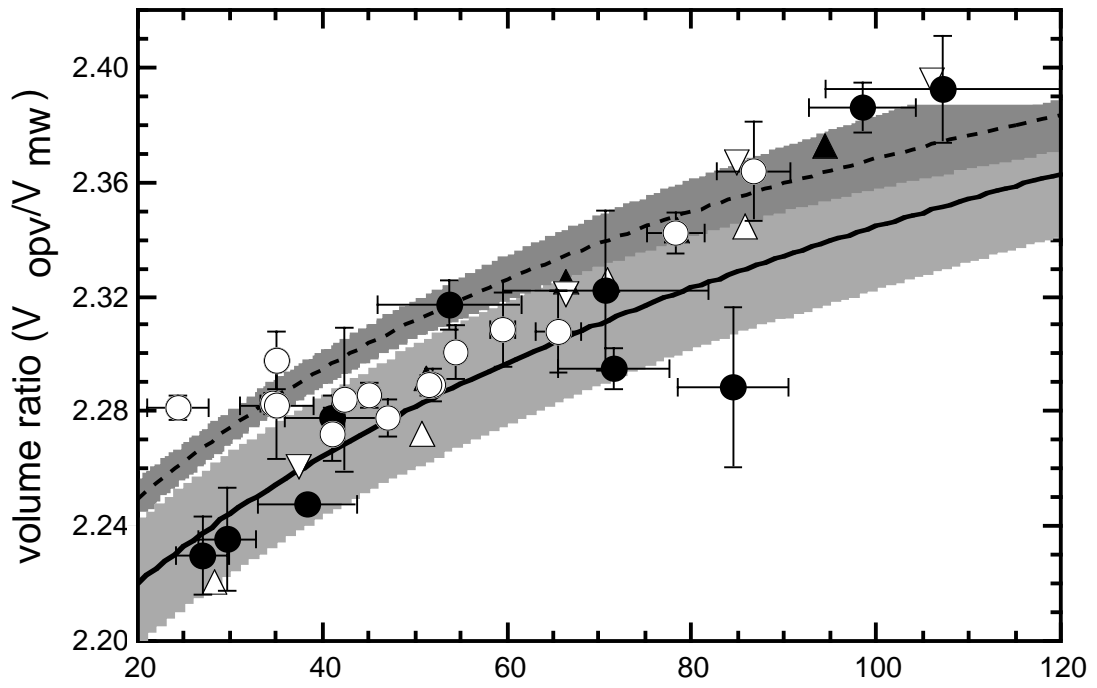
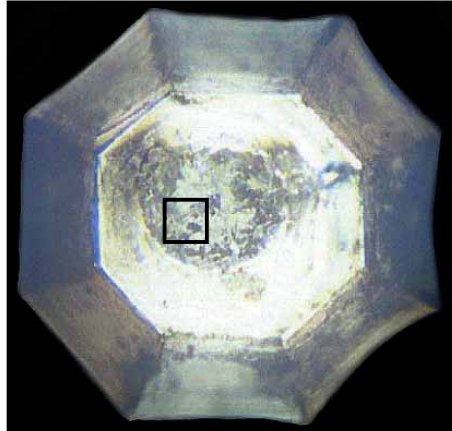
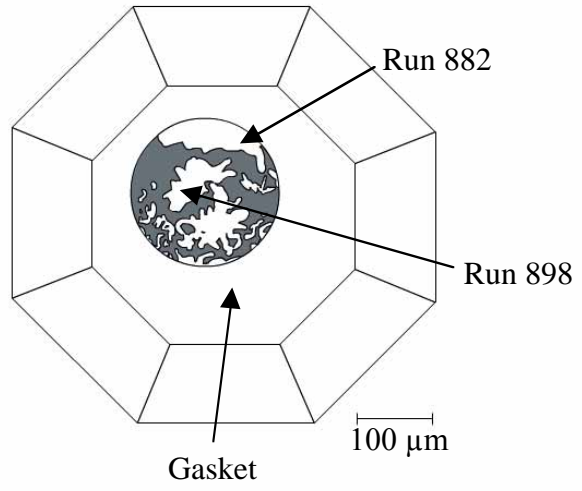


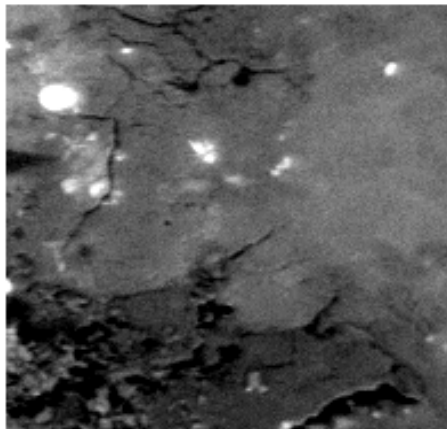
Figure A-3



(A)



(B)



(C)

Figure A-4

Appendix B: Taking thin diamonds to their limit: Coupling static-compression and laser-shock techniques to generate dense water

Abstract. *Laser-driven Hugoniot experiments on pre-compressed samples access thermodynamic conditions unreachable by either static or single-shock compression techniques alone. Recent experiments using Rutherford Appleton Laboratory's Vulcan Laser achieved final pressures up to ~200 GPa and temperatures up to 10,000 K in water samples precompressed to ~1 GPa, thereby validating this new technique. Diamond anvils, used for sample precompression, must be thin in order to avoid rarefaction catch up; but thin diamonds fail under pressure. Anvils no more than 200 μm thick were encased in diamond cells modified to accommodate the laser-beam geometry.*

Introduction

Dynamic experiments generally employ a sample initially at normal density and standard pressure, therefore providing data on the principal Hugoniot. By varying the initial density of the sample through precompression, it is possible to obtain data off the principal Hugoniot, accessing conditions unreachable by either static or single-shock compression. That is, precompression allows an investigation of the entire Pressure-Volume-Temperature (P - V - T) space between the isotherm and Hugoniot.

The method is proven here through experiments on H_2O , which has previously been studied both dynamically and statically to pressures in the multi-Mbar ($\sim 10^2$ GPa) range. The precompression technique is shown below.

Constraints

In laser-driven shock wave experiments, a short, high intensity pulse yields a strong shock. The shock must ideally be steady in order to obtain accurate Hugoniot data. Rutherford Appleton Laboratory's Vulcan Laser generates a $10^{13} - 10^{14}$ W/cm², 4 ns long, 400 μ m diameter pulse by way of seven beams, six of which come from off-axis. This geometry results in two significant design constraints for precompressed samples. First, the intensity and short pulse length require that the anvil through which the laser shock travels be extremely thin—no more than 200 μ m. In order to have a planar shock wave through the sample, the shock wave must propagate through the anvil thickness while the laser is on, thus supporting the wave propagation, else the end-of-pulse rarefaction may catch up. Side rarefaction is also an issue if the laser spot is not large enough to yield a planar front. Second, the laser spot size and beam path require a large aperture radius (hence unsupported anvil radius), r , and aperture angle, θ , in the high-pressure cell itself (Figure B-1).

In order to satisfy the needs for a thin anvil having a large unsupported aperture, we chose the strongest material known, diamond. Use of a diamond anvil cell has numerous advantages, not the least of which are that the basic technology is well established and that the sample can be probed before and during the experiment due to the optical transparency of the anvil. Hence, the thickness, pressure and other characteristics of the pre-compressed sample can be determined at the outset of the Hugoniot experiment.

A small-radius aperture in the backing for the diamond anvil is problematic because the plasma generated by ablation of the backing plate is a source of high energy x-rays

that preheat the sample (3). Also, the blow-off plasma absorbs the laser beam far from the target, thus reducing the shock intensity significantly. In order to avoid preheat, plasma blow-off and laser damage to the DAC, a wide cone angle ($\theta = 35^\circ$) and diamond support hole (300 μm radius) were incorporated into the design of the support plate for the diamond as well as the surrounding diamond cell. This geometry, although accommodating to the laser shock, provides less than optimal support for achieving very high static pressures with thin diamond flats.

Characteristics of Thin Diamond Anvils

The diamond flat can be modeled as a uniformly-loaded circular plate, such that a simple relation exists between the maximum pressure load w and the anvil thickness t

$$w = \frac{k_1 S_m t^2}{r^2} \quad (1)$$

where S_m is the maximum stress achieved in the diamond (here, the tensile strength of diamond), r is the unsupported radius and k_1 is a constant equal to 0.833 (simply supported disc) or 1.333 (disc with fixed edges) (4). For $r = 300 \mu\text{m}$ and $t = 200 \mu\text{m}$ and using the value of tensile strength of diamond, 2.8 GPa (5), we arrive at a maximum load of between 1.0 (simply supported) and 1.7 GPa (fixed edges) (Figure B-2).

The thin diamond flats are fragile and flex under pressure (Figures B-3, B-4), with the maximum amount of deflection y_m described by,

$$y_m = \frac{k_2 w r^4}{E t^3} \quad (2)$$

where E is the elastic modulus (1050 GPa for diamond) and $k_2 = 0.780$ (simply supported) or $k_2 = 0.180$ (fixed edges) (4). Figure B-5 shows good agreement of this simple model with our measurements.

Sample Characterization

Determining the initial pressure–density–internal energy conditions (P_0 , ρ_0 , E_0) in the precompressed sample is key for Hugoniot measurements. The precompression pressure P_0 was measured in the water via ruby fluorescence (2). Using the equation of state of water by Saul and Wagner (6), the initial density ρ_0 and energy E_0 were determined.

White-light interferometry was used to determine the product of the index of refraction and distance nd (7). The height of the Al step (known *a priori*) placed into the sample to aid in the VISAR measurements was used as d ; determining the index of refraction for the compressed water sample was therefore straightforward (Figure B-6). As the index of refraction of water increases with pressure, it is necessary to obtain an accurate starting value for VISAR measurements, which look through the precompressed water.

Conclusion

Despite the fragility of the diamond flats, it was possible to precompress water to ~ 1 GPa ($\rho_0 \sim 1.2$ g/cm³), as predicted by the above models. These precompressed samples were laser-shocked up to pressures of ~ 200 GPa and temperatures to $\sim 10,000$ K (see 12, 13). In order to achieve higher initial pressures (and therefore densities), the

laser intensity and duration must be increased to allow for thicker diamonds flats. For instance, the maximum load that a 500 μm thick diamond flat could withstand is predicted to lie between 6.5 (simply-supported) and 12.5 GPa (fixed-at-edges).

These results also pave the way for laser-Hugoniot measurements on mixtures, including H_2 and He, at high densities and variable temperatures.

References

1. Barker, L. M. and Hollenbach, R. E., *J. Appl. Phys.* **43**, 4669-4675 (1972).
2. Mao, H. K. et al., *J. Appl. Phys.* **49**, 3276-3283 (1978).
3. Moon, S. J. et al., "Computational Design for Laser Produced Shocks in Diamond Anvil Cells," in *Shock Compression in Condensed Matter-2001*, edited by M. D. Furnish, AIP Conference Proceedings 431, Atlanta, 2002.
4. Timoshenko, S. , *Strength of Materials , Part II: Advanced Theory and Problems*, D. Van Nostrand Company, Princeton, New Jersey, 1956, pp. 76-144.
5. Field, J. E., *The Properties of Diamond*, London Academic, London, 1992.
6. Saul, A. and Wagner, W., *J. Phys. Chem. Ref. Data* **18**, 1537-1564 (1989).
7. Le Toullec, R. et al., *Phys. Rev. B* **40**, 2368-2378 (1989).
8. Loubeyre, P. et al., unpublished (2000).
9. Schiebener, P. et al., *J. Phys. Chem. Ref. Data* **19**, 677-717 (1990).
10. Shimizu, H. et al., *Phys. Rev. B* **53**, 6107-6110 (1996).
11. Tkachev, S. et al., *J. Chem. Phys.* **105**, 3722-3725 (1996).
12. Hicks, D. et al., "Laser Driven Shock Waves in Diamond Anvil Cells," *in preparation*.
13. Henry, E. et al., "Temperature Measurements of Water Under Laser-driven Shock Wave Compression," in *Shock Compression in Condensed Matter-2001*, edited by M. D. Furnish, AIP Conference Proceedings 431, Atlanta, 2002.

Figure B-1. Schematic cross-section of diamond-cell configuration used for laser-driven shock experiments on precompressed samples. Wide openings (300 μm radius holes) in tungsten carbide (WC) supports allow ample shock laser entry ($\theta = 35^\circ$ opening) and VISAR access (18.5° opening). Thin diamonds are pushed together to apply pressure on a small sample of water (~ 30 nL) held in a hole within a stainless steel gasket 100 μm thick. An Al step is glued on the thinnest diamond and used to measure the breakout times (velocities, and ultimately shock pressure) with VISAR (1). A few ruby grains are placed in the sample chamber for precompression pressure measurements via ruby fluorescence (2). There is a 1000 \AA Al flash coating on the back side of the thinnest diamond to lower the critical depth of shock ablation, and an anti-reflection coating on the thicker diamond for the VISAR measurement.

Figure B-2. Maximum pressure load w achievable assuming a diamond disc of thickness t that is simply supported (dashed line) or fixed at edges (solid line) with an unsupported radius $r = 200$ μm (thin) or 300 μm (thick). Observations of maximum pressures achieved with $r = 200$ μm (open squares) and with $r = 300$ μm (closed circles) are consistent with these expectations.

Figure B-3. Schematic cross-section illustrating flexure of thin diamond flat (highly exaggerated).

Figure B-4. Typical white-light interferometric measurement showing the symmetric deflection of a diamond flat under compression: total deflection is $0.170\ \mu\text{m}$ for $t = 200\ \mu\text{m}$, $r = 300\ \mu\text{m}$ at a pressure of 0.4 GPa.

Figure B-5. Pressure load vs. maximum deflection for $t = 200\ \mu\text{m}$, $r = 200\ \mu\text{m}$ (open squares, thin lines) and $t = 200\ \mu\text{m}$, $r = 300\ \mu\text{m}$ (closed circles, thick lines). Maximum deflection assuming simply-supported (dashed line) and fixed-at-edges (solid line). For the smaller unsupported radius, the measurements agree with the simply-supported theory, whereas for the larger unsupported radius the measurements are nearer to the fixed-at-edges condition.

Figure B-6. Index of refraction as a function of pressure for H_2O water, ice VI and ice VII at room temperature. The values obtained in the present study (closed circles) compare well with previous results of Loubeyre et al., (closed squares) (8); Schiebener et al., (closed diamonds) (9); and Shimizu et al., (open triangles) (10). In one run, ice VI crystals were observed at a pressure less than the nominal freezing pressure, indicating a possibly metastable condition (11).

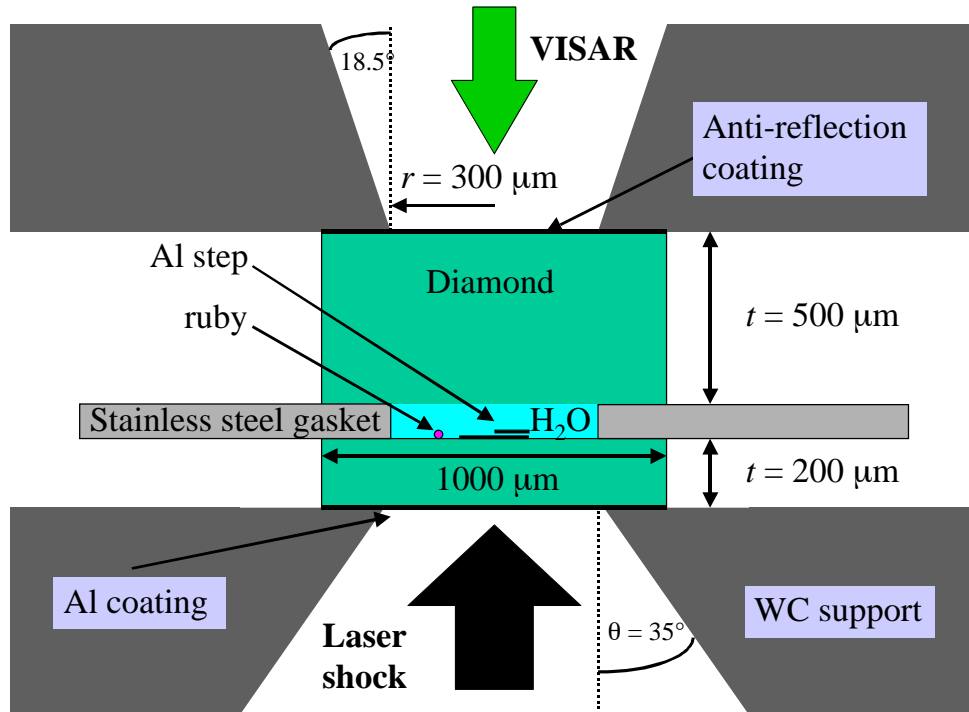


Figure B-1

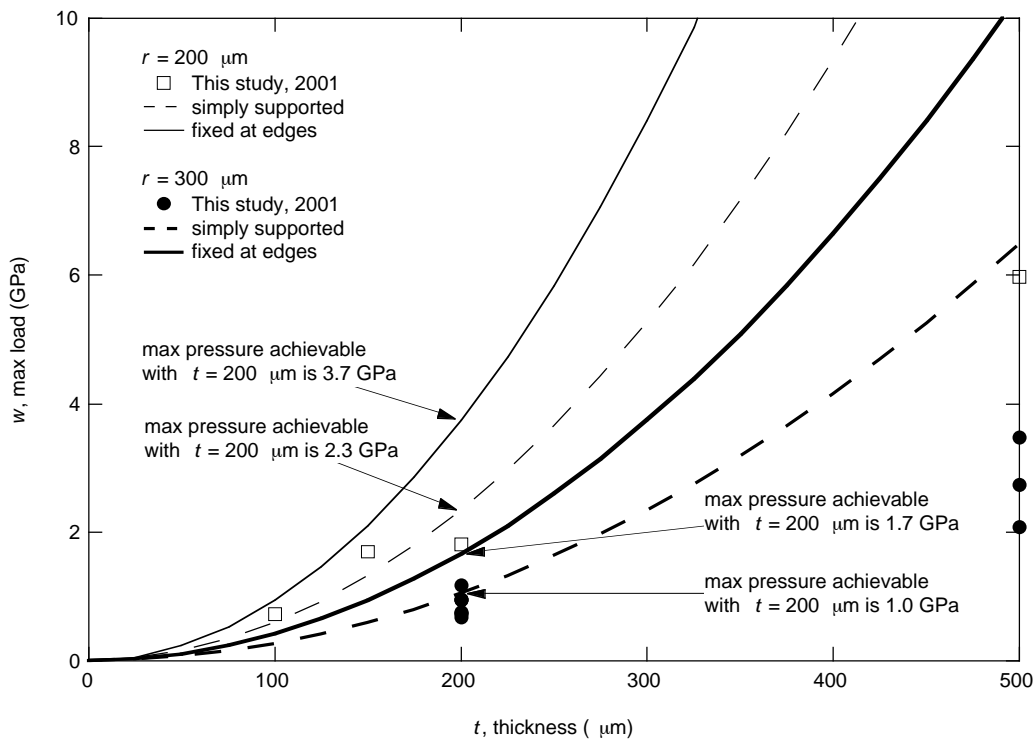


Figure B-2

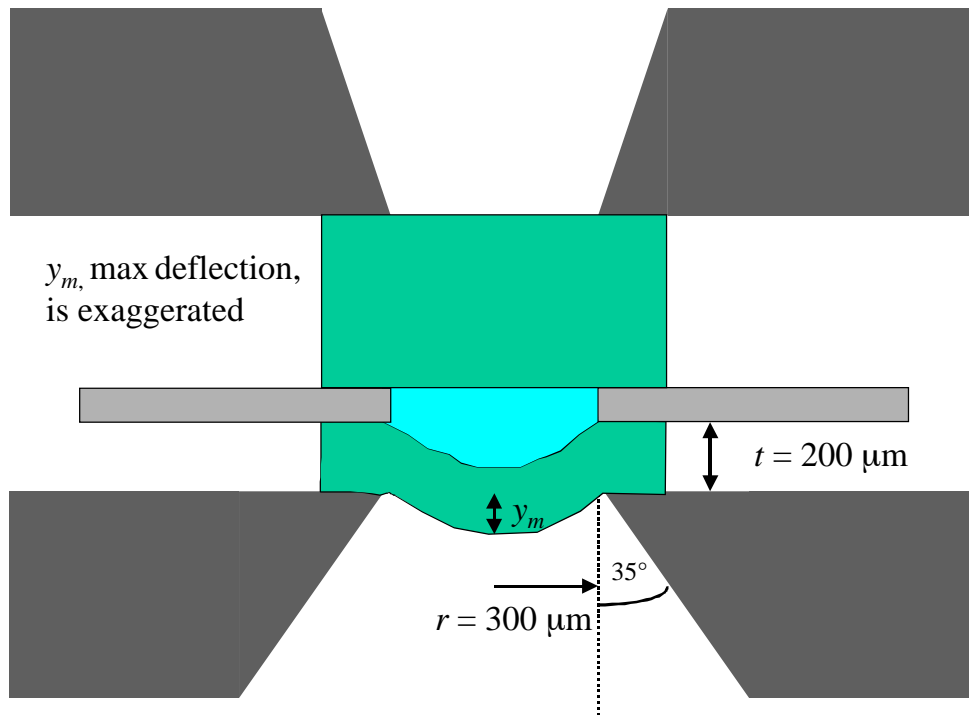


Figure B-3

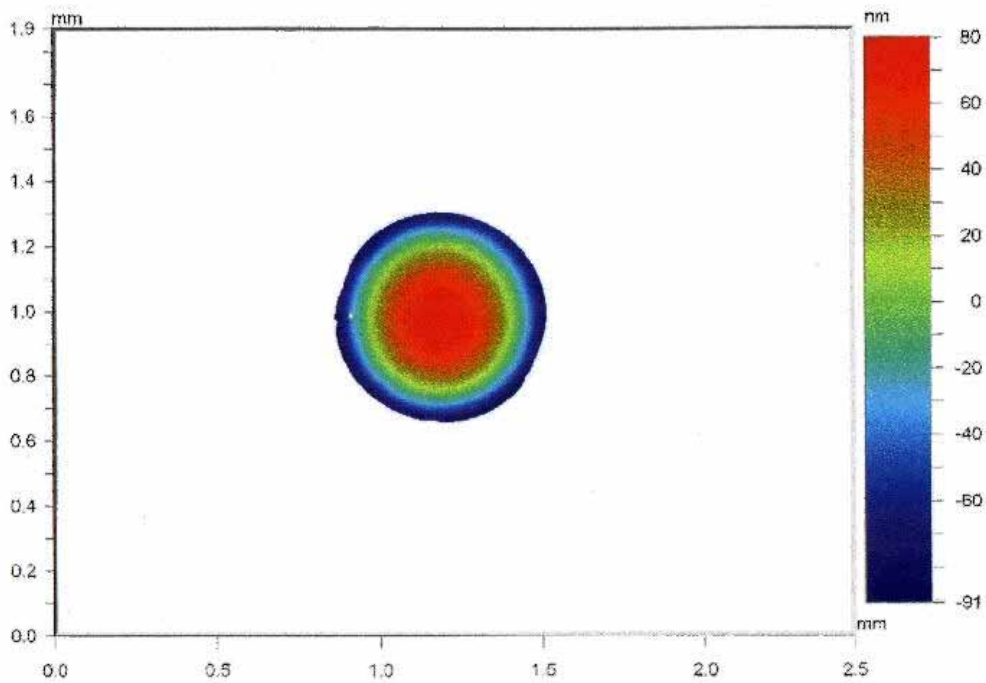


Figure B-4

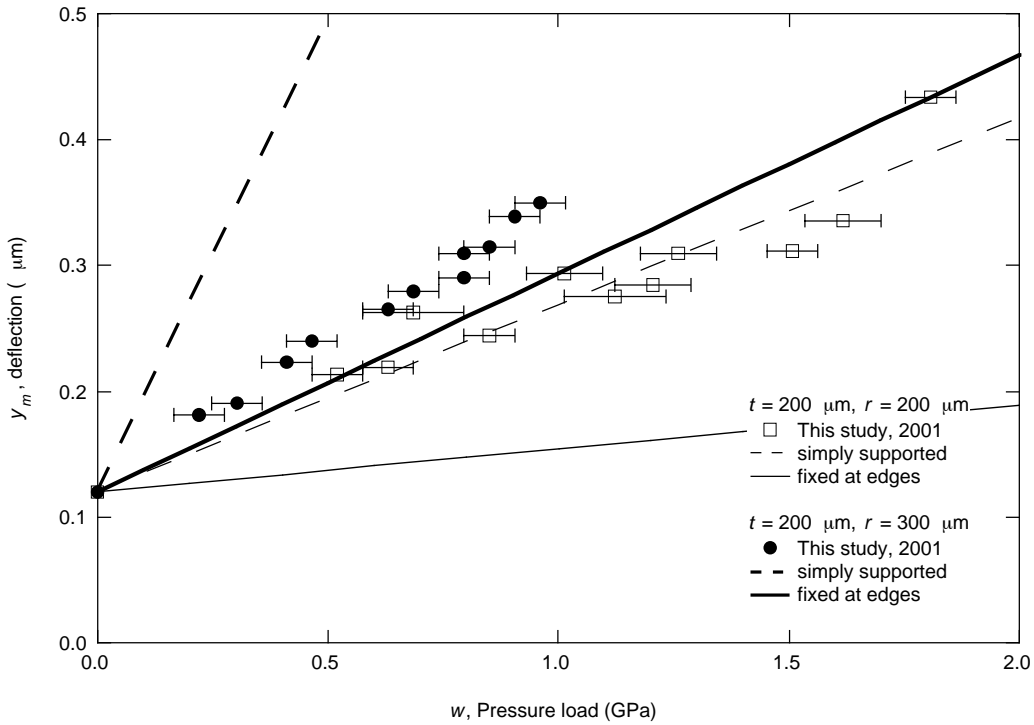


Figure B-5

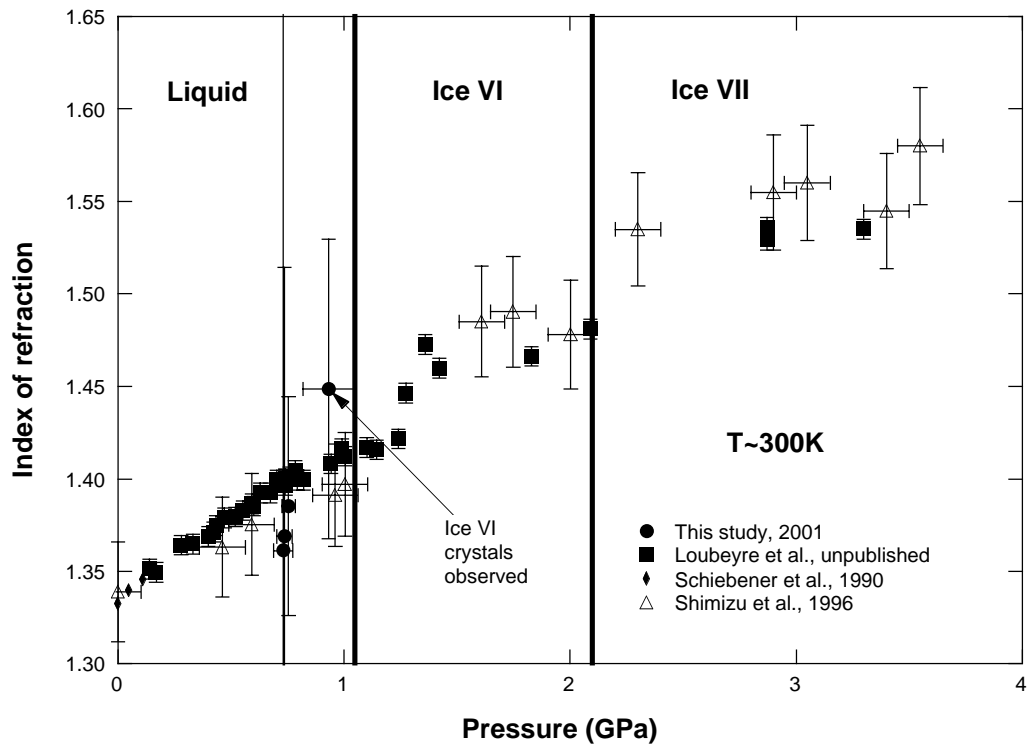


Figure B-6